3D Reconstruction of Plasma Equilibria using Magnetic Diagnostics on the Compact Toroidal Hybrid

by

Benjamin Adam Stevenson

A dissertation submitted to the Graduate Faculty of
Auburn University
in partial fulfillment of the
requirements for the Degree of
Doctor of Philosophy

Auburn, Alabama
December 12, 2011

Keywords: Fusion, energy, plasma, equilibrium, reconstruction

Approved by

Stephen F. Knowlton, Chair, Professor of Physics
James D. Hanson, Professor of Physics
Gregory J. Hartwell, Associate Research Professor of Physics
Edward Thomas, Jr., Professor of Physics

Abstract

Equilibrium reconstruction of magnetically confined plasma for fusion energy research uses magnetohydrodynamic (MHD) theory in combination with experimental diagnostic data to accurately model high temperature plasma discharges. Reconstruction of two dimensional, axisymmetric plasma equilibria are commonly used in many of today's fusion energy experiments. The ability to reconstruct fully three dimensional plasma equilibria has received less attention, but is becoming increasingly important in stellarator as well as tokamak research. This dissertation describes the process of reconstructing plasma equilibria produced in the Compact Toroidal Hybrid (CTH) device. CTH is a torsatron, a type of stellarator. Stellarators confine plasmas using external magnetic field coils without the requirement of plasma current. Nonetheless, toroidal currents can be driven in CTH, which significantly modifies the equilibrium. Plasma equilibria of current-driven discharges are reconstructed using data from a set of magnetic diagnostics and the V3FIT equilibrium reconstruction code[1]. The main magnetic diagnostics used consist of several segmented Rogowski coils as well as a movable Hall sensor array. The details of the construction and calibration of each of these diagnostics are described. The reconstructed plasma results are shown and compared with measurements made using the Hall sensor array. Finally, sources of systematic error and the suggested steps for improving the reconstruction process are described.

Acknowledgments

I would first like to thank my Lord and savior Jesus Christ who through his loving kindness gave me the wisdom and strength to complete this work. My deepest gratitude also goes to my loving bride who has supported me through this difficult process. Susan I could not have done this without you.

Table of Contents

List of Tables

List of Figures

1 Introduction

There currently exists a continually increasing demand for energy production. In 2001, the world used energy at an approximate rate of 500 Quads/yr. Essentially all projections of the future suggest that this rate will at least double within the next 100 years. Fossil fuels, including oil, coal, and natural gas currently supply 86% of this energy. Even if the energy use remained at 500 Quads/yr, oil and natural gas reserves are projected to be expended within the next century. Increasing energy needs combined with decreasing reserves demand new sources of reliable energy production.[2,3,4]

One quite promising new source of energy is that produced from fusion. Fusion is the nuclear reaction in which light nuclides merge to produce heavier nuclides along with a substantial amount of energy. An example of a typical fusion reaction is:

$$D + T \rightarrow {}^{4}He + n + 17.6MeV \tag{1.1}$$

where the fusion reactants are deuterium (D) and tritium (T) and the reaction products are Helium and an energetic neutron.[5] At low energies (<1 keV), the reaction cross-section is quite low due to the Coulomb repulsive force. For the D-T reaction, the cross-section is largest when the reactant energies are approximately 100 keV. If fusion takes place within a thermal distribution of particles, the temperature required for an optimal rate of fusion power is 10 keV, because at this temperature the fusion reactions occur in the high energy tail of the Maxwellian energy distribution. Fusion brought about by heating the reactants to these high temperatures is

called thermonuclear fusion. If a sufficient density of reactants with these high temperatures can be maintained, the energy produced from the fusion reactions will sustain these temperatures.[6] However, maintaining a high density of reactants with such high temperatures has proven to be quite difficult. The required conditions can be quantified with a commonly used figure of merit referred to as the fusion triple product[7] which is the product of the peak density (n), temperature (T), and energy confinement time (τ_e). This triple product is based on the Lawson criterion[8], and for a self sustaining D-T reaction requires the following condition:

$$n\tau_e T \geq 5\times10^{21}\frac{s\,keV}{m^3} \tag{1.2}$$

Achieving a fusion triple product of this magnitude has driven research efforts for over 50 years.[9] Developing new technologies have led to a significant improvement in the triple product as shown in Figure 1.1. An important part of reaching the conditions needed for a fusion reactor is an effective method of confining the fusion reactants.

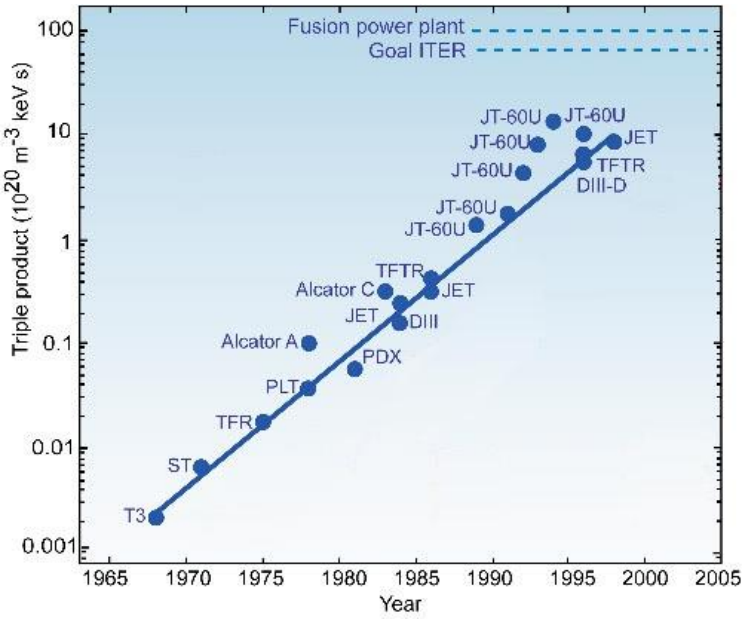

Figure 1.1 – Increase in the fusion triple product achieved in tokamak magnetic confinement experiments as a function of time. Dashed lines indicate target values for the ITER device, and a fusion power plant.[10]

The reactant gases are ionized at such high temperatures, and exist in the plasma state. Due to the Lorentz force, the charged particles in a plasma can be effectively confined in some magnetic field configurations. There are a variety of magnetic field configurations which have been developed to confine a high temperature plasma[5]. Many of these magnetic field configurations confine the plasma within a torus. The two classes of toroidal confinement devices that will be discussed in this dissertation are the tokamak and the stellarator.

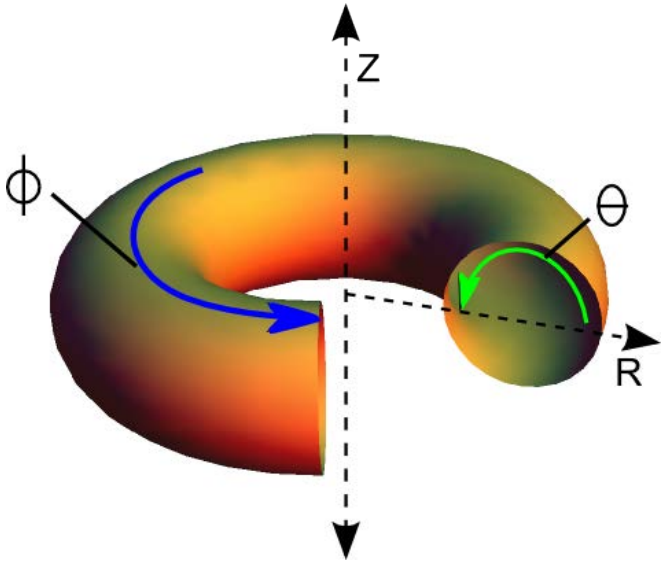

Figure 1.2 – Toroidal magnetic confinement geometry showing toroidal direction (blue arrow) and poloidal direction (green arrow)

A combination of both toroidal and poloidal magnetic field components confine the plasma in tokamaks and stellarators. The orientations of these two required field components are shown in Figure 1.2. The azimuthal angle φ increases in the toroidal direction, and θ represents the poloidal angle. This figure defines the toroidal geometry that will be used throughout this dissertation. In cylindrical coordinates, the variable R represents the radial distance from the axis of the torus, and Z represents the vertical distance from the mid-plane of the torus. When the toroidal and poloidal magnetic fields are combined, they produce a helical magnetic field. Stellarators are designed to generate both the toroidal and poloidal field components using

external magnet coils. However, in tokamaks, only the toroidal field and a relatively small portion of the poloidal field are made using external magnet coils. The primary poloidal field in a tokamak is created by the toroidal current driven within the confined plasma.

To confine the plasma, the toroidal and poloidal fields are configured in such a way as to form nested magnetic flux surfaces, as shown in Figure 1.3. Within this magnetic field

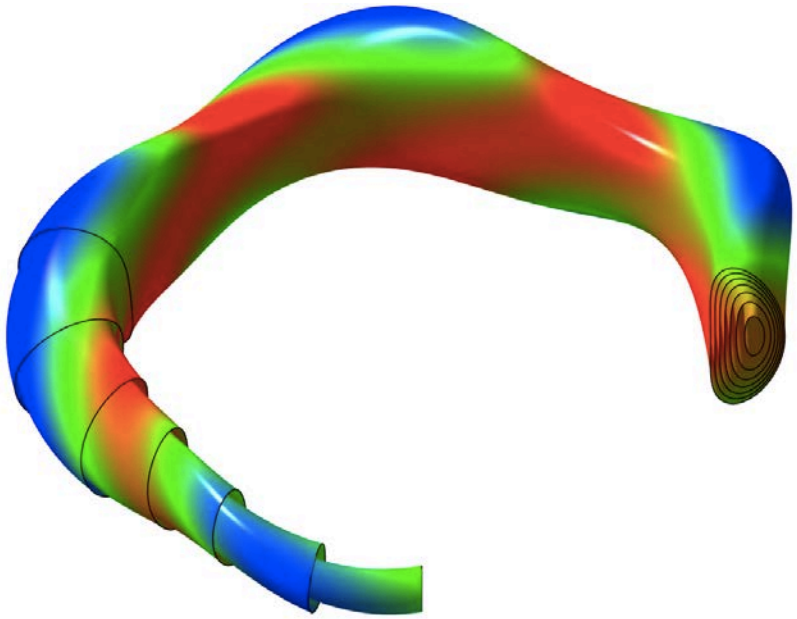

Figure 1.3 – Model of the nested magnetic flux surfaces on the Compact Toroidal Hybrid

structure, the dynamics of hot plasmas are effectively modeled using the theory of ideal magnetohydrodynamics (MHD). A review of ideal MHD and how it relates to fusion relevant plasmas is given by Friedberg[11]. The ideal MHD equation which describes the motion of a fluid element of the plasma is given by:

$$\rho_m \frac{d\mathbf{v}}{dt} = -\nabla p + \mathbf{J} \times \mathbf{B} \tag{1.3}$$

where ρ_m is the mass density, **v** is the flow velocity, p is the pressure, **J** is the current density, and **B** is the magnetic field. When the plasma is in equilibrium, the time derivative of the left side of Eq. (1.3) is zero. This leads to the following equilibrium equation:

$$\nabla p = \mathbf{J} \times \mathbf{B} \tag{1.4}$$

This equation represents the fundamental force balance that is required to maintain a plasma in equilibrium. Two additional properties of the nested flux surfaces can be derived from this force balance equation. The scalar product of the magnetic field and Eq. (1.4) gives the following:

$$\mathbf{B} \cdot \nabla p = \mathbf{B} \cdot (\mathbf{J} \times \mathbf{B}) = 0 \tag{1.5}$$

Eq. (1.5) shows that **B** is orthogonal to ∇p which says that the magnetic surfaces previously described are also contours of constant pressure. Similarly, the scalar product of the current density with the equilibrium Eq. (1.4) gives:

$$\mathbf{J} \cdot \nabla p = \mathbf{J} \cdot (\mathbf{J} \times \mathbf{B}) = 0 \tag{1.6}$$

This shows that the current density is also parallel to the magnetic surfaces.

Properties of the magnetic flux surfaces such as the current and pressure distributions can affect the stability and confinement of the plasma[12-16]. The shape of the flux surfaces have also been linked to plasma performance and stability[12,17,18]. The ability to accurately model the equilibrium flux surfaces has proven to be an important aspect of understanding magnetically confined plasmas. To model the magnetic flux surfaces, one must determine the spatial locations where the magnetic and pressure forces balance (Eq. 1.4). Most modern devices have complex magnetic field geometries which make it necessary to employ numerical algorithms to solve the equilibrium condition. Many toroidal devices, including tokamaks, are designed to be axisymmetric which means the flux surface shape and position does not vary with toroidal angle.

For these devices, the flux surface geometry that satisfies the force balance condition can be calculated, usually numerically, using the Grad-Shafranov equation[6] derived from Eq. (1.4). However, stellarators do not exhibit axisymmetry. Also, magnetic field errors in nominally axisymmetric devices can result in asymmnetric magnetic equilibria. In these cases, the algorithms must be able to model fully three-dimensional (3D) MHD equilibria. The 3D equilibrium solver used in this study is the Variational Moments Equilibrium Code (VMEC)[19].

As shown in Eq. (1.4), information about the current and pressure profiles as well as the magnetic field are required to solve the equilibrium condition. These quantities are typically defined within equilibrium codes by using a series of input parameters. When using an equilibrium solver to model an experimental plasma, it is important that the input parameters chosen accurately represent the experiment. The accuracy of the resulting equilibrium model can then be determined through comparisons with experimental data. Equilibrium reconstruction is a method that optimizes the model of the adjustable parameters specifying the current and pressure profiles by choosing input parameters that minimize the differences between modeled and experimental diagnostic data. Measurements of the local and average magnetic flux are commonly used for equilibrium reconstruction. During the reconstruction process, simulated quantities corresponding to the experimental diagnostic signals are calculated based on the modeled equilibrium. These simulated diagnostic signals are then compared with the experimental diagnostic signals. Based on this comparison, the model input parameters are adjusted, and the equilibrium flux surfaces are recalculated. This iterative process optimizes the equilibrium input parameter until the difference between the simulated and experimental diagnostic signals has reached a minimum.

One of the earliest examples of equilibrium reconstruction was of an axisymmetric plasma in the Doublet-IIA experiment[20]. Since that time, axisymmetric equilibrium reconstruction has become a critical diagnostic tool in magnetized fusion research. The EFIT[21] code is used to reconstruct equilibria on many axisymmetric experiments including DIII-D[22], JET[23], and KSTAR[13].

Previous attempts have been made to apply 3D reconstruction techniques on stellarator equilibria.[24,25] In this dissertation, the relatively new V3FIT reconstruction code[1] is applied to stellarator MHD equilibria. This code has been benchmarked against the EFIT code for axisymmetric plasmas, but is only beginning to be used to reconstruct fully three-dimensional equilibria modified by finite current and pressure. This dissertation presents the first reconstructions of experimental 3D plasmas in the Compact Toroidal Hybrid (CTH) device.

The outline of this dissertation is as follows: Chapter 2 provides a physical description of the CTH device including typical plasma parameters. Chapter 3 describes the design, construction, and calibration of the magnetic diagnostics that were used in equilibrium reconstruction. Chapter 4 gives a general discussion of the equilibrium reconstruction codes, with emphasis on the input and output parameters used during reconstructions. Chapter 5 discusses the various techniques that were used to optimize the modeled diagnostics as well as the corrections that are made to the experimental signals. Chapter 6 presents the results obtained from 3D equilibrium reconstruction of current-carrying discharges on CTH and recommends further steps for this research project.

2 Compact Toroidal Hybrid

CTH is a torsatron designed to investigate the stability of current-carrying plasmas. Plasmas can be confined within CTH using only external magnet coils because the external coils produce both the toroidal and poloidal magnetic fields required for confinement. However, the plasma equilibria reconstructed in this dissertation are configured so that a significant portion of the confining magnetic field is produced by toroidally driven plasma current. The calculation of plasma equilibria requires specific knowledge of the magnitude of the external currents and their locations. The external magnet coils on CTH are described in this chapter as well as their effect on the shape and position of the equilibrium. Besides the external coil currents, there are also significant eddy currents driven in the vacuum vessel and surrounding structures. The proximity of these eddy currents to the magnetic diagnostics used for reconstruction make it necessary to include these currents in the reconstruction. Therefore, the physical properties of the vacuum vessel and coil frame are also described. The final section describes the process used to generate typical plasmas discharges on CTH with and without toroidal plasma current.

2.1 CTH coil configuration

There are several independently controlled sets of external magnet coils on CTH, allowing flexibility in the geometry of the vacuum magnetic field that can be produced. The layout of the magnet coil configuration is shown in Figure 2.1. The magnetic field coils on CTH

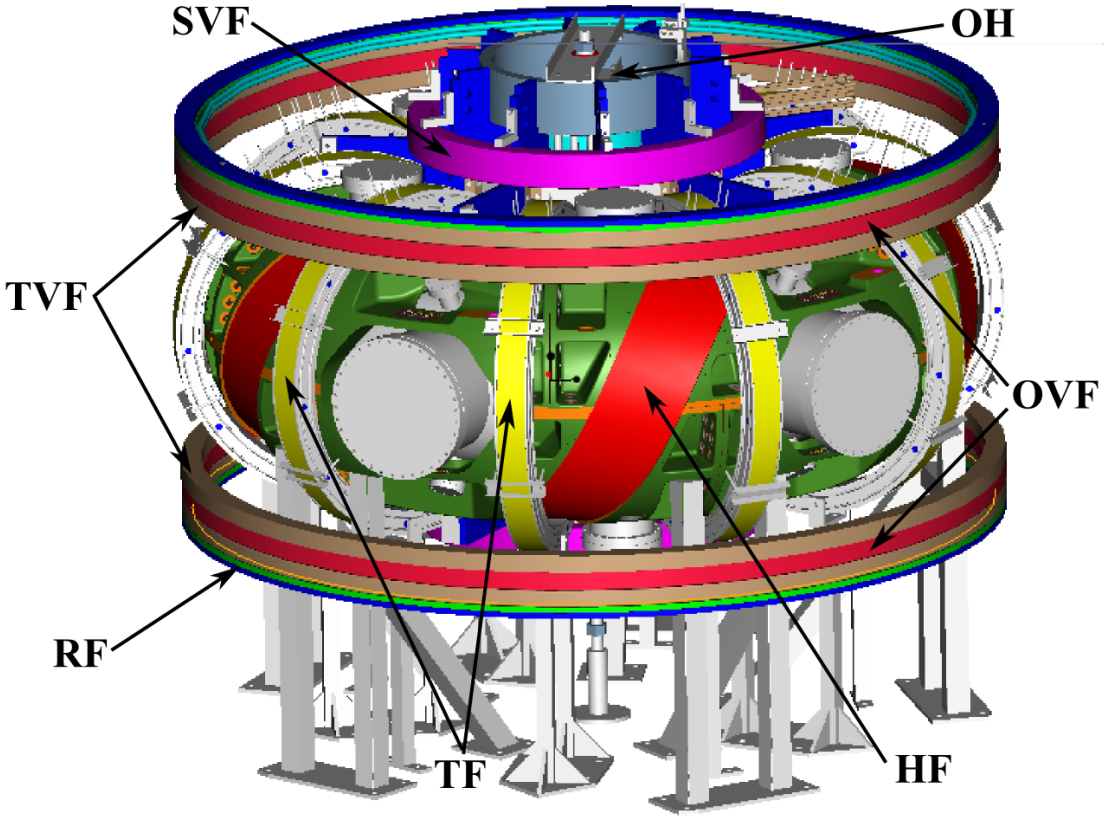

Figure 2.1 – CTH device showing HF, OVF, TVF, TF, RF, SVF, OH, coil frame, and vacuum vessel.

are designed to produce magnetic surfaces that are field-periodic. In a magnetic field configuration that is field periodic, the cylindrical coordinates describing the magnetic flux surfaces have the following property:

$$\left[R(\Phi,\theta,\varphi), Z(\Phi,\theta,\varphi)\right] \leftrightarrow \left[R\left(\Phi,\theta,\frac{2\pi n}{N}+\varphi\right), Z\left(\Phi,\theta,\frac{2\pi n}{N}+\varphi\right)\right] \tag{2.1}$$

Here the functions R and Z refer to the set of points which define the flux surface. Φ is a radial flux coordinate, and θ and φ are the poloidal and toroidal angles respectively. N is the number of field periods, and n is any integer. CTH has a field periodicity of N=5. The coil configuration is also designed to exhibit stellarator symmetry, such that the magnetic flux surfaces also exhibit the following property:

$$\left[R(\Phi,\theta,\varphi),Z(\Phi,\theta,\varphi)\right]\leftrightarrow\left[R(\Phi,\theta,-\varphi),-Z(\Phi,\theta,-\varphi)\right] \tag{2.2}$$

The torsatron configuration provides both a toroidal field and a poloidal field with a single-polarity helically wound coil. The helical field (HF) coil of the CTH torsatron is shown in Figure 2.2. It is wound into an aluminum coil frame. The HF coil frame is made up of 10 electrically-

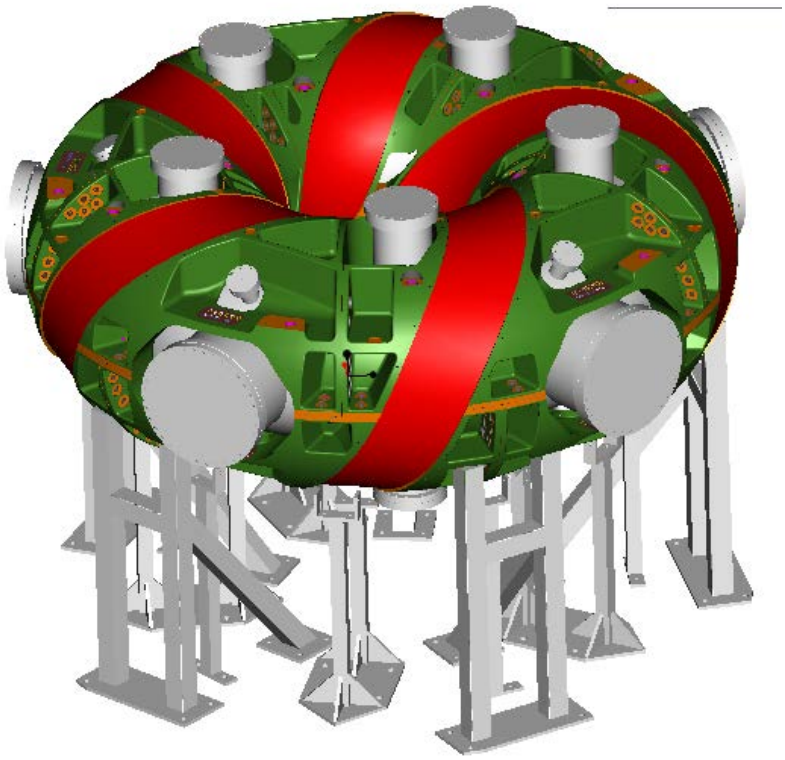

Figure 2.2 – HF coil (red) wound onto the HF coil frame (green) which encases the vacuum vessel.

isolated segments. Its electrical properties will be discussed in greater detail in Sec. 5.1. The HF coil encircles the vacuum vessel twice in the toroidal direction and five times in the poloidal direction. This coil defines the 5-field periodicity of CTH.

As is typical in torsatrons, an additional vertical field must be applied to produce closed toroidal flux surfaces within the vacuum vessel. In CTH, the vertical field is provided by two separate sets of vertical field coils, each providing on the order one-half of the net external

vertical field. The first vertical field coil is the outer vertical field (OVF) coil set and is connected in series with the HF coil. The flux surfaces generated using only the HF/OVF coil set are centered near the outer radius of the vacuum vessel. An additional vertical field is applied by the Trim Vertical Field (TVF) coils which shift the flux surfaces radially inward allowing the equilibria to be centered within the vacuum vessel. Characteristic currents within the HF/OVF and TVF coil sets during a typical plasma discharge are shown in Figure 2.3(a). The closed flux surfaces produced using these coil currents are modeled using the VMEC code[19]. (The use of VMEC on CTH will be discussed in greater detail in Sec. 4.1.) Cross sections of the calculated flux surfaces are shown in Figure 2.3(b) for two toroidal angles. These toroidal angles represent

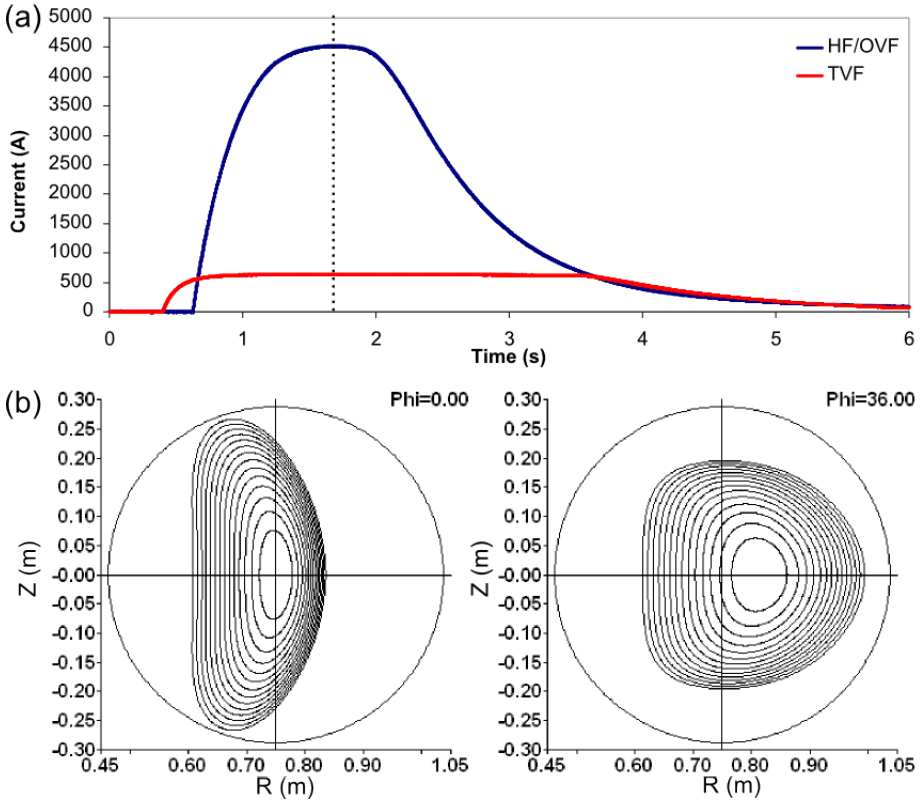

Figure 2.3 – (a) TVF and HF/OVF current traces; Dashed line indicates currents used for the (b) surface of section plots showing two symmetry planes which were calculated using VMEC

the full (φ=0˚), and half (φ=36˚) field period locations where the flux surfaces are centered along the mid-plane of CTH. The outermost circles shown in these plots represent the minor radius of the vacuum vessel.

CTH is equipped with 10 toroidal field (TF) coils. Unlike a tokamak or a conventional stellarator such as W VII A, these coils do not provide the primary toroidal field, but are used to vary the ratio of the toroidal to poloidal field strength. The helicity of the confining magnetic field is characterized using the rotational transform defined as follows[5]:

$$\iota = \frac{\iota}{2\pi} = \frac{d\mathrm{X}}{d\Psi_{t_{tot}}} \tag{2.3}$$

Here, $\Psi_{t_{tot}}$ and X represent the toroidal and poloidal magnetic flux respectively. The addition of the toroidal field from the TF coils makes it possible to vary the vacuum rotational transform within the range $0.02 < \iota(s) < 0.4$. Five rotational transform profiles are shown in Figure 2.4 as a function of the normalized toroidal flux which is normalized to the total toroidal magnetic flux. In this plot, the middle profile shows the rotational transform profile without TF current such that

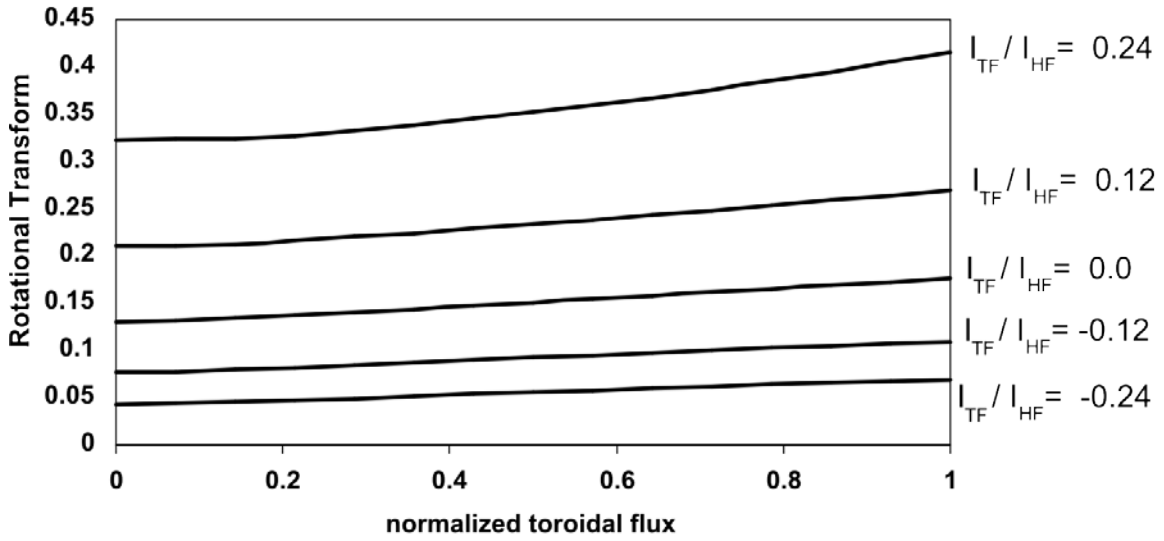

Figure 2.4 – Vacuum rotational transform profiles vs. normalized toroidal flux for different I_{TF}/I_{HF} current ratios

I_{TF} / I_{HF} = 0.0 current in the TF coils. The lowest profiles are when the TF coils have a negative current so the magnetic field produced increases the toroidal field created by the HF coil. In contrast, the top two profiles demonstrate the effect of a positive TF current which reduces the toroidal field produced by the HF coil thereby increasing ι. Similar to the TVF and HF/OVF coil sets, the TF coils are powered using a set of motor generators.

As shown in Figure 2.1, there are a set of radial field coils (RFC) which are adjacent to the TVF coils. The RFC coils adjust the plasma's vertical position and can be used to correct vertical asymmetries. The RFC set is composed of circular pancake coils identical to the TVF coils, with the top and bottom RFC coils configured with opposite polarities to produce a net radial field component inside the volume of the CTH plasma. The effect of adding this radial

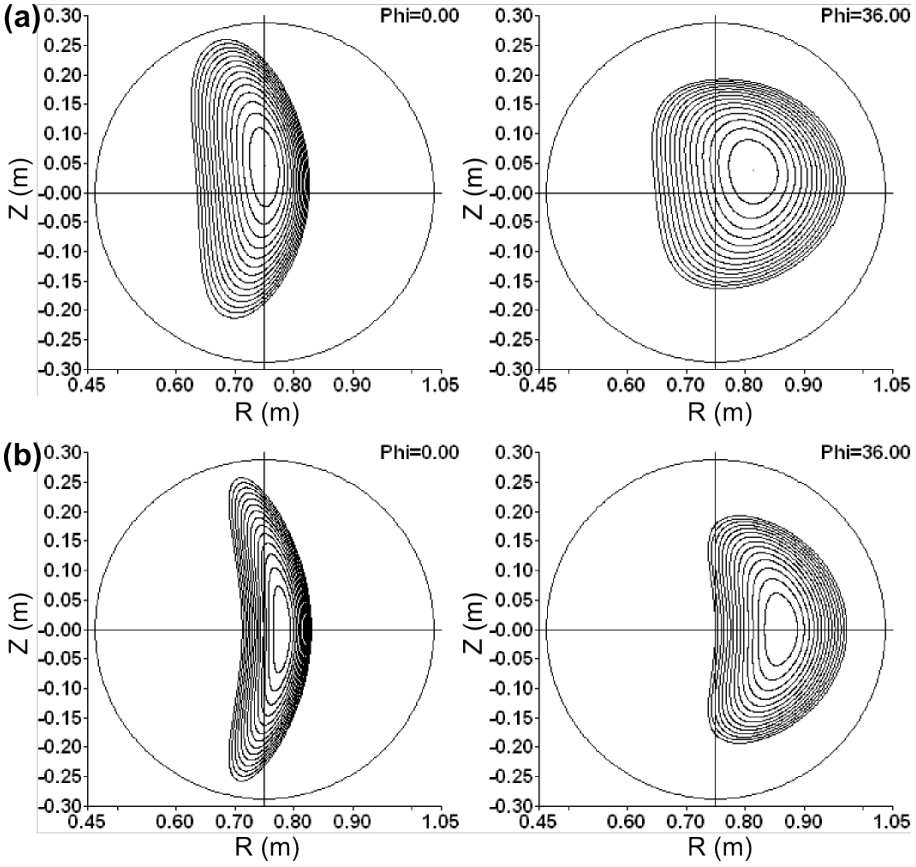

Figure 2.5 – Surface of section plots calculated using VMEC which show (a) the vertical shift which results from 200A of current in the RFC magnet coil, and (b) the effect of adding the SVF quadrupole field with I_{SVF}/I_{HF} =0.1.

field on the equilibrium position can be seen in Figure 2.5(a). There is also a shaping vertical field (SVF) coil set which produces a quadrupole field to change the plasma elongation. The effect of this quadrupole field on the magnetic flux surfaces is shown in Figure 2.5(b).

CTH is equipped with an ohmic heating (OH) transformer. The OH coil set is used to inductively drive a toroidal plasma current that heats the plasma and increases the rotational transform above the vacuum level. Figure 2.6 is a schematic of the central OH coil stack, which is oriented along the central axis of CTH. The OH coil set also consists of two additional poloidal field coils adjacent to the OVF coil which reduce the magnetic flux produced by the OH current within the plasma region. Current is supplied to the OH coil using a set of capacitor banks. The current is shown in Figure 2.7 as a function of time for a typical OH discharge along with the resulting toroidal loop voltage. The induced plasma currents and the effects on equilibrium will be discussed further in the next section.

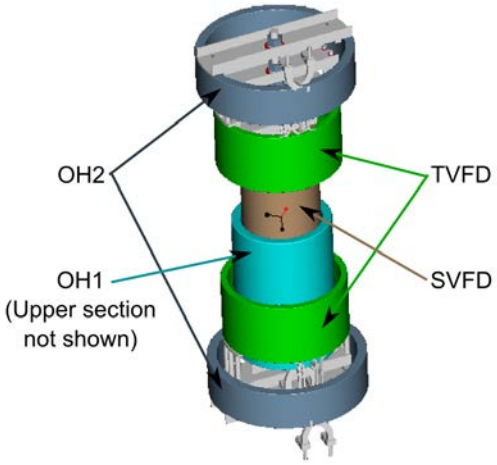

Figure 2.6 – OH central coil pack along with decoupler coils for the TVF and SVF.

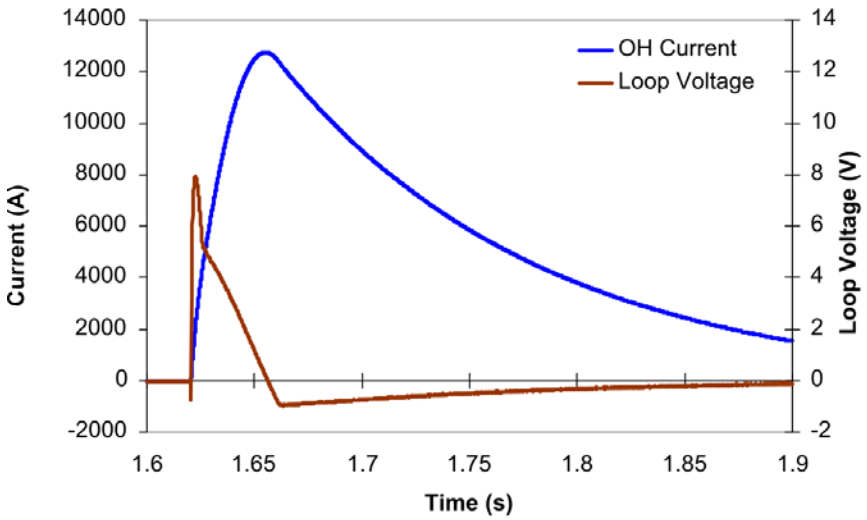

Figure 2.7 – Typical OH current versus time along (blue) with the resulting toroidal loop voltage (brown)

The OH induced voltage that drives the plasma current induces current in the other magnet coils. To minimize the induced current in the TVF coil, a trim vertical field decoupler (TVFD) coil was connected in series. The TVFD coil was designed such that the combination of the TVF and TVFD would have a negligible mutual inductance with the OH coil. Similarly, the SVF is also connected in series with a decoupler coil (SVFD). The TVFD and SVFD are located along the central axis of CTH near the OH solenoid as shown in Figure 2.6. In order to decouple the HF/OVF from the OH coil, a decoupling transformer is connected in series to each of these coil set feeds. This transformer is located approximately 10 m away from CTH to keep its magnetic field from interfering with the CTH confinement fields. At this distance, the stray field is approximately 50 G.

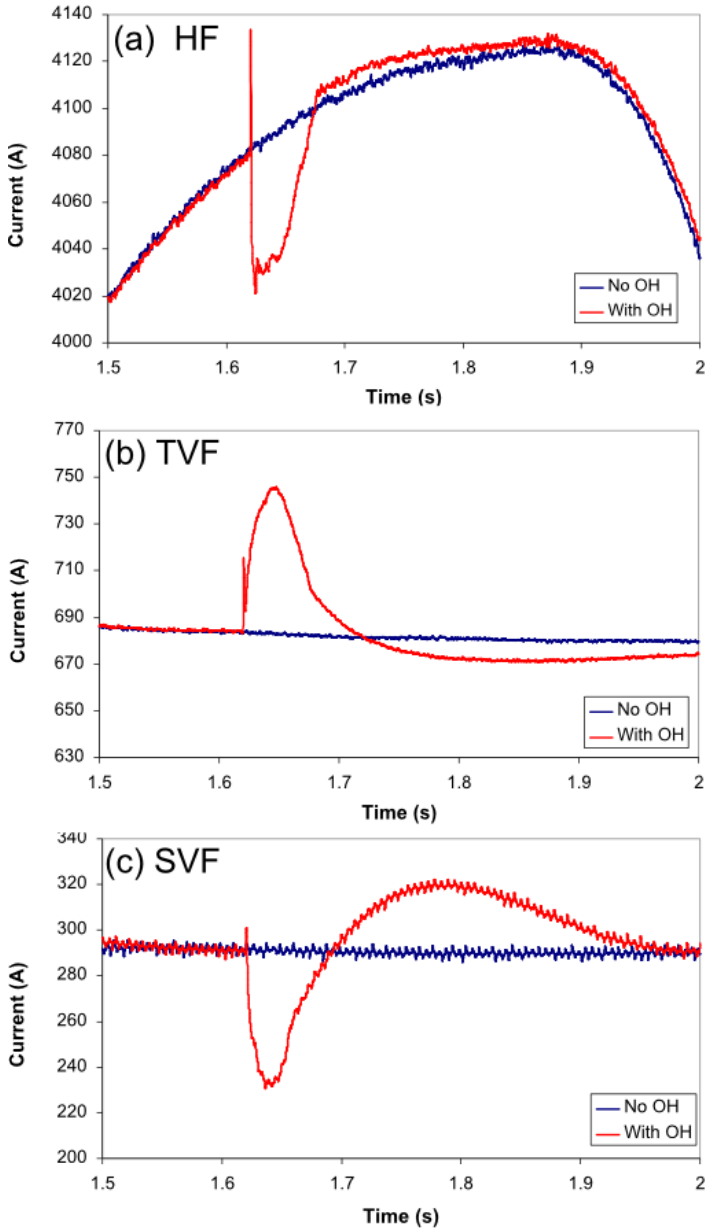

Figure 2.8 – Change in the current measured in the HF/OVF (a), TVF (b), and SVF (c) external coil sets due to inductance with the OH coil

Although the decoupler coils were designed to minimize the currents induced by the OH coil, the currents in the HF, TVF, and SVF coil sets are still affected by the OH induced voltage as shown in Figure 2.8. The current TVF coil configuration utilizes a reduced number of turns compared to the original design. Because of this configuration, the TVFD coil over compensates

for the OH flux, resulting in an increase in the TVF current during the OH discharge (Figure 2.8(b)). This increase in TVF current counters the radial expansion of the equilibrium during current-driven discharges.

To minimize sources of asymmetric magnetic fields, effort was taken to ensure accurate placement of the coils during construction, and the coil feeds were designed to reduce their dipole moments. To accurately determine the final placement of the external coils, a FARO Coordinate Measuring Machine (CMM) was used to measure each coil's position with respect to the helical coil frame. Measurements made using the CMM have a specified accuracy of 0.25 mm relative to the reference coordinate system defined by the helical coil frame.

2.2 CTH vacuum vessel and plasma diagnostics

The toroidal vacuum vessel of CTH is made of Inconel 625 alloy. Inconel was chosen due to its relatively high electrical resistivity and low magnetic permeability. The vacuum vessel is circular in both poloidal and toroidal coordinates. The vacuum vessel has a major radius of R_o= 0.75 m and a minor radius of a_{vv}= 0.29 m. As shown in Figure 2.9, there are five horizontal ports, ten vertical ports, and ten diagonal ports. The mean toroidal angle of each port is located at either a full or half field period where the flux surfaces are up-down symmetric.

Because the continuous helical coil surrounds the vacuum vessel, it was difficult to create a toroidal electrical break in the vacuum vessel that would have eliminated the induced net toroidal current. The vacuum vessel is thus electrically continuous in the toroidal and poloidal coordinates. The average thickness of the vessel wall is nominally 3.8mm. The toroidal electrical resistance was measured to be 0.76 mΩ based on loop voltage and vacuum

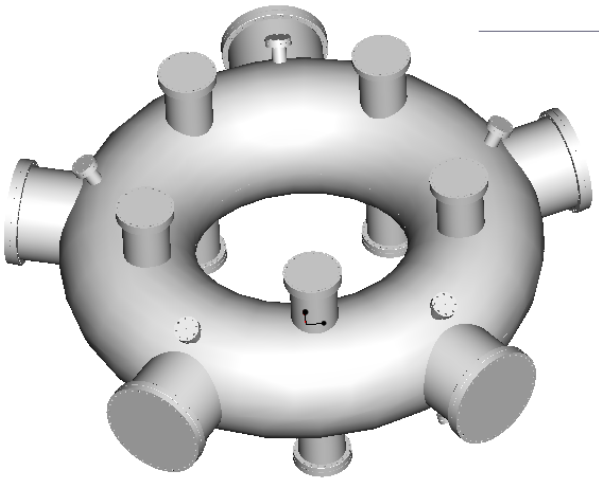

Figure 2.9 – CTH toroidal vacuum vessel

vessel current measurements. Peak toroidal currents in the vacuum vessel have been measured to be greater than 10 kA during OH discharges.

Mounted on the interior wall of the CTH vacuum vessel are a series of poloidal limiters. The material and location of these limiters are shown in Table 2.1. These limiters prevent the plasma from directly contacting the vacuum vessel wall. By localizing the plasma-wall interaction to specific locations and on specific materials, they reduce damage to other internal surfaces and reduce the amount of impurities within the plasma[6]. Due to these limiters there

Material	**Minor Radius**	**Toroidal Angle**	**Poloidal Range**
Molybdenum	26.0 cm	144˚	-150˚ to 150˚
Stainless Steel	26.0 cm	184˚	-30˚ to 30˚
Molybdenum	24.5 cm	300˚	-120˚ to -60˚
Molybdenum	24.5 cm	348˚	60˚ to 120˚
Graphite	18 – 29 cm	216˚	70˚ to 110˚

Table 2.1- Material and location of the four static poloidal plasma limiters on CTH as well as the adjustable limiter

exists a 3 cm gap between the plasma and the vacuum vessel wall. This gap allows magnetic diagnostics to be mounted within the vacuum vessel, and yet remain external to the plasma.

Plasma impurities typically result in increased radiation leading to lower plasma temperatures than in pure plasmas. The impurity content of CTH plasmas is addressed with glow discharge cleaning and titanium gettering. In glow discharge cleaning, the ions of a low temperature plasma are biased to impact the chamber walls with energies of several hundred electron Volts. This plasma discharge is found to reduce the water content of the residual gas in the CTH vessel, presumably by removing absorbed water from the plasma-facing surfaces. Titanium gettering involves the evaporation of wires to produce a thin film of titanium on the vacuum vessel wall. This chemically active metal binds gaseous impurities such as oxygen to the wall. Metal deposition can occur not only from this gettering process, but also during glow discharge cleaning due to sputtering. The internal magnetic diagnostics must be shielded during these cleaning processes to avoid the deleterious effects of metal deposition.

The set of magnetic diagnostics installed on CTH include full and segmented Rogowski coils, Mirnov coils, flux loops, Hall probes, and diamagnetic loops. The average plasma density is measured along a single chord using a 4-mm microwave interferometer. There are a series of soft X-ray detectors that measure the plasma emissivity along multiple chords at two toroidal locations. Also, an X-ray spectrometer has recently been installed to measure the plasma temperature. The data from the CTH diagnostics are digitized using a series of data acquisition boards (DAQ). The magnetic diagnostic signals which are discussed in this dissertation are digitized at a rate of 100 kHz.

2.3 Plasma generation in CTH

The plasmas generated within the CTH device are composed of hydrogen. The hydrogen is ionized and then heated by electron cyclotron resonance heating (ECRH). ECRH is dependent on the electron cyclotron frequency which is defined as:

$$\omega_{ce} = \frac{eB}{m_e} \tag{2.4}$$

where e and m_e are the electron's charge and mass respectively, and B is the magnitude of the confining magnetic field. On CTH, the ECRH heating is applied using three microwave klystrons. The first klystron operates at a frequency of 14.0 GHz which is resonant at a magnetic field strength of 0.50 T. The other two klystrons operate at a frequency of 17.65 GHz, which is resonant at a field strength of 0.63 T. The combination of these three klystrons provides up to 30 kW of ECRH power to the plasma.

Mark Cianciosa has installed a triple probe on CTH which is capable of measuring the electron temperature during these ECRH heated plasmas. The measured electron temperature is typically 10eV. The densities of plasmas in CTH that are heated only by ECRH are limited to an electron density of approximately 4×10^{18} m^{-3}. This density corresponds to the cutoff density above which the plasma becomes highly reflective to the microwave heating sources and the heating efficiency is greatly reduced.

The average electron density is shown in Figure 2.10(a) for a typical plasma generated in CTH with only ECRH plasma heating. The density remains mostly constant during the 80 ms when the ECRH is applied. For this particular shot, the confining field was generated using the HF/OVF, TVF, and TF coil sets. The flux surfaces at two toroidal locations for this field configuration are shown in Figure 2.10(b) as simulated using VMEC. The colored

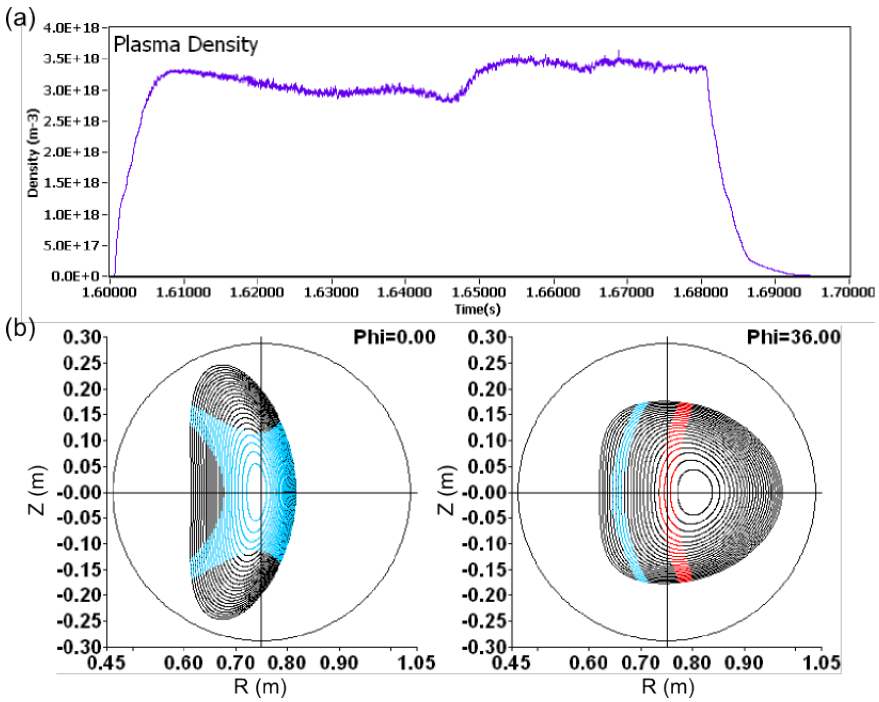

Figure 2.10 – (a) Electron density vs time for ECRH heated plasma (b) corresponding flux surfaces. The ECRH resonances are shown in color. Red shows a field strength of 0.50 T and blue indicates 0.63 T.

portions represent regions where the magnitudes of the magnetic fields are resonant with the ECRH sources.

As described in Sec. 2.1, CTH is also equipped with an ohmic transformer which can be used to further heat the plasma by inducing a toroidal current within the plasma. During ohmic shots, ECRH is also used to ionize the gas and initially heat the plasma. After 20 ms, the OH capacitor bank is discharged through the OH transformer to produce a toroidal loop voltage. This loop voltage drives toroidal current within the plasma and the conducting vacuum vessel. An example of the measured loop voltage and the current driven in the plasma is shown in Figure 2.11(a). With the addition of the plasma current, the average radial position of the magnetic flux surfaces moves outward, and the shape is radially elongated as shown with VMEC surface of section plots in Figure 2.11 (c). The additional heating from the plasma current allows the

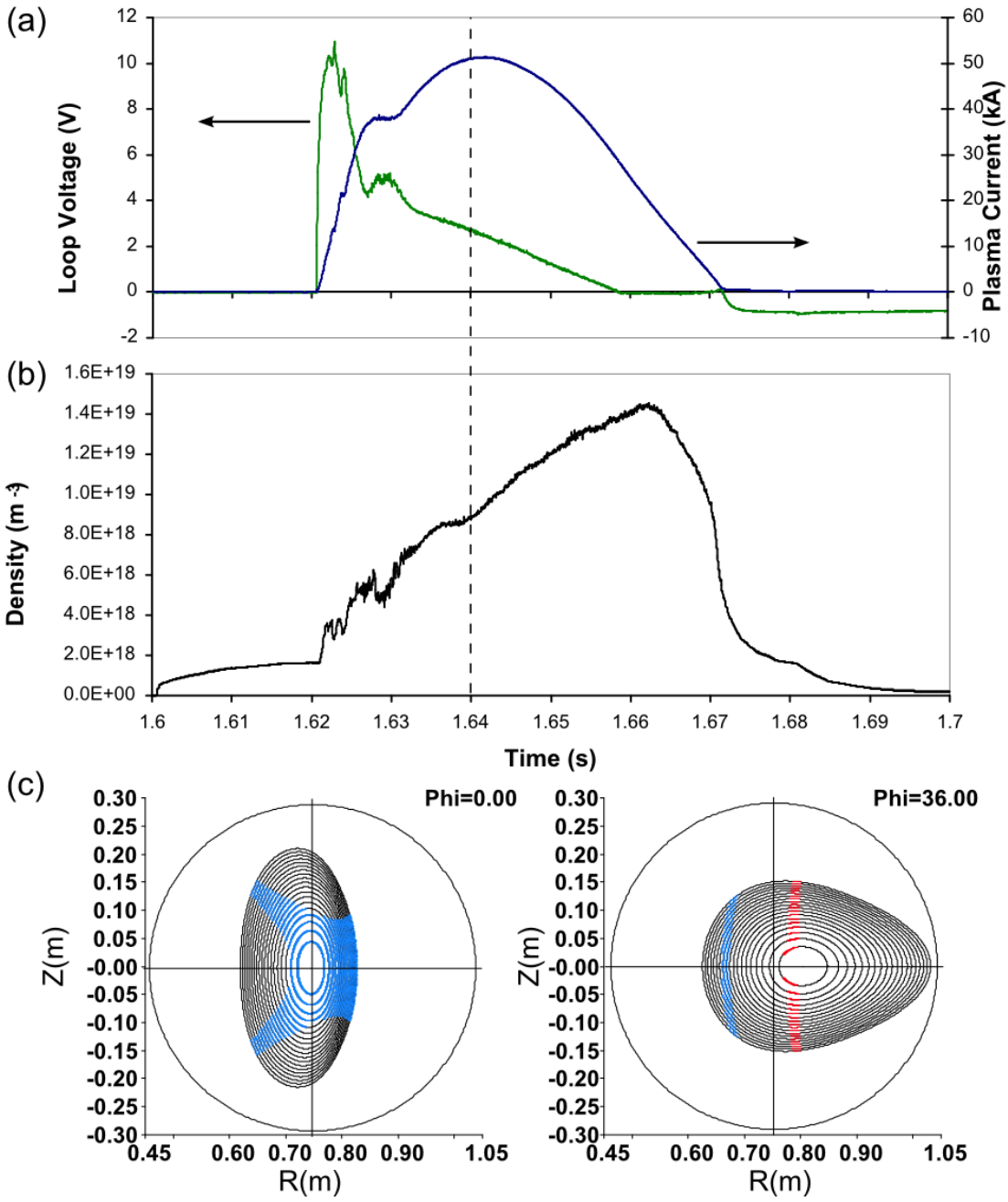

Figure 2.11 – (a) Loop voltage (green) and Plasma current (blue) and (b) line-averaged electron density versus time for typical Ohmic discharge. (c) flux surfaces at the two symmetry planes for t=1.64s into the shot

electron density to be increased above the cutoff density of the ECRH systems (shown in Figure 2.11 (b)). Because of the higher energy content of ohmic discharges, the triple probe cannot be used to measure plasma parameters except at the edge. The plasma temperature can be estimated

from the Spitzer resistivity[6]. The procedure is described in Appendix A.1. The central plasma temperature determined from the measured loop voltage and plasma current values at t = 1.64 s in Figure 2.11 is 220 eV. Measurements of soft X-ray Bremsstrahlung, with an X-ray spectrometer indicate that the central temperature of the plasma during current driven discharges is in the range 150 – 300 eV. This is similar to the value calculated using the Spitzer resistivity.

3 Magnetic Diagnostics on CTH

Magnetic field measurements are routinely used to determine and control the shape and position of magnetized plasmas[6,26,27]. Magnetic diagnostics are used to determine the magnitude and distribution of currents within the plasma[6,28]. They are also used to identify various MHD instabilities[6,29]. Magnetic diagnostics are also used to reconstruct plasma equilibria[21,30]. Strait et al. has recently reviewed the role of magnetic diagnostics in magnetically confined fusion energy experiments[31].

The magnetic diagnostics on CTH consist of full and segmented Rogowski coils, Mirnov coils, flux loops, Hall probes, and diagmagnetic loops. The results in this dissertation are obtained from measurements using the Rogowski coils and Hall probes, all of which are oriented to measure the poloidal component of the magnetic flux at multiple toroidal and poloidal locations. Measurements from these magnetic diagnostics have been used in conjunction with the V3FIT code to help determine CTH plasma equilibria.

3.1 Description of magnetic diagnostics

The local or average magnetic flux is typically measured using simple loops or coils of wire. The response of a basic magnetic diagnostic coil to a magnetic flux is obtained from the integral form of Faraday's Law as applied to a simple loop of wire:

$$\oint_C \mathbf{E} \cdot d\mathbf{l} = -\int_S \frac{\partial \mathbf{B}}{\partial t} \cdot d\mathbf{S} \tag{3.1}$$

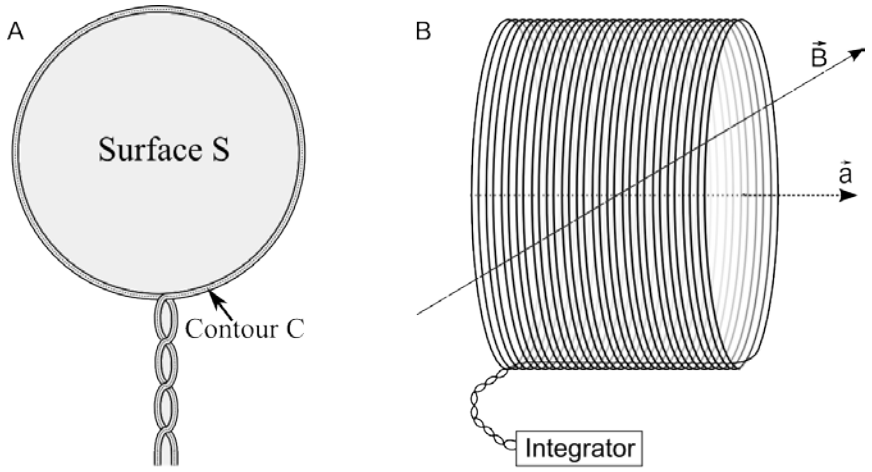

Figure 3.1 – (a) Simple flux loop with twisted leads (b) Solenoidal pickup coil wound over the return feed with a twisted pair connected to an integrator.

where $\oint_C \mathbf{E} \cdot d\mathbf{l}$ is the line integral of the induced electric field around the loop of wire defined by the contour C bounding the surface S as shown in Figure 3.1(a). The line integral is equivalent to an EMF (V):

$$V = -\oint_C \mathbf{E} \cdot d\mathbf{l} \tag{3.2}$$

The integral on the right side of equation 3.1 is the time derivative of the magnetic flux (Φ) through the surface S:

$$-\frac{d}{dt}\int_S \mathbf{B} \cdot d\mathbf{S} = -\frac{d}{dt}\Phi \tag{3.3}$$

Because the flux is the required quantity, the output voltage of the coil is electronically integrated to give:

$$V_{meas} = -\int_{t_0}^{t} V(t')dt' = \int_S \mathbf{B} \cdot d\mathbf{S} = \Phi \tag{3.4}$$

Generally, a loop consists of multiple turns to provide an increased induced voltage. As shown in Figure 3.1(b), the diagnostic coil consists of a solenoid with cross sectional area A, number of turns per unit length of n, and length **l**. The flux through the solenoid is:

$$\Phi = n\int_l\int_A dA\,\mathbf{B}\cdot d\mathbf{l} = nA\int_l \mathbf{B}\cdot d\mathbf{l} \tag{3.5}$$

where $\int_l \mathbf{B}\cdot d\mathbf{l}$ is the line integral of **B** averaged over the cross-section of the loop.

A Rogowski coil consists of a solenoidal coil that closes on itself as shown in Figure 3.2(a). The coil is typically wrapped around a current-carrying conductor (bus bar, plasma, etc.) to measure the total current through application of Ampere's law:

$$\frac{\Phi}{nA} = \oint_l \mathbf{B}\cdot d\mathbf{l} = \mu\, I \tag{3.6}$$

where μ represents the magnetic permeability of the solenoid core, and I is the current enclosed by the Rogowski coil. The measurement of flux is nominally insensitive to the location or distribution of the current within the enclosed area bounded by the curve l, and so is used to measure the total current enclosed. Information of the spatial variation of the current may be obtained with a set of segmented Rogowski coils as shown in Figure 3.2(b). A segmented Rogowski coil set is a series of pickup coils each spanning a fraction of the 360° poloidal angle. For example, each segment of the 8-part Rogowski coil shown in Figure 3.2(b) would span 45°.

3.2 Rogowski Coil Construction

Nineteen sets of both full and segmented Rogowski coils are installed on CTH. Seventeen of these Rogowski coils are each oriented so that they measure the poloidal magnetic flux. The locations of these coils on CTH are shown in Figure 3.3. Twelve of the Rogowski coils are

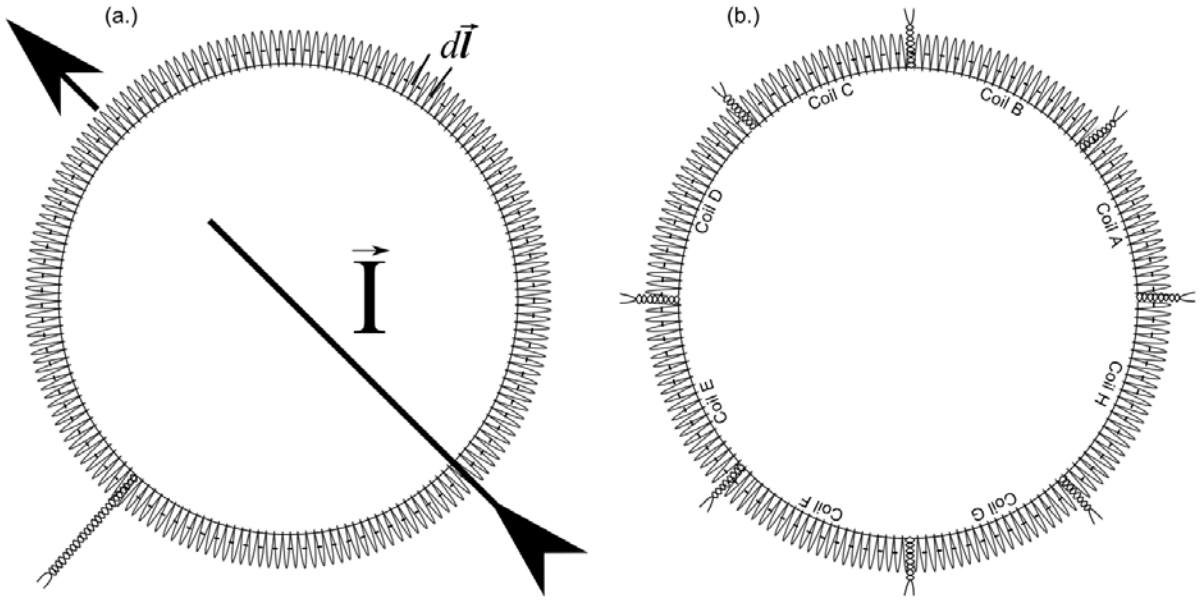

Figure 3.2 – (a) Full Rogowski coil enclosing the current to be measured. (b) Segmented 8-part Rogowski Coil. Note the coils are wound over a return lead and the leads are twisted to minimize measurement of flux along I direction.

mounted on the outside of the vacuum vessel. Portions of these external coils as well as several poloidal flux loops can be seen in Figure 3.4. The external coils consisted of two full, six 4-part, and four 8-part Rogowski coil sets.

Five Rogowski coils are mounted on the interior wall of the vacuum vessel. The locations of these coils are also shown in Figure 3.3. The internal coils consist of two full and three 8-part Rogowski coil sets. One full (1PI264) and one 8-part (8PI264) internal Rogowski coils are shown in Figure 3.5 and are mounted on the inner wall of the vacuum vessel. The labeling scheme 8PI264 refers to an 8-part, internal Rogowski located at $\varphi = 264^{\circ}$. The internal coils are used for performing equilibrium reconstruction. The difference signals between internal and external full Rogowski coils provide a measurement of the current induced in the vacuum vessel during ohmic discharges.

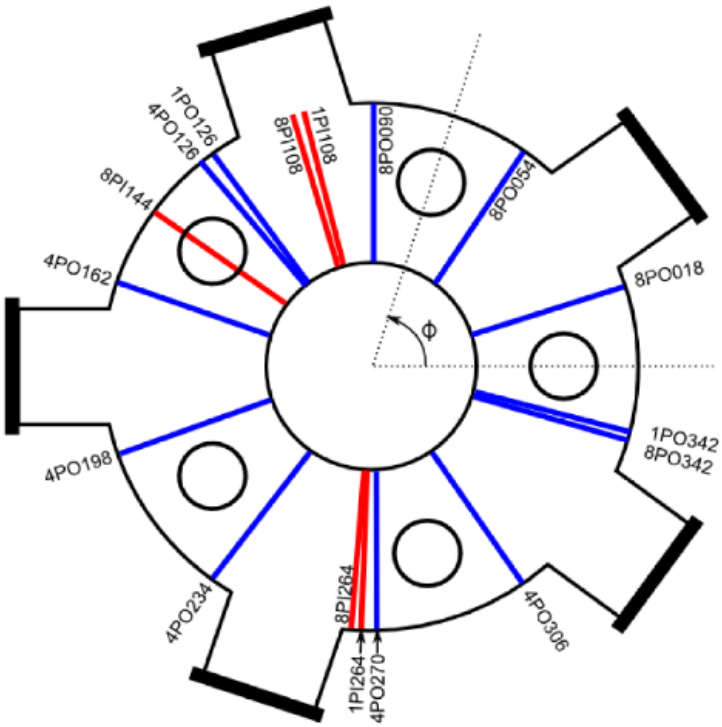

Figure 3.3 – Rogowski coil locations: External coils are shown in blue, and internal coils are shown in red.

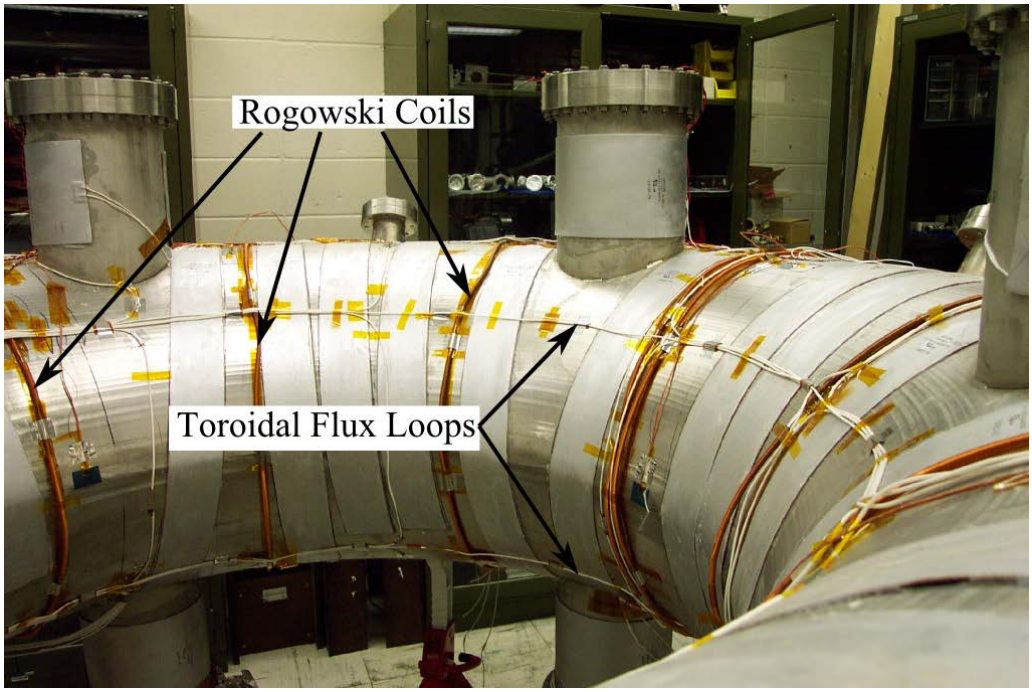

Figure 3.4 – Magnetic diagnostics external to the vacuum vessel prior to being installed within the helical coil frame.

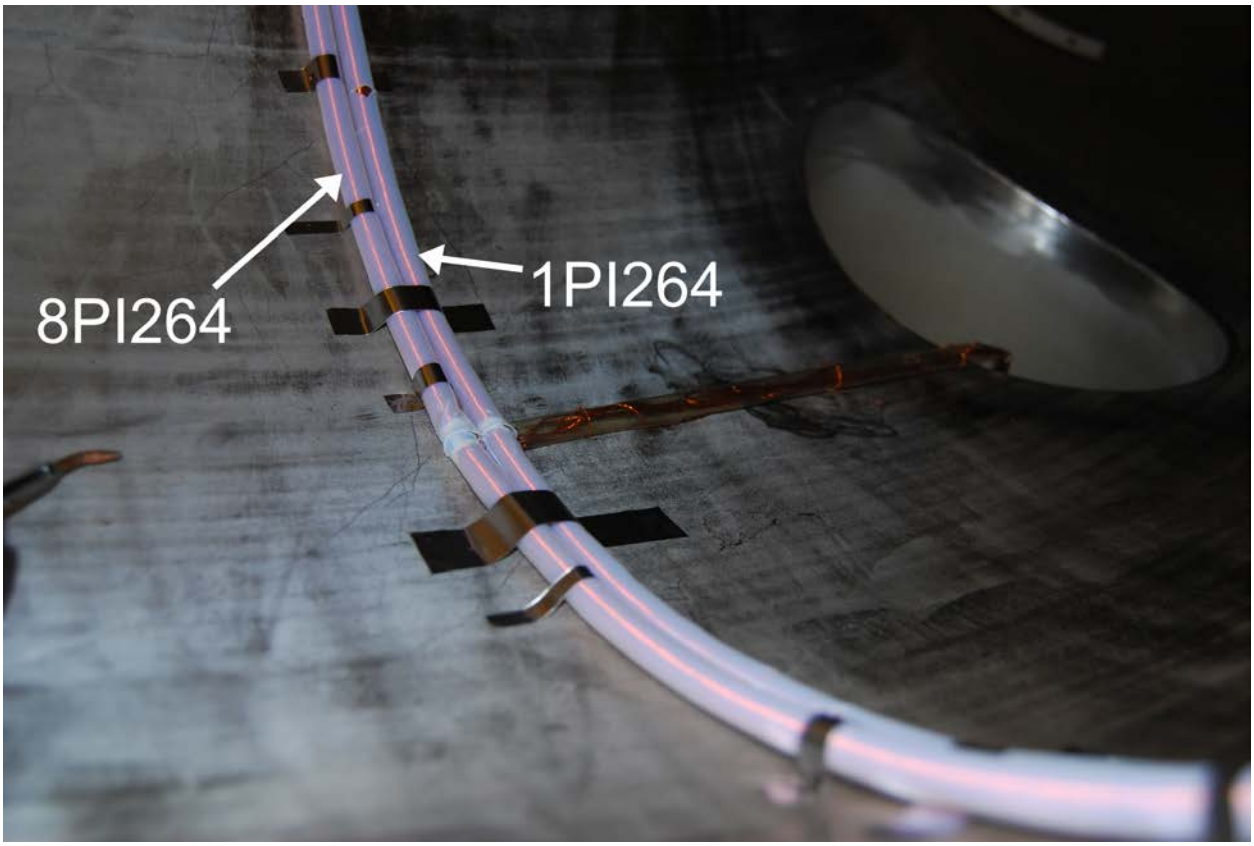

Figure 3.5 – 8PI264 and 1PI264 Rogowski coils mounted on the interior vacuum vessel wall prior to being covered with shim stock

There are additional Rogowski coils used on CTH other than the toroidal coils shown in Figure 3.3. In addition to the toroidal current driven in the vacuum vessel, there are significant eddy currents induced in the elements of the HF coil frame during the ohmic phase of the discharge. Two Rogowski coils were used to measure a portion of the eddy currents in the coil frame to assist in modeling. The red coil shown in Figure 3.6 demonstrates the mounting location of these coils. The locations and characteristics of the Rogowski coils installed on CTH are given in Table 3.1. Many external Rogowski coils have failed since construction and are inaccessible to repair.

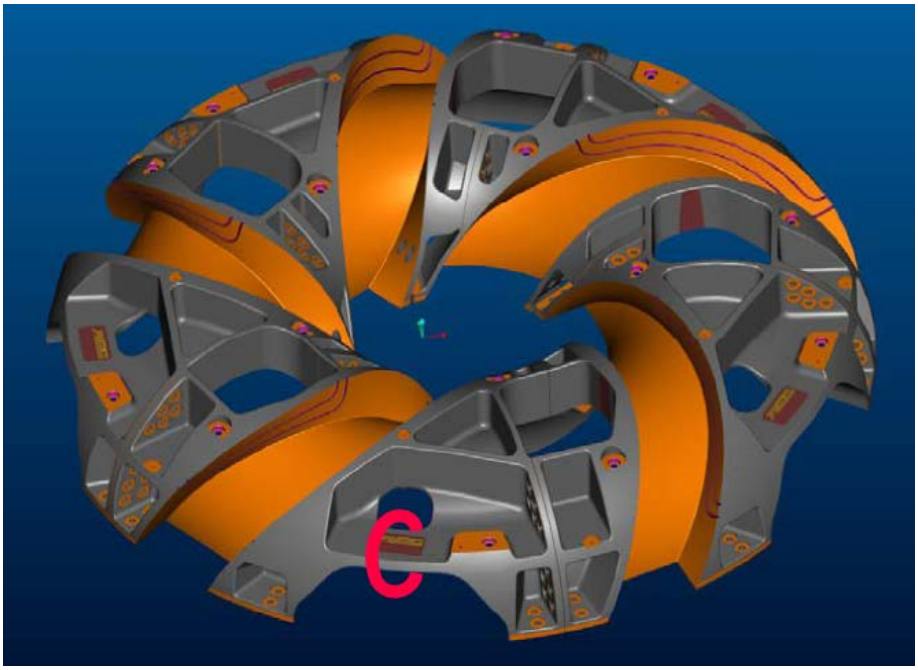

Figure 3.6 – Mounting configuration of Rogowski coil (shown in red) used to measure portion of coil frame current

Identifier	Toroidal Angle	Mounting Location	# of Segments	Coil Winding
8PO018	18˚	External Vac. Vessel	8	Single
8PO054	54˚	External Vac. Vessel	8	Single
8PO090	90˚	External Vac. Vessel	8	Single
1PI108	108˚	Internal Vac. Vessel	1	Single
8PI108	108˚	Internal Vac. Vessel	8	Single
1PO126	126˚	External Vac. Vessel	1	Single
4PO126	126˚	External Vac. Vessel	4	Single
8PI144	144˚	Internal Vac. Vessel	8	Double
4PO162	162˚	External Vac. Vessel	4	Single
4PO198	198˚	External Vac. Vessel	4	Single
4PO234	234˚	External Vac. Vessel	4	Single
8PI264	264˚	Internal Vac. Vessel	8	Double
1PI264	264˚	Internal Vac. Vessel	1	Double
4PO270	270˚	External Vac. Vessel	4	Single
4PO306	306˚	External Vac. Vessel	4	Single
8PO342	342˚	External Vac. Vessel	8	Single
1PO342	342˚	External Vac. Vessel	1	Single
HCF F ROG	252˚	Top HF Coil Frame	1	Double
HCF C ROG	252˚	Bottom HF Coil Frame	1	Double

Table 3.1 – Properties of diagnostic Rogowski Coils on CTH

Each of the full Rogowski coils on CTH was calibrated prior to being installed by measuring their output voltage while enclosing an AC current. This AC current is measured using a 0.1Ω resistor with a resistance tolerance of 0.1%. All of the Rogowski coils on CTH are wound on a 6.35 mm diameter polytetrafluoroethylene (PTFE) core using polyimide-coated (Kapton) 30 gauge copper magnet wire. Experience has shown that abrasion of the polyimide insulation led to electrical short circuits of some coils to the vacuum vessel. Subsequently constructed Rogowski coils inside the vacuum vessel were each placed inside a PTFE tube of wall thickness 0.35 mm. All of the interior magnetic diagnostics are further shielded from the plasma by being placed inside stainless steel tubing, or covered with shim stock. The twisted pair leads were also covered with shim stock to prevent erosion and metal deposition during plasma discharges, glow discharge cleaning, and titanium gettering.

Physical Rogowski coils inevitably have various sources of parasitic pick-up which must be minimized to reduce systematic error in equilibrium reconstruction. The Rogowski coils first installed on CTH consist of a single helical coil wound from one end to the other. The helically-wound coil can be represented as the superposition of an ideal solenoid and an axial lead running the length of the Rogowski coil. The axial lead creates a single loop that responds to the toroidal flux. To compensate for this unwanted pickup, the return lead in this design is placed along the surface of the PTFE core, and the coil is wound over top of this lead. Due to the fact that the return lead path does not lie along the axis of the coil, there exists a small difference in the effective area of the loops that pick up the toroidal flux. To minimize the measured toroidal flux, newer magnetic diagnostic coils are wound with two layers. The return wire forms a second coil wound on top of the first. This method of double winding eliminates the effective toroidal flux loop, and also increases the signal by doubling the number of turns per unit length.

There are other sources of parasitic pickup in the magnetic diagnostic signals. It should be noted that the surface S referred to in Eq. (3.1), actually includes not only the large circular region shown, but also the area enclosed by the leads, as shown in Figure 3.1. The contribution in this region is minimized by twisting the leads which on average cancels out the additional flux pickup. However, there may still be significant parasitic pickup near electrical feed-throughs where the leads often cannot be tightly twisted. When accounting for these sources of pickup, Eq. (3.1) can be written as:

$$\oint_C \mathbf{E}\cdot d\mathbf{l} = \int_{coil} \mathbf{E}\cdot d\mathbf{l} + \int_{leads} \mathbf{E}\cdot d\mathbf{l} = -\int_S \frac{\partial \mathbf{B}}{\partial t}\cdot d\mathbf{a} \qquad (3.7)$$

where the contour integral is written as a sum of the contribution through the coil section and that through the leads.

Each of the internal Rogowski coils has one or more twisted pair conductors that are fed through a vacuum vessel port with a bayonet type 32-pin connector. Cables consisting of shielded twisted pair conductors are connected to these feedthroughs bringing the signals to the analog integrator boards. The integrator circuit design was provided by J Sarff of the University of Wisconsin / Sterling Scientific. The integrated signals are amplified and then directed to the data acquisition system (DAQ).

3.3 Hall Probe Construction and Calibration

To further improve the reconstruction of CTH plasmas, an array of Hall effect sensors was built that can be inserted into the plasma to measure the local poloidal magnetic field internal to the plasma itself. The Hall probe array design is based on similar designs which have been successfully implemented on tokamak experiments including PEGASUS[32], HBT-EP[33], and TEXTOR[34]. Hall effect sensors consist of a semiconductor through which a current **J** is passed (Figure 3.7). When the sensor is placed in a magnetic field, the charge carriers (electrons or

holes) experience a Lorentz force perpendicular to both the current and the field to produce a Hall voltage.[28]

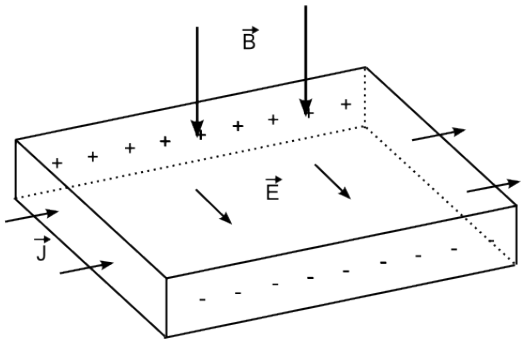

Figure 3.7 – Schematic showing effect of Lorentz force within a Hall effect sensor.

The function of a Hall sensor as a plasma diagnostic is similar to that of the magnetic pickup coils described in the previous section, in that they both measure the local magnetic field. Unlike a magnetic pickup coil, the Hall sensor directly measures the magnetic field without integrators. Also, Hall sensors can be only a few millimeters in size providing highly localized measurements of the magnetic field. The small size facilitates their inclusion into a probe that can be inserted into the plasma. The Hall array built for CTH consists of 16 GH-701 Gallium Arsenide (GaAs) sensors manufactured by Sypris Test & Measurement[35]. The GH-701 sensor has an active area of

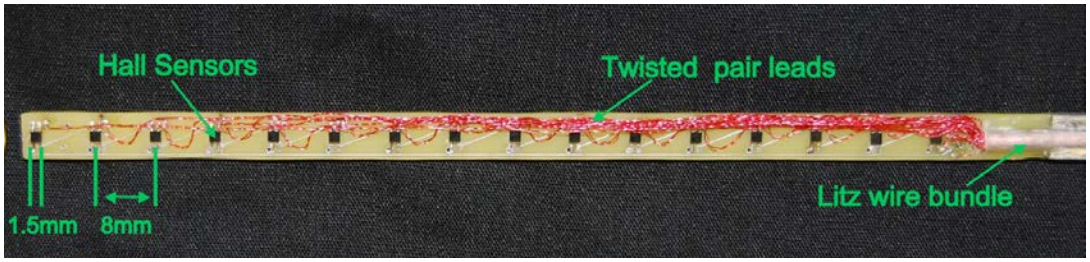

Figure 3.8 – Array of 16 Hall sensors connected in series with twisted pair leads emerging from a Litz wire (white).

1.5 x 1.5 mm. As shown in Figure 3.8, these sensors are mounted onto a printed circuit board (PCB) with an 8mm separation between adjacent sensors. When mounted, the sensor surface is nominally parallel to the surface of the PCB.

The sensitivity of each Hall sensor to the local magnetic field depends on the bias current through it. To ensure that the sensitivity of each sensor is identical, the bias current of 8.18 mA is connected in series to each of the 16 sensors. The Hall voltage from each sensor was carried using a twisted pair of 36 gauge wires which emerges from a 65 conductor Litz wire bundle (see Figure 3.8). The output voltages of the Hall sensors are fed into differential amplifiers with a gain of 20. The amplifier outputs are then connected to the DAQ system.

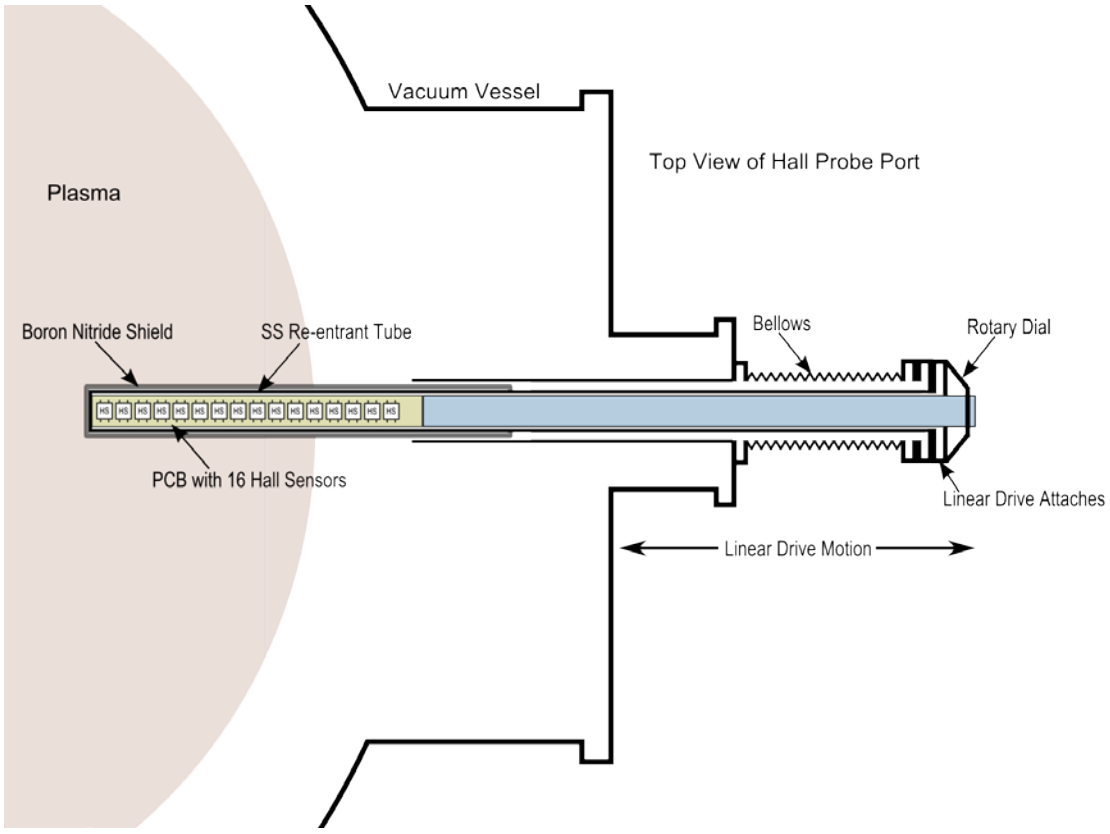

Figure 3.9 – Hall Probe Array assembly – Top view

The Hall probe array assembly mounted onto a side port of CTH as shown in Figure 3.9. The probe is located inside a re-entrant 8 mm diameter stainless steel tube with 0.9 mm thick walls. The Hall sensor PCB is connected to a long aluminum strip which allows the array to be fully inserted into the re-entrant tube and pivoted about its axis. For ease of alignment, the aluminum strip is mounted to a rotary dial with a degree scale. The rotary adjustment allows the Hall sensor array to be aligned to measure only the poloidal component of the magnetic field. The angular calibration is performed as follows. The array is moved to the inward most position and the background Hall voltage for sensor 1 is measured at three angular positions spanning 20 degrees. The background signal changed less than 0.5% and is consistent with the expected signal change from measurement of the local earth's field. Next, 400A was applied to the TF coil set and the voltage for sensor 1 was again measured at the three angular positions. With the field produced from the TF coil, the Hall voltage changed 66% over the same 20 degree span. The angle was adjusted until the signal was the same as the background level ensuring that the Hall sensor array was perpendicular to the toroidal field.

The outer end of the re-entrant tube is connected to a motorized linear slide. The linear slide in combination with a bellows allows the probe assembly to be moved radially within the vacuum chamber. The linear slide was positioned using the coordinate measuring machine (CMM) to lie nominally along the mid-plane at a toroidal angle of 180˚. Once the slide was placed, CMM measurements were made for a series of different probe positions to determine the final orientation of the slide. A linear fit was applied to these measurements to determine the precise direction of probe travel. The linear position of the probe is controlled with a Vexta PK266 model stepping motor and a Velmex VXM controller with a specified precision of 0.01 mm per step.

A Boron Nitride (BN) tube is placed around the stainless steel tube housing the probes to prevent the metal tube from providing a conducting path across the plasma flux surfaces. The BN tube is 1.27 cm in diameter and closed on the end inside the plasma. Boron Nitride was chosen based on previous results[36] that showed excellent thermal and electrical resistance while also producing less plasma density changes than the other probe materials studied. To prevent metal deposition on the BN shield during glow discharge cleaning and titanium gettering, the probe assembly recesses into a 1 inch diameter stainless steel tube. A simple shutter at the end of the tube closes when the assembly is fully retracted.

The calibration of the magnetic field response of the Hall sensors is performed in two stages. The sensors are initially calibrated at relatively low magnetic fields to obtain the sensitivity of each detector, defined as the ratio of the output voltage to the magnetic field. A set of Helmhotz coils provided the calibration magnetic field. The Hall sensors were found to have an average sensitivity of 1.46 V/T, consistent with the manufacturer's specifications. While the ideal Hall probe responds only to the magnetic field component perpendicular to its active surface, previous tests using InSb Hall sensors indicated that the probe's sensitivity to fields perpendicular to the surface varies when a strong parallel field is present[32,33]. This is a concern because the toroidal magnetic field in CTH within the plasma is normally many times stronger than the poloidal field.

Because this sensitivity variation due to parallel fields was unknown for the GH-701 Hall sensors, a calibration setup was prepared that makes use of two orthogonal sets of Helmholtz coils to provide magnetic fields perpendicular and parallel to the Hall probe surface, as shown

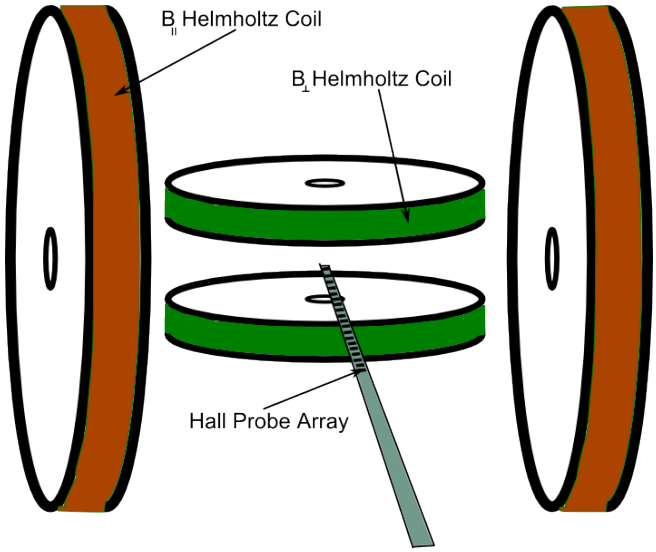

Figure 3.10 – Schematic of the double Helmholtz calibration stand used to determine Hall Probe sensitivity

in Figure 3.10. Both Helmholtz coils in this assembly were calibrated using a Bell Teslameter. The parallel field corresponds to the toroidal field in CTH, while the perpendicular field corresponds to the poloidal field, the component of interest to reconstruction.

The output voltage of one sensor is plotted versus the perpendicular field for three different values of the parallel field in Figure 3.11(a). The measured sensitivity determined using the Helmholtz coils remained constant at 1.50 V/T for each parallel field tested. The maximum magnetic field that could be achieved was 0.035 T using the Helmholtz coils. This magnetic field strength is less than one tenth the typical

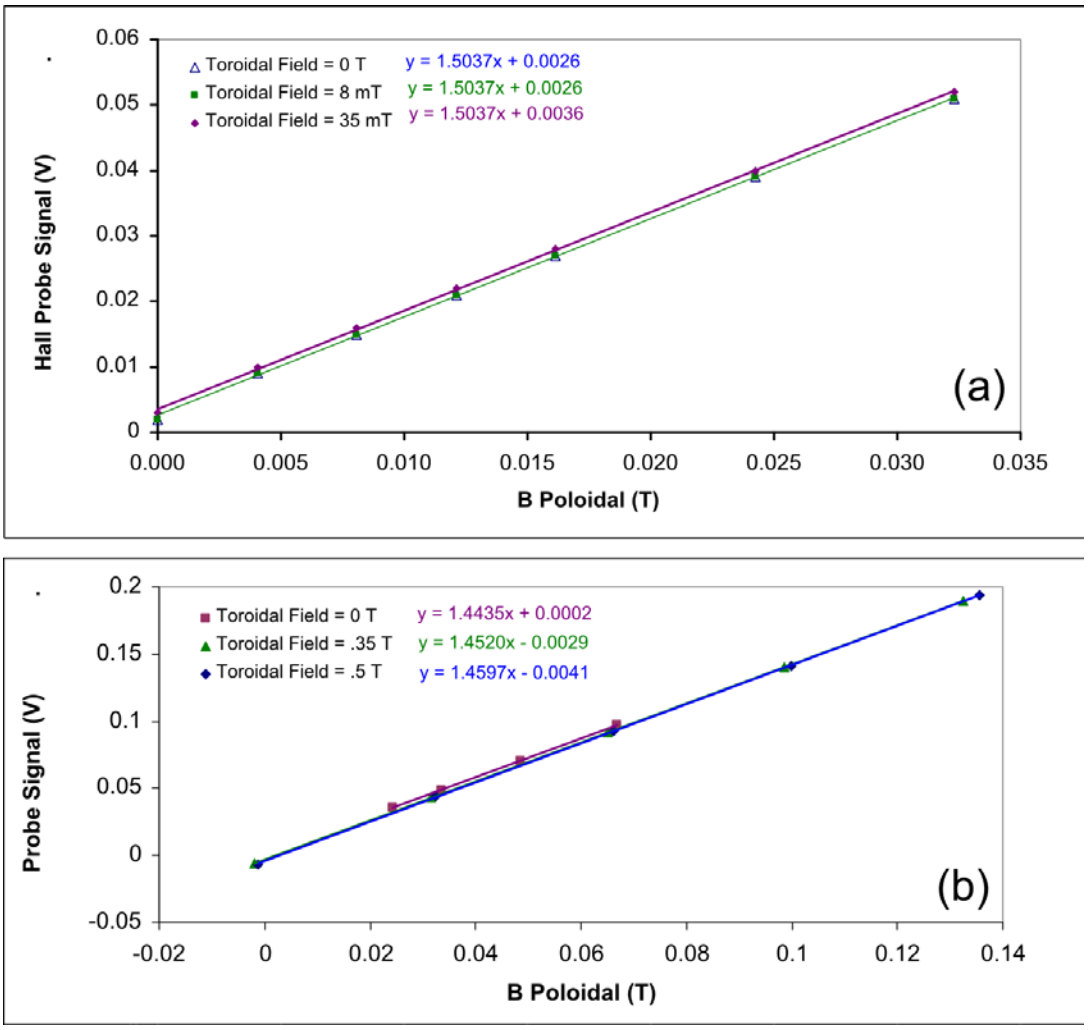

Figure 3.11 – Effect on Hall Probe 1 output voltage versus poloidal field when low (a) and high (b) toroidal field strengths are applied. The lines indicate linear fits to the data, and the legend indicates the fitted sensitivity in (V/T).

toroidal field strength of 0.5 T in CTH. Further calibrations of the sensors were performed *in situ* using the known "vacuum" fields of the CTH configuration. The results of this in situ calibration for three higher values of the parallel field are shown in Figure 3.11(b). During this test, the measured sensitivity remains in the range 1.45 V/T ± 1%. The change in average measured sensitivity from the results obtained using the Helmholtz coils and those from the in situ CTH test can be attributed to a design modification of the amplifier circuit which was performed between these two tests.

The sensitivity of Hall effect sensors is also known to be a function of temperature. The sensitivity of the InSb Hall sensors used on PEGASUS[32] and HBT-EP[33] were specified to change by up to 2%/°C. The array installed on HBT-EP was also equipped with thermistors to monitor and account for this temperature change[33]. The GaAs Hall sensors of the CTH array are less sensitive to temperature changes, with a stated temperature sensitivity of 0.06 %/°C. Nonetheless, the temperature of the probe array is monitored with thermistors. Two thermistors are mounted onto the back side of the PCB as shown in Figure 3.12. The ability to directly measure the probe temperature with these thermistors makes it possible in principle to adjust the calibrated probe sensitivities to account for temperature changes. The Hall sensors are also

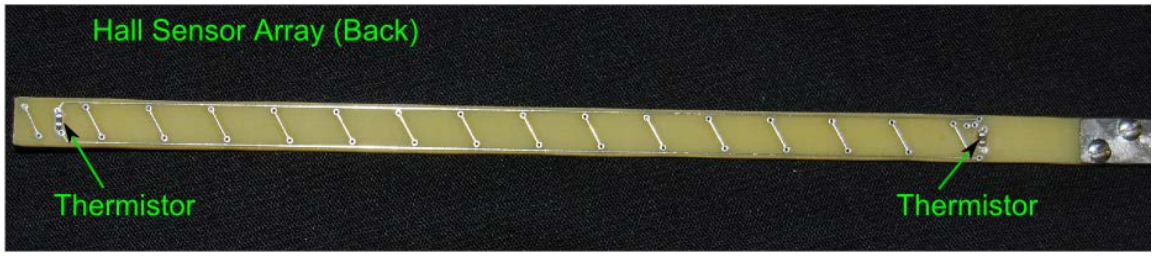

Figure 3.12 – Back of Hall sensor array showing two thermistors integrated into design for temperature measurement.

actively cooled by flowing compressed air over the sensors during operation. Currently, temperature corrections have not been found to be necessary due to the small temperature sensitivity of the GH-701 sensors as well as the active cooling.

3.4 Diagnostic placement and measurement

The process of equilibrium reconstruction minimizes the difference between modeled diagnostic signals and those experimentally determined. Precise measurements of the magnetic diagnostics positions and their orientations are critical to accurately reconstruct plasma

equilibria. It has been necessary to develop a model which describes the placement of the actual diagnostics.

Conceptually, the Rogowski coils were designed to lie in a poloidal plane at a constant toroidal angle. Each segment of a circular array was to lie at the same average minor radius. In practice, the vacuum vessel to which the coils are mounted does not have a perfectly circular cross-section. Furthermore, three of the inner Rogowski coil sets are contained within rigid nearly semi-circular stainless steel tubes mounted on the inner wall of the vacuum vessel. The tubes do not maintain their semi-circular shape when they were installed into the vacuum vessel. This coupled with the fact that the vacuum vessel has a non-circular cross section results in both radial and toroidal deviations of the diagnostic locations from their conceptual placement.

To improve the accuracy of the reconstructions from magnetic diagnostics, the coordinate measuring machine (CMM) was used to accurately place the magnetic diagnostics along a toroidal plane. The CMM measurements were also used to determine the actual position and orientation of these coils once they were installed.

The Rogowski coil arrays 8PI264 and 1PI264 were mounted directly to the vacuum vessel wall, and their locations were directly measured with the CMM prior to being covered with stainless steel shim stock. The measured minor radius and toroidal angle of the 8PI264 coil are shown as a function of poloidal angle in Figure 3.13 (a) and (b) respectively. The CMM measured points have a specified accuracy of ± 0.013 mm. The collection of measured data was fit using Fourier series to develop a model of the exact position and shape of the diagnostic coils to be used within the reconstruction code. Specifically, the Fourier series describing the poloidal dependence of the minor radius and toroidal position are:

$$r(\theta)=\sum_{i=0}^{4}\left[a_i\sin(i\theta)+b_i\cos(i\theta)\right] \qquad \text{and} \qquad \phi(\theta)=\sum_{i=0}^{4}\left[c_i\sin(i\theta)+d_i\cos(i\theta)\right] \qquad (3.8)$$

These nine terms in each of Fourier series were used to model the curves of each Rogowski coil set as shown by the solid curves in Figure 3.13.

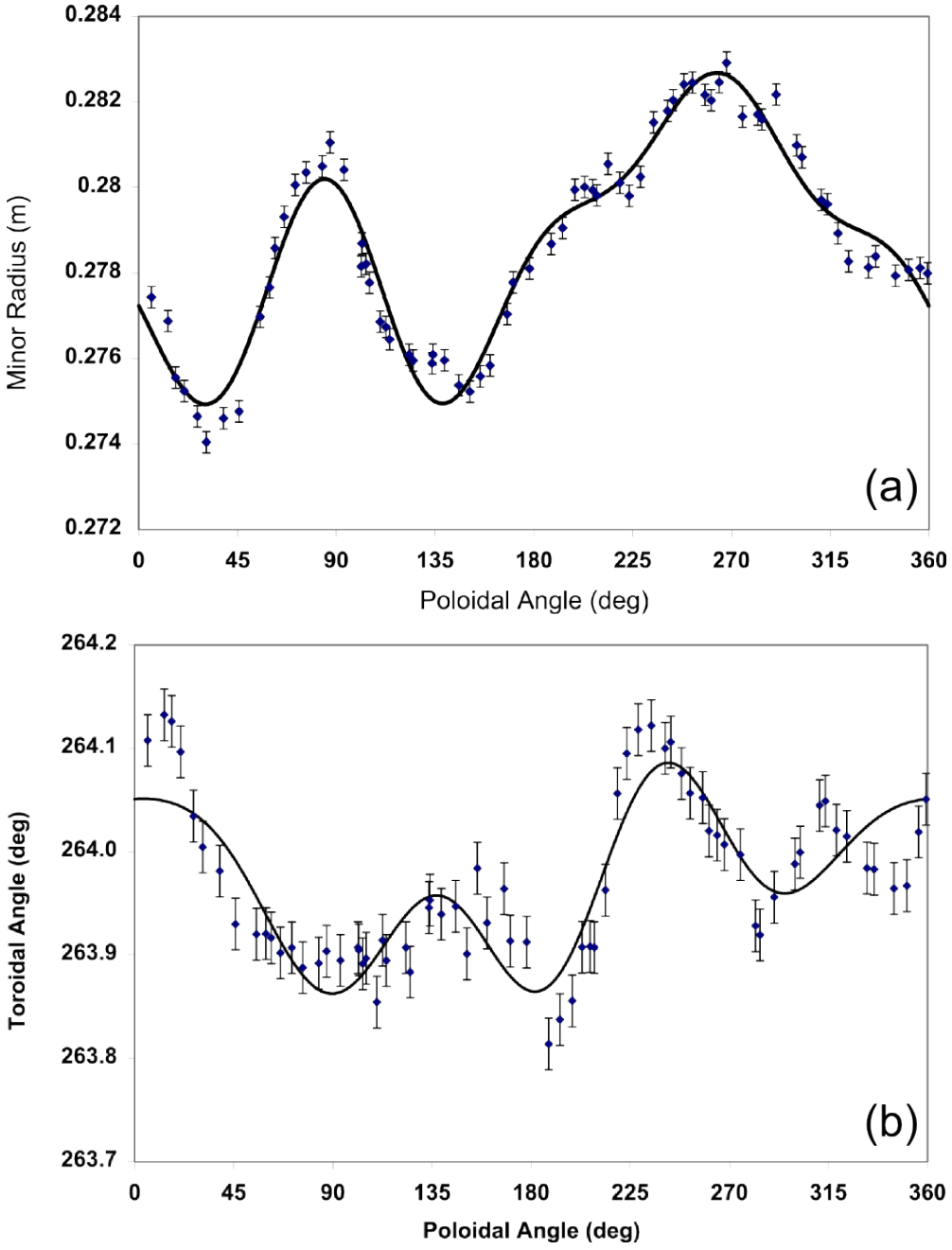

Figure 3.13 – Measured (a) minor radius and (b) toroidal angle of Rogowski coil 8PI264 versus poloidal angle. The black curves are Fourier series fits to the data. Error bars represent the ± 0.013 mm accuracy of the CMM.

Direct measurement of the locations of the three Rogowski coils placed within the stainless steel tubes was not possible, but the CMM was used for accurate placement of the tubes themselves. The CMM measurements of the tubes were then used to model the positions of Rogowski coils they enclosed. An additional 6.4 mm radial offset was added to these position measurements to account for the radius of each tube enclosure. Similar to the method just described for 8PI264, a Fourier series fit to these measurements was used to model coils 8PI108 and 8PI144.

4 Computational Method of Reconstruction

4.1 VMEC Equilibrium Solver

VMEC is an ideal MHD equilibrium solver that is used to calculate the 3D nested flux surfaces in toroidal plasmas[19]. MHD equilibria are found in VMEC through an iterative process in which the total energy of a plasma confined in a volume V_p is minimized subject to the constraints of ideal MHD. This total energy includes the magnetic and thermal energy components and can be represented as:

$$W_p = \int_{V_p} \left(\frac{B^2}{2\mu_0} + p \right) dV \tag{4.1}$$

The VMEC minimization routine is performed in an inverse coordinate system in which the cylindrical coordinates R and Z are expressed in terms of the flux coordinates s, u, and v. The radial-like coordinate s represents the normalized toroidal flux and is defined as:

$$s \equiv \frac{\Psi_t}{\Psi_{t_{tot}}} \qquad 0 \le s \le 1 \tag{4.2}$$

where Ψ_t is the toroidal magnetic flux within a particular flux surface, and $\Psi_{t_{tot}}$ is the total toroidal magnetic flux contained within the plasma, i.e. the toroidal flux at the plasma boundary. The coordinate v is equivalent to the geometric toroidal angle φ. The coordinate u represents a poloidal-like angular coordinate in a flux-based coordinate system in which the magnetic field

lines appear straight. This is achieved by adding a periodic stream function λ to the poloidal angle θ. The function λ acts as a renormalization parameter and improves the code convergence. Within VMEC, the cylindrical coordinates R and Z, as well as λ, are expressed in terms of the flux coordinates using Fourier series as:

$$R = \sum_{n,m} R_{mn}(s)\cos(mu - nv)$$

$$Z = \sum_{n,m} Z_{mn}(s)\sin(mu - nv) \qquad (4.3)$$

$$\lambda = \sum_{n,m} \lambda_{mn}(s)\sin(mu - nv)$$

The minimization of W_p is performed on a discrete mesh in flux coordinates. At each grid point, W_p is minimized by varying the Fourier amplitudes in Eq. (4.3). The resulting values describe how the equilibrium flux surfaces are mapped into cylindrical coordinates.

The VMEC code can be configured to run in fixed or free boundary mode. For fixed boundary mode, the shape of the outermost flux surface is defined and is held constant while W_p is minimized. With the boundary condition defined, the solution becomes a Neumann boundary value problem with the normal component of B taken to be zero. The values of the external coil currents are not required to achieve a solution, and the code is generally less computationally intensive. However, the shape of the outermost flux surface is typically not known in finite-pressure, current-carrying plasmas, and free-boundary solutions must be pursued. In the free boundary mode, additional input parameters are required to solve the equilibrium condition. Among these input parameters, the current in the external coils must be defined along with a description of the paths of each coil filament. Values for the total toroidal magnetic flux $\left(\Psi_{t_{tot}}\right)$ and the total toroidal plasma current are needed. The solution also requires functions which

describe either the radial profile of the plasma current or the rotational transform profile, and the pressure profile. For the equilibria presented in this dissertation, the pressure profile is described using a power series in the flux coordinate s as:

$$p(s) = p_{scale} \sum_{i=0}^{n} a_m(i)\, s^i \tag{4.4}$$

where the series coefficients a_m determine the shape of the profile, and p_{scale} is an overall scaling factor.

The toroidal current passing through a cross section in the poloidal plane with its normal in the toroidal direction can be represented as:

$$I(s) = \int_0^s \int_0^{2\pi} \mathbf{J} \cdot \hat{e}^v \sqrt{g}\; ds\, du \tag{4.5}$$

Where J is the current density, and $\hat{e}^v$ is the toroidal basis vector. g is the determinant of the metric matrix

$$g^{ij} = e^i \cdot e^j \tag{4.6}$$

where e^i are the basis vectors in the flux coordinate system s, u, v, and e^j are the basis vectors in the cylindrical coordinate system. The VMEC input specifying the current density profile is designated as $I'(s)$ and defined as:

$$I'(s) \equiv \int_0^{2\pi} \mathbf{J} \cdot \hat{e}^v \sqrt{g}\; du \qquad \text{so that} \quad I(s) = \int_0^s I'(s')\, ds' \tag{4.7}$$

Several parameterizations of the current profile have been incorporated into VMEC. One parameterization uses a simple power series as:

$$I'(s) = \left(\frac{I_{tot}}{\sum_{i=0}^{n} \frac{a_c(i)}{i+1}} \right) \sum_{i=0}^{n} a_c(i)\, s^i \tag{4.8}$$

where I_{tot} is the total toroidal plasma current, and $a_c(i)$ are the power series coefficients. The current density $I'(s)$ is assumed to go to zero at the outer most flux surface (s=1). This condition is met when the power series coefficients meet the following condition:

$$\sum_{i=0}^{n} a_c(i) = 0 \tag{4.9}$$

The accuracy of reconstruction depends on the ability of model profiles with adjustable parameters to match the physical profiles, or at least the fields they produce. Other current density profiles used in the course of this work are Gaussian profiles and so-called two-power profiles. Similar to the condition just stated for the power series, the Gaussian current density profile is truncated to ensure the current density goes to zero at s=1, and has the form:

$$I'(s) = I'_0 \left[e^{-\left(\frac{s}{a_G}\right)^2} - e^{-\left(\frac{1}{a_G}\right)^2} \right] \tag{4.10}$$

where a_G is the single parameter that characterizes the peakedness of the profile. I'_0 is a factor that is scaled to deliver the correct (measured) total plasma current.

The two-power profile has the following form:

$$I'(s) = I'_0 \left(1 - s^{\alpha}\right)^{\beta} \tag{4.11}$$

This current density model has two free parameters, α and β, and is capable of simulating peaked as well as extremely flat current density profiles. The factor I'_0 again allows normalization to the total plasma current, and for this parameterization can be written in terms of I_{tot} as:

$$I_0' = \frac{I_{tot}\,\Gamma\left(1+\frac{1}{\alpha}+\beta\right)}{\Gamma\left(1+\frac{1}{\alpha}\right)\Gamma(1+\beta)} \tag{4.12}$$

With these input parameters defined, VMEC can be used to solve the Fourier amplitudes (Eq. 4.3) which describe the spatial locations of the equilibrium flux surfaces. The results from VMEC also include a description of the calculated magnetic field within the last closed flux surface.

4.2 V3FIT Reconstruction Code

Plasma reconstructions in this dissertation were performed using the V3FIT equilibrium reconstruction code[1]. This code is based on VMEC that solves 3D toroidal equilibria given the vacuum fields and current and pressure profiles. The goal of reconstruction is to find the most probable current and pressure profiles of the stellarator plasma consistent with the magnetic measurements. The current and pressure profiles which define the equilibrium are defined by a set of input parameters such as the coefficients of the current density profile ($a_c(i)$) shown in Eq. (4.8). Input parameters which are not measured can be optimized using V3FIT through a process which minimizes the mismatch between experimental diagnostic signals and a corresponding set of modeled signals. The modeled signals are quantities which are simulated measurements and are calculated from the modeled equilibrium. The diagnostic signals used in this dissertation measure the poloidal magnetic flux using segmented Rogowski coils mounted onto the vacuum vessel. A corresponding modeled signal is the magnetic flux averaged over the same geometric location, which is calculated from the magnetic fields produced by the modeled external currents and the VMEC computed plasma equilibrium. Once these input parameters are optimized, the

resulting reconstructed equilibrium should more accurately represent the experimental equilibrium.

The optimization of the input parameters is achieved within the V3FIT code by minimizing the following function:

$$\chi^2(\mathbf{p}) \equiv \sum_i^N k_i \left[\frac{S_i^o(\mathbf{d},\mathbf{p}) - S_i^m(\mathbf{p})}{\sigma_i} \right]^2 \tag{4.13}$$

where N is the number of diagnostics used. The terms, S_i^o represent the observed signals from each of these N diagnostics. These observed signals are dependent on the experimental data (**d**), and can also be a function of the parameters which are being optimized (**p**). In this dissertation, the observed signals are the measured data from the magnetic diagnostics. The modeled diagnostic signals represented by S_i^m are a function of the parameters being optimized. The standard deviation of the observed signals is represented by σ_i. The parameter k_i is a weighting factor that is typically set to one, but could be used to reduce the contribution of a particular diagnostic to χ^2 in the event one believes the data from that diagnostic is suspect. A reasonable reconstruction would result in modeled signals with magnitudes in the range of $S_i^o \pm \sigma_i$. If the weighting factors k_i are assumed to be unity, the expected minimum value of χ^2 would be approximately N.[37]

The quantity χ^2 is minimized by making small changes in the parameters **p** to determine the effect on the model signals $S_i^m(\mathbf{p})$. This is accomplished in V3FIT with the Jacobian matrix:

$$A_{ij} = -\frac{\partial e_i}{\partial a_j} \tag{4.14}$$

that is written in terms of dimensionless vectors. The difference or error vector is defined as:

$$e_i \equiv \frac{\sqrt{k_i}}{\sigma_i}\left[S_i^o(\mathbf{d},\mathbf{p}) - S_i^m(\mathbf{p})\right] \tag{4.15}$$

In terms of this vector, the quantity χ^2 is:

$$\chi^2 = \sum_i e_i e_i \tag{4.16}$$

The normalized parameter vector is:

$$a_j \equiv \frac{p_j}{\pi_j} \tag{4.17}$$

where π_j is a user-assigned normalizing factor. The Jacobian is a measure of how much a small change in the j^{th} parameter will effect the i^{th} model diagnostic signal. During each iteration step, the change in the parameter vector ($\delta\mathbf{a}$) is determined using the method of singular value decomposition[38]. This results in a system of equations such that:

$$\mathbf{A} \cdot \delta\mathbf{a} = \mathbf{e} \tag{4.18}$$

After each step in parameter space ($\delta\mathbf{a}$), the new plasma equilibrium is recalculated using VMEC. This process is repeated until the value χ^2 is minimized. The parameters that minimize χ^2 are used to calculate the fitted equilibrium from VMEC.

The routine used to minimize the χ^2 value is also used to compute the posterior parameter variances[37,39] associated with each reconstructed parameter. These values are the variation in parameter space that results in a similar value of χ^2. These values will be used in Chapter 6 to represent the uncertainty in the reconstructed parameters.

The value of the total toroidal flux enclosed by the plasma is required for VMEC to converge to an equilibrium solution. Practically, this impact parameter is determined by determining where the last closed flux surface is in contact with one or more physical limters.

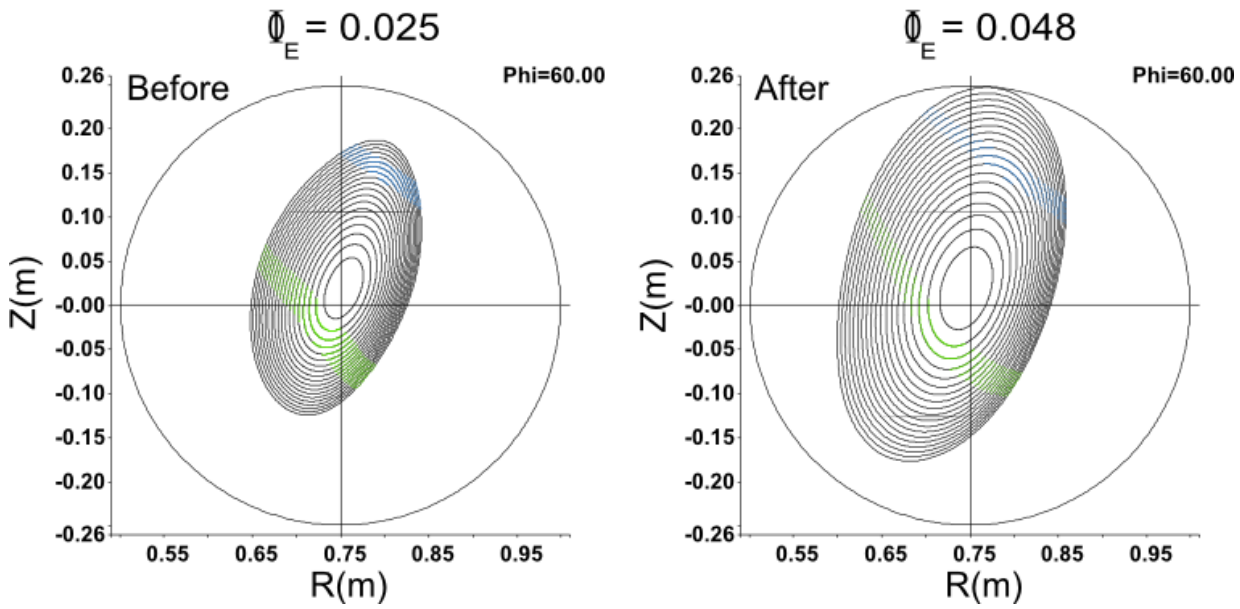

Figure 4.1 – Surface of section plots showing effect of V3FIT optimization of Φ_E, the outer circle is the simulated limiter.

Model limiter surfaces can be defined using simple 2D curves in the cylindrical coordinates (R,Z) in a specified poloidal plane. As geometric curves, they are represented as limiter functions. The distance between the s=1 flux surface and the limiter surfaces are included as modeled signals, such that the χ^2 value increases with distance. The VMEC input parameter that defines the total toroidal flux $\left(\Psi_{t_{tot}}\right)$ is a parameter often used to optimize the radial extent of the last closed flux surface. The example shown in Figure 4.1 displays a set of VMEC calculated CTH equilibria. The outer-most circle shown in each plot of Figure 4.1 represents the simulated limiter function defined within V3FIT. As shown in these plots, the V3FIT optimization of Φ_E results in a last closed flux surface which is adjacent to limiter.

4.3 V3RFUN response function code

The computation of modeled magnetic signals (simulated measurements) could be very time intensive. A process in the V3FIT code called V3RFUN[40] streamlines this procedure.

Similar to the approach used in the EFIT code, a database of diagnostic response functions is generated once for each diagnostic. This greatly increases the speed of equilibrium reconstruction.

The response of magnetic diagnostics in V3FIT is derived using the magnetic vector potential. The magnetic flux measured by a magnetic diagnostic coil, as described by Eq. (3.4), can be written in terms of the vector potential (**A**) as:

$$\Phi = \int_S \mathbf{B} \cdot d\mathbf{S} = \int_S (\nabla \times \mathbf{A}) \cdot d\mathbf{S} \tag{4.19}$$

where the integral is performed over the surface area of each loop comprising the diagnostic. Using Stoke's theorem, the flux can be written in terms of a line integral of the vector potential as:

$$\Phi = \oint \mathbf{A} \cdot d\mathbf{l} \tag{4.20}$$

where **l** is along the 3D curve of the wire elements of the diagnostic coil itself. The flux within the diagnostic coil is comprised of a component from the external current sources and another from the current within the plasma. The flux from each external current source is linearly proportional to the current's amplitude, and so the total flux measured by the j^{th} diagnostic coil can be represented as:

$$\Phi^j_{Total} = \Phi^j_{plasma} + \sum_i M_{ij} I_i \tag{4.21}$$

where Φ^j_{Total} is the total magnetic flux, Φ^j_{Plasma} is the flux from the plasma current, the summation is over the external currents I_i, and M_{ij} is the mutual inductance of the i^{th} current to the j^{th} diagnostic coil. Similarly, Eq. (4.20) can be expressed in terms of its plasma and external coil contributions as:

$$\Phi^{j}_{Total} = \oint \mathbf{A}^{j}_{plasma} \cdot d\mathbf{l}_j + \sum_i I_i \oint \mathbf{a}^{i}_{coils} \cdot d\mathbf{l}_j \tag{4.22}$$

where $\mathbf{A}^{j}_{plasma}$ is the vector potential at the location of the jth diagnostic due to the plasma current. The summation is over all of the external coils with current I_i, and $\mathbf{a}^{i}_{coils}$ is the vector potential at the location of the jth diagnostic due to a unit current within the ith coil. By comparing the second terms in Eqs. (4.21) and (4.22), the mutual inductance can be expressed in terms of the unit vector potential as:

$$M_{ij} = \oint \mathbf{a}^{i}_{coils} \cdot d\mathbf{l}_j \tag{4.23}$$

By reciprocity, the mutual inductance does not change when the indices are interchanged.[40] This can be represented as:

$$M_{ij} = \oint \mathbf{a}^{i}_{coils} \cdot d\mathbf{l}^{diag}_{j} = \oint \mathbf{a}^{j}_{diag} \cdot d\mathbf{l}^{coils}_{i} \tag{4.24}$$

where $\mathbf{a}^{j}_{diag}$ is the vector potential due to a unit current in the jth diagnostic coil, and the contour integral in the last term on the right is along the line which describes the ith external coil filament. This reciprocity shows that the flux which passes through an external coil due to a unit current in a diagnostic loop is equivalent to the flux that would pass through the diagnostic loop due to a unit current within the external coil. Using the Biot-Savart law, the vector potentials ($\mathbf{a}^{j}_{diag}$) can be calculated along the curves that define the external coil filaments.

The plasma contribution to the measured diagnostic flux in Eq. (4.22) is given in terms of the vector potential of the plasma current. This term depends on the magnitude and distribution of the plasma current, which depend directly on the particular equilibrium. However, using the same reciprocity argument and the Biot-Savart law, the plasma contribution to the flux in the jth diagnostic can be written as:

$$\Phi^{j}_{plasma} = \int_{plasma} dV' \mathbf{J}_{plasma}(\mathbf{x}') \cdot \mathbf{a}^{j}_{diag}(\mathbf{x}') \tag{4.25}$$

Here, $\mathbf{J}_{\text{plasma}}$ is the plasma current density, and the integral is over the plasma volume. Although the plasma current density changes with the equilibrium conditions, the diagnostic vector potential remains invariant.

The diagnostic vector potentials in the plasma region are calculated with V3RFUN at points on a fixed grid. In the model for CTH, this grid typically consists of 32 toroidal planes per field period, each with 101 by 101 points which span the area $0.45m \geq R \geq 1.05m$ by $-0.3m \geq z \geq 0.3m$. The diagnostic vector potential is also calculated along the filaments that define the external currents sources. The mutual inductance values are then calculated from Eq. (4.24). The contribution of each external current to the modeled flux is then calculated from the product of this mutual inductance and a specified coil current. The mutual inductance values for each external current and the diagnostic vector potentials within the plasma region are written to a database. This database of response functions is used in V3FIT to calculate the simulated diagnostic signals for each set of external currents and modeled plasma equilibrium. The response function calculations only need to be performed once for each set of magnetic diagnostics and external coils.

A problem arises when the simulated diagnostics are located within the last closed flux surface of the plasma. The Hall probe array is inserted into the plasma inside the last closed flux surface defined as s=1. Within this region, the VMEC calculations are performed on a discrete grid in flux coordinates. The numerical integration of Eq. (4.25) will be inaccurate if the modeled diagnostic is positioned on one of these discrete grid points. This error currently prevents magnetic diagnostics within the last closed flux surface from being used in equilibrium reconstruction with V3FIT. Although the Hall probe data cannot be used as a modeled diagnostic

signal in V3FIT, their magnetic field measurements are compared to those calculated from the reconstructed equilibria.

The accuracy of the pre-computed response functions and hence the V3FIT reconstruction results depend on simulated diagnostics that closely model their experimental counterpart. The geometric properties of the magnetic diagnostics are used in the V3RFUN calculations. For a simulated Rogowski coil, these properties are the cross sectional area, number of turns per unit length, and a set of points that define the path of the coil's axis. Careful measurements of the locations and orientations of each magnetic diagnostic such as those described in Sec. 3.4 are important to ensure the modeled diagnostics accurately represent the experiment. This agreement can be further optimized by comparing the mutual inductance values calculated using V3RFUN with those determined experimentally. This optimization method will be described in Sec. 5.4.

5 Experimental Considerations for Reconstruction

Equilibrium reconstructions are performed using V3FIT by comparing the simulated diagnostic response signals to those experimentally observed. As described in Sec. 4.3, the total magnetic flux measured by the magnetic diagnostic signals can be written in terms of a plasma contribution and that produced by external currents. The observed and modeled diagnostic signals are:

$$S^{O}_{Total} = S^{O}_{Plasma} + \sum_{i} M^{O}_{ij} I^{O}_{i} \qquad \text{and} \qquad S^{M}_{Total} = S^{M}_{Plasma} + \sum_{i} M^{M}_{ij} I^{M}_{i} \tag{5.1}$$

respectively. The external contribution to the diagnostic signal includes not only the flux from the external magnet coils, but also the flux produced by eddy currents in the vacuum vessel and supporting structures. This portion of the signal also includes any parasitic signals associated with finite loops at the feeds, or feed-throughs. The reconstruction process minimizes the difference in the modeled and experimental diagnostic signals which is:

$$S^{O}_{Total} - S^{M}_{Total} = \left(S^{O}_{Plasma} - S^{M}_{Plasma}\right) + \left(\sum_{i} M^{O}_{ij} I^{O}_{i} - \sum_{i} M^{M}_{ij} I^{M}_{i}\right) \tag{5.2}$$

The parameters reconstructed in this dissertation each change only the S^{M}_{Plasma} term. Differences that exist between the observed and modeled external signals still remain after reconstruction and result in systematic error. The steps taken to minimize the term $\left(\sum_{i} M^{O}_{ij} I^{O}_{i} - \sum_{i} M^{M}_{ij} I^{M}_{i}\right)$ and

thereby reduce the remaining systematic error are detailed in this chapter. This section will also describe the method of optimizing the model to more closely match the experimental setup.

5.1 Current Measurements

The currents (I_i^O) in the magnet coils as well as those induced in the vacuum vessel and coil frame eddy currents contribute the majority of the total magnetic diagnostic signal. Therefore, accurate measurements of these currents are an essential part of equilibrium reconstruction. With the exception of the OH coil and the induced currents in the vacuum vessel and helical coil frame, the currents in the external coils are measured using shunts. These current shunts are connected in series to the coil feeds and work by measuring the voltage drop across a precision resistor. The measured voltages from these shunts are digitized, recorded, and then converted to a current measurement using a calibration constant. The currents measured using these shunts have a specified accuracy of 0.5%.

Small DC offsets are present in the measured current data which must be corrected. The data acquisition boards are triggered to begin taking data on the order of 0.4 s prior to when the magnet coils are triggered. This brief period of time between these two triggers is used to determine the magnitude of these DC offsets. A linear fit is applied to this data during this brief time which is then subtracted from the signal.

Due to the magnitude of the current, a shunt is not used to measure. The OH coil current is measured using a Rogowski coil which surrounds the coil feed far from the other coils. During an OH discharge, in addition to the current driven within the plasma there are also significant currents induced in the vacuum vessel and coil frame segments. These induced currents produce a significant signal in the segmented Rogowski coils due to their close proximity. This makes it necessary to also measure these induced currents and include them in the reconstruction. There

are multiple full Rogowski coils utilized on CTH to measure each of these currents. The net toroidal plasma current is measured using coil 1PI264 which is internal to the vacuum vessel. Coil 1PO198 encloses the vacuum vessel as well as the plasma and measures the combined net toroidal current. The plasma current, as determined by 1PI264, is subtracted from the total current measured by 1PO198 in order to acquire the toroidal vacuum vessel current. An example of these current measurements is shown in Figure 5.1. The difference between these two signals is the vacuum vessel current.

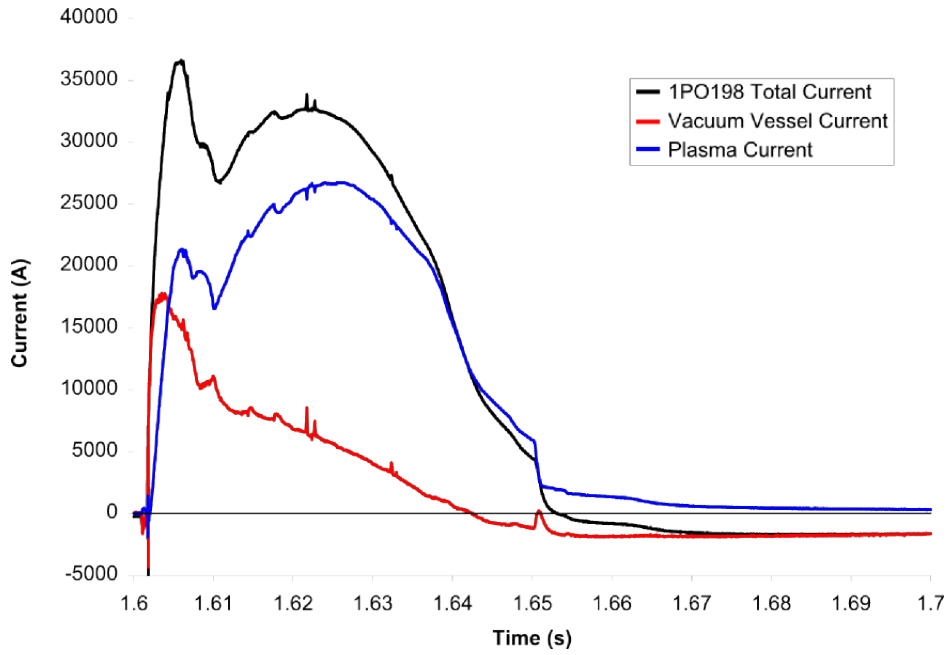

Figure 5.1 – Full current measured by 1PO198 (black), plasma current as measured by 1PI264 (blue), and the difference (red) is the vacuum vessel current.

Although the helical coil frame is not electrically continuous in the toroidal or poloidal directions, it was discovered that there are significant eddy currents driven within the various sections. The induced eddy currents were found to have relatively long decay times which made it necessary to measure and account for these currents. Although there are 10 coil frame segments, testing demonstrated less than 5% difference in the measured current from one coil

frame segment to the next. Because the current in each of the coil frame segments is so similar, only two Rogowski coils are used to measure the currents. These two Rogowski coils are mounted onto adjacent upper and lower coil frame sections. The average of these two current measurements is used to represent the currents in all 10 coil frame segments.

5.2 Modeled Currents

The previous section described the measurements of the magnitude of the external currents. The topology of the magnetic fields produced by these currents is not only dependent on the magnitude of these currents, but is also largely dependent on the distribution of these currents. Within the VMEC model, external current sources (I_i^M) are modeled as sets of filamentary conductors. The model used to define the magnet coils was defined based on CMM measurements and an SVD optimization routine, which utilized data acquired through electron beam field mapping[41]. The optimized coil model included features of the coils which produced

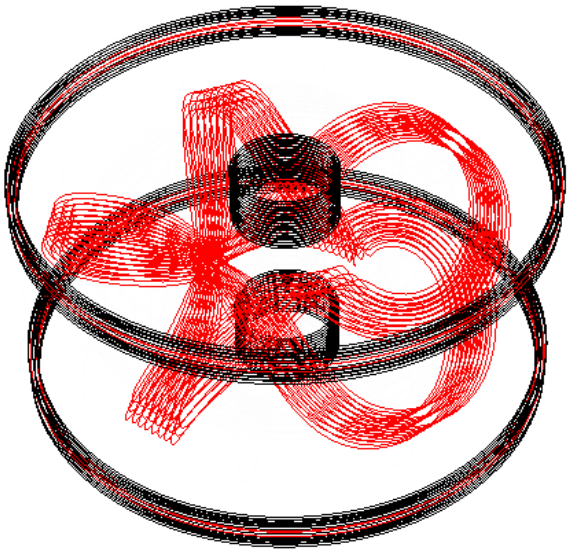

Figure 5.2 – Filament model of the HF (red) and TVF (black) external magnetic coils

fields that were moderately stellarator asymmetric. Since the present version of V3FIT performs reconstructions of stellarator symmetric plasmas only, the optimized coil frame model was symmetrized by eliminating the purely non-symmetric terms describing the HF coil, and averaging out small differences in spatial parameters (such as radius or height) which would result in vertical asymmetries. The symmetrized filament model is shown in Figure 5.2 for the HF (red) and TVF (black) coils.

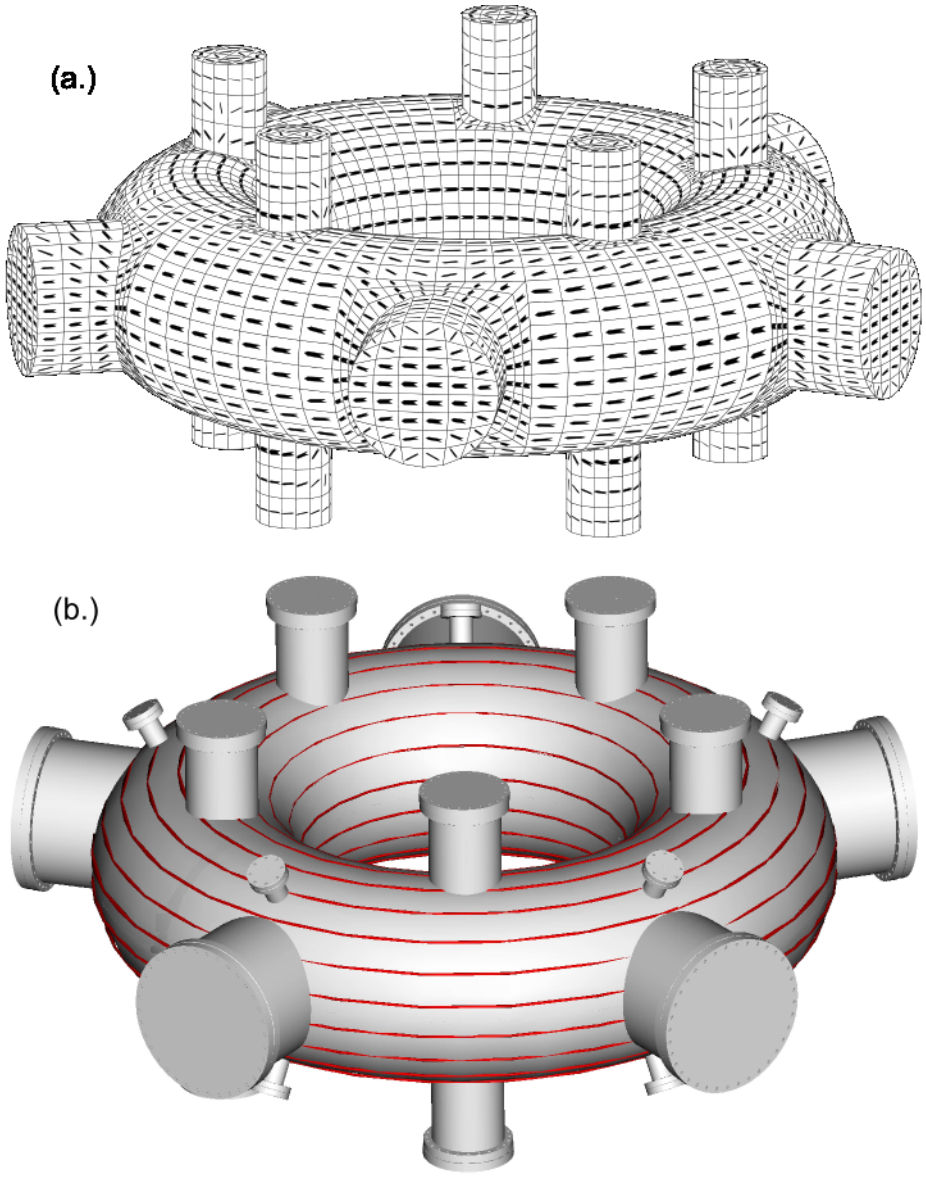

Figure 5.3 – VALEN models of simulated vacuum vessel current distribution using (a) a mesh model and (b) one with simple toroidal filaments

The current in the magnet coils can be accurately modeled due to the ability to directly measure the coil shapes and positions. However, eddy currents induced in the vacuum vessel and coil frame are more difficult to model accurately. The distribution of these induced currents depends on the source of magnetic flux which drives them. Also, the magnitudes of these eddy currents can decay at different rates from run to run. Although each of the magnet coils can drive eddy currents in the vacuum vessel and coil frame, the OH coil is the only external coil current that varies significantly during the time when the plasma is generated. The currents driven in the vacuum vessel during an OH discharge were modeled using the VALEN code[42]. Initially, a grid model was used to estimate the vacuum vessel current distribution as shown in Figure 5.3(a). This grid model simulates the currents driven within the toroidal shell, and around and within the various ports. The simulations show that for a typical OH current discharge, the variations in the induced current distribution occur primarily during the first 6 ms. After this initial 6 ms, the current distribution becomes more constant in the form displayed in Figure 5.3(a).

The results of the VALEN code served as a basis for a filamentary model of the vacuum vessel currents. The simulated current filaments are shown in Figure 5.3(b). This model consists of 24 toroidal filaments which lie within the vacuum vessel, and are poloidally separated by 15˚. The vacuum vessel wall thickness is a function of poloidal angle and varies as much as 1.2 mm. This thickness variation was included within the filamentary VALEN simulation. The radial distribution of current that is used based on these simulations is shown in Figure 5.4.

During the process of optimizing the magnetic diagnostic signals, long lived eddy currents within the helical coil frame were discovered which contributed a measurable portion of the diagnostic signal. The coil frame has a rather complicated shape which makes it difficult to

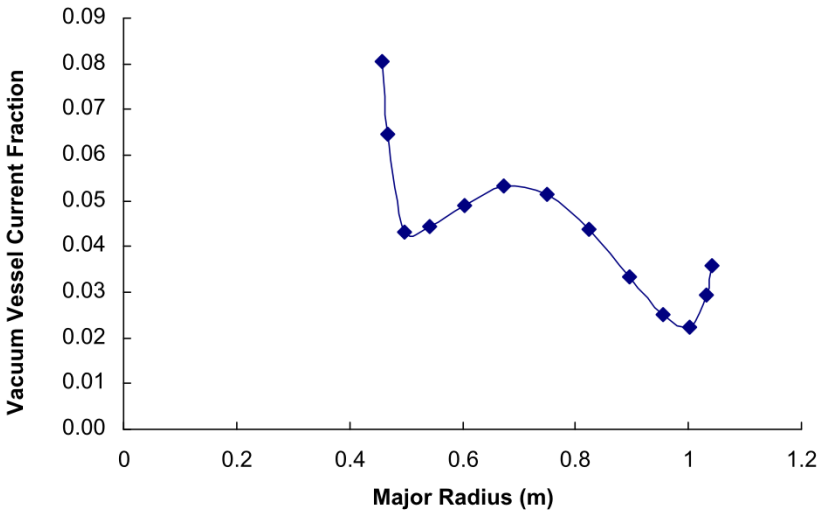

Figure 5.4 – Fraction of total vacuum vessel current in each filament versus major radius

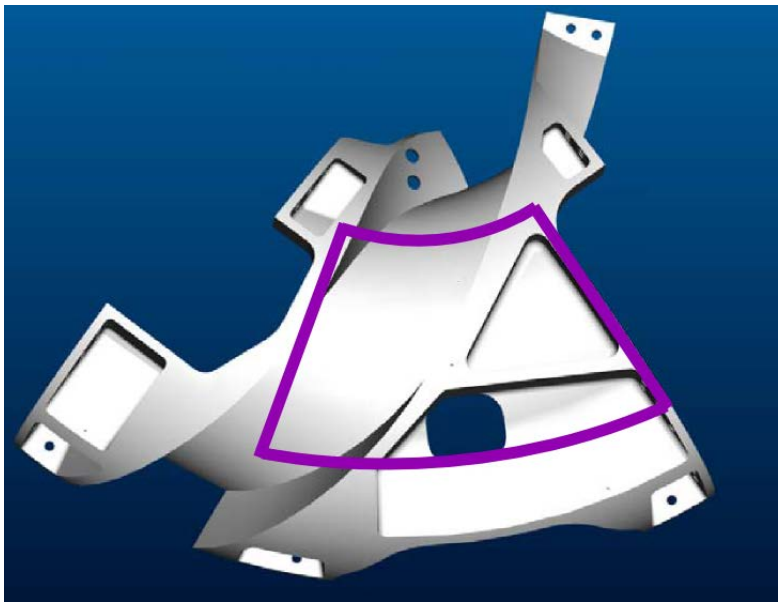

Figure 5.5 – Helical coil frame segment with modeled saddle coil current filament (purple)

predict and model the distribution of these eddy currents. As an initial approximation, these eddy currents were modeled using ten saddle-shaped coils. One of the simulated coils is shown in Figure 5.5 overlaid onto the coil frame segment. The currents are set to be the same in each of the ten coils, which maintains stellarator symmetry and is consistent with experimental results.

5.3 Determination of Mutual Inductance

As shown in Eq. (5.1), the measured magnetic flux contributed by the external current sources is a function of the current magnitude as well as the mutual inductance. For the reconstructions performed in this dissertation, the observed external currents were used as the modeled currents so that $I_i^O = I_i^M$. For this condition, the externally contributed portion of Eq. (5.2) becomes $\sum_i \left(M_{ij}^O - M_{ij}^M\right) I_i^O$. To minimize this term, it is necessary to accurately measure the diagnostic mutual inductance values to each external coil and then optimize the model diagnostics to match.

The mutual inductance values of the Rogowski coils to each external current depend on the orientation and geometry of the diagnostic coils as well as the distribution of the external currents. This quantity should remain fixed since the diagnostic positions and current distributions are constant. A process is described in Sec. 5.4 in which the positions and orientations of the modeled magnetic diagnostics are optimized through comparisons of the modeled and empirical mutual inductance values. This comparison can also highlight errors in the model of the external current distributions. The mutual inductance values of the Rogowski coils to each external current, are also used to isolate the portion of the total signal which is contributed by the plasma (Sec. 5.6).

The mutual inductances (M_{ij}^O) of the external magnet coils to each magnetic diagnostic were measured using the following method. The flux from each external coil set was isolated by open-circuiting all of the other coil sets to ensure that there were no induced currents driven in them. Then, a relatively constant current was driven in the remaining coil to minimize the effect

of induced currents in the vacuum vessel and helical coil frame which occur during the current ramp. During this time interval in which the coil current was constant, the ratio of the measured flux in the Rogowski coil to the current measured in the isolated coil was used to determine the experimental value of the mutual inductance. The mutual inductance thus obtained is an average over approximately 0.2 s. The variation in the measured mutual inductance during this 0.2 s period was defined as the measurement uncertainty. As an example, the flux measured by one segment of 8PI264 when excited by the HF coil current is shown in Figure 5.6. Also

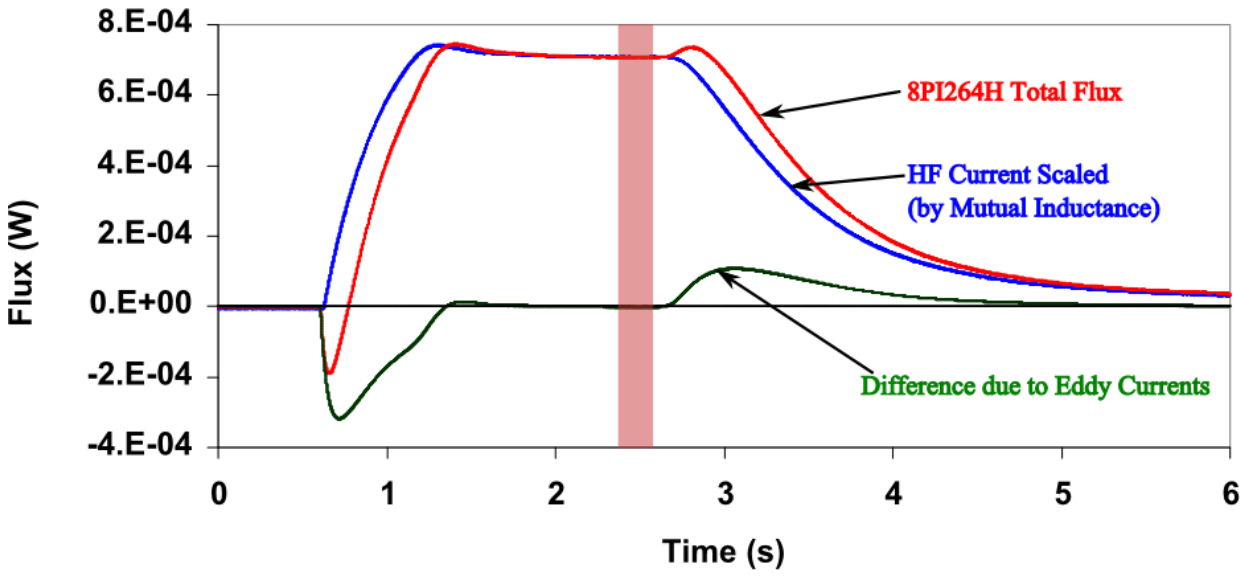

Figure 5.6 – Experimental flux measured in 8PI264 (red) with HF current only. Computed flux due to HF current (blue) and difference between measured and computed flux (black).

shown in the figure is the calculated flux contribution from the HF coil. The shaded region in the plot represents the time interval during which the mutual inductance was determined. The flux measured during the time when the HF coil current is ramping up or down consists not only of the HF contributed flux but also a significant contribution from induced eddy currents elsewhere on the CTH structure. The mutual inductance of the magnetic diagnostics to the eddy currents induced in the vacuum vessel and helical coil frame can not be determined in the same fashion.

The vacuum vessel and helical coil frame have complex shapes, and the current density distribution can vary significantly depending on the current source which induces the current. The currents that exist within these structures during a current driven plasma discharge are primarily induced from the OH coil. Due to the fact that there is no simple method of driving a constant current with the same distribution, a different method was chosen to determine the mutual inductance of these currents to the diagnostic coils.

The method used to determine these mutual inductance values can be described by starting once again with Eq. (4.21) which gives the total flux measured by each diagnostic. During a run in which a plasma was not generated $\left(\Phi^{j}_{plasma}=0\right)$, this total flux is:

$$\Phi^{j}_{Total}(t)=\sum_{i} M_{ij} I_i(t) \tag{5.3}$$

Assuming all currents (I_i) are measured, the mutual inductance matrix (M_{ij}) can be determined using a standard least squares technique. This is accomplished by first defining the following merit function:

$$\chi^2_{Ind}=\sum_{k=1}^{N}\left(\frac{\Phi^{j}_{Total}(t_k)-\sum_{i} M_{ij} I_i(t_k)}{\sigma(t_k)}\right)^2 \tag{5.4}$$

where σ represents the measurement uncertainty. Also, the time is now represented as a discrete variable, t_k, corresponding to the digitized signal data acquired. The value of χ^2_{Ind} is minimized by taking the derivative of Eq. (5.4) with respect to M_{ij} and setting the result to zero. The end result gives the mutual inductance as:

$$M_{ij}=\alpha^{-1}_{il}\beta_l \tag{5.5}$$

where

$$\alpha_{il} = \sum_{k=1}^{N} \frac{I_i(t_k) I_l(t_k)}{\sigma^2(t_k)} \qquad \text{and} \qquad \beta_l = \sum_{k=1}^{N} \frac{\Phi_{Total\ j}(t_k) I_l(t_k)}{\sigma^2(t_k)} \tag{5.6}$$

This method was only used to determine the mutual inductance to the currents induced in the vacuum vessel and the helical coil frame. The other terms in the mutual inductance matrix were defined based on the isolated coil technique described earlier.

5.4 Optimization of Modeled Diagnostics

One of the challenges of equilibrium reconstruction is to ensure that the position and orientation of the modeled diagnostics closely resemble the experimental diagnostics. As described in Sec. 3.4, the segmented Rogowski coils do not have a constant minor radius or toroidal position. Also, the poloidal position of each Rogowski coil segment is often difficult to measure. Moreover, the method used to calibrate full Rogowski coils cannot be used to determine the sensitivity of the segmented Rogowski coils. The process used to optimize the model diagnostics and thereby minimize the difference between observed and modeled mutual inductance values $\left(M_{ij}^{O} - M_{ij}^{M}\right)$ is described in the following section.

The external coil sets used for model optimization were the HF and TVF, because they have the highest mutual inductance values hence produce a greater diagnostic signal. The following parameter is minimized for each 8-part Rogowski coil set:

$$\chi^2_{Model} = \sum_{i=1}^{2} \sum_{j=1}^{8} \left[\frac{\left(M_{ij}^{o} - \lambda_s M_{ij}^{m}\right)}{\sigma_o} \right]^2 \tag{5.7}$$

where M_{ij}^{O} and M_{ij}^{M} represent the observed and modeled mutual inductances respectively. The uncertainty in the observed mutual inductance measurement is shown as σ_o. The summations are over the eight Rogowski coils in a set, and the two external coils with the largest mutual

inductance (HF and TVF). The variable λ_s is a scaling factor which was determined by minimizing Eq. (5.7) with respect to λ_s. This scaling factor is defined by:

$$\lambda_s = \frac{\sum_{i=1}^{2}\sum_{j=1}^{8}\left[\frac{\left(M_{ij}^{o}\, M_{ij}^{m}\right)}{\sigma_o^2}\right]}{\sum_{i=1}^{2}\sum_{j=1}^{8}\left[\frac{M_{ij}^{m}}{\sigma_o}\right]^2} \tag{5.8}$$

The calibration constant of the segmented Rogowski coils is simultaneously optimized by including the parameter λ_s . Physically, this constant depends on the cross sectional area of the Rogowski coil as well as the number of turns per unit length.

The measurement and fitting process described in Sec. 3.4 gives the overall contour of each internal 8-part Rogowski coil, but does not provide the beginning and ending positions of each coil within the contour. The modeled diagnostics were initially optimized by poloidally rotating the modeled 8-part Rogowski set along the measured contour. The quantity defined in Eq. (5.7) was calculated for each poloidal offset. As an example of this technique, the values calculated for the 8-part set, 8PI108, are shown in Figure 5.7 versus the poloidal angle of 8PI108A. This poloidal angle was optimized by iteratively applying a quadratic fit to the values near each local minimum.

Once the overall poloidal angle of the modeled 8-part Rogowski coils had been optimized, the individual diagnostics within each set were then modified in order to further reduce the χ^2_{Model} value. Individual modifications included varying the poloidal extent, average poloidal angle, and number of turns per unit length. The variation in poloidal position and length were small compared to the uncertainties associated with constructing the coils. Modification of the number of turns per unit length was utilized as a simple scaling adjustment to account for differences in the gain between various diagnostics. Figure 5.7(b) displays a closer view of the

minimized data presented in Figure 5.7(a), but also displays the additional reduction achieved by independently modifying each Rogowski coil segment. This optimization process fixed the modeled poloidal position of the Rogowski coil segments inside the stainless steel tubes. The schematic shown in Figure 5.8 displays the final modeled positions of each internal Rogowski coil segment.

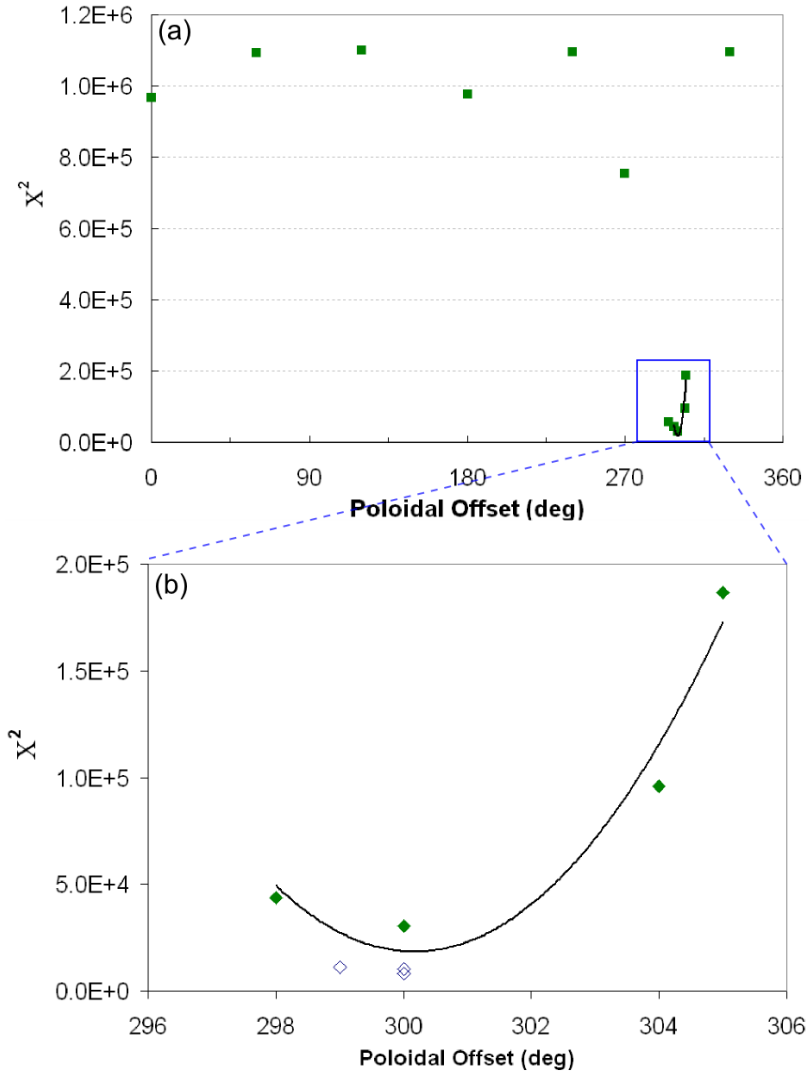

Figure 5.7 – (a) Minimization parameter χ^2_{Model} versus the poloidal orientation of 8PI108; Minimum determined using a quadratic fit (b) Modification of the individual Rogowski segments further reduces χ^2_{Model} (open diamonds)

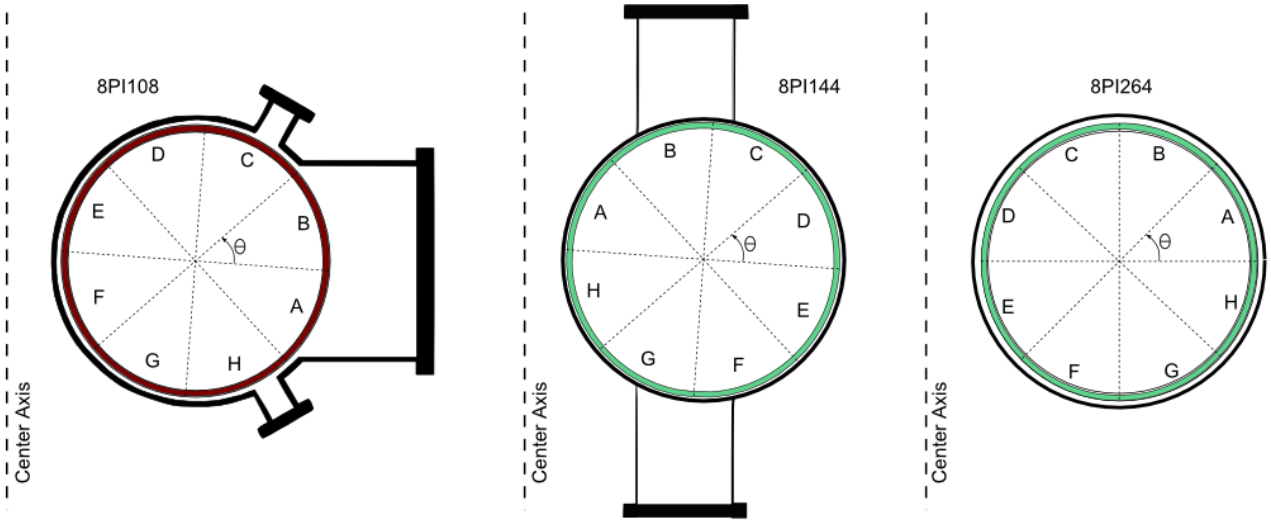

Figure 5.8 – Schematic showing modeled orientation of the three segmented Rogowski coil sets

Following this optimization routine, the modeled mutual inductances show good agreement to the experimental values, as summarized in Table 5.1. This table shows the experimentally determined mutual inductance of each 8-part Rogowski coil segment to both the HF and TVF external coils. The percent differences between the modeled and experimental values are also shown. The model closely matches the experimental mutual inductance values for the majority of the Rogowski coils. Diagnostics 8PI108E and 8PI264C both show a relatively high difference in the modeled mutual inductance to the HF coil. However, in both cases, the magnitude of the experimental mutual inductance to the HF coil is many times smaller than the corresponding mutual inductance to the TVF coil. For these lower mutual inductance values, sources of pickup contribute a larger fraction of the measured signal. These sources of pickup are not accounted for in the model. Although the optimization process described in this section has greatly improved the agreement between the experimental and modeled diagnostics, the remaining differences can still introduce systematic error into the reconstruction routine. The method used to minimize these remaining errors will be shown in Sec. 5.6.

Rogowski Coil	Mutual Inductance to HF		Mutual Inductance to TVF	
	Experimental (H)	Model Difference (%)	Experimental (H)	Model Difference (%)
8PI108A	1.65E-06	2.4	6.76E-06	0.4
8PI108B	1.88E-06	-2.3	6.76E-06	-1.6
8PI108C	1.28E-06	3.0	5.62E-06	1.0
8PI108D	-2.58E-06	-2.6	-3.99E-07	-7.9
8PI108E	-9.98E-07	-13.8	-6.96E-06	0.2
8PI108F	3.36E-06	1.8	-7.57E-06	1.1
8PI108G	-2.69E-06	3.2	-5.49E-06	0.5
8PI108H	-1.33E-06	8.7	1.56E-06	-0.4
8PI144A	1.37E-06	-3.8	-4.09E-06	1.2
8PI144B	1.95E-06	-0.6	-1.12E-06	1.7
8PI144C	-4.24E-07	-5.6	3.07E-06	2.8
8PI144D	-3.78E-06	-0.2	3.94E-06	-0.4
8PI144E	-2.68E-06	-1.5	3.91E-06	0.9
8PI144F	7.64E-07	-0.7	1.24E-06	0.8
8PI144G	2.12E-06	-0.4	-2.63E-06	0.6
8PI144H	4.73E-07	1.1	-4.23E-06	0.9
8PI264A	1.01E-06	6.3	4.06E-06	-0.9
8PI264B	1.46E-06	-6.4	2.38E-06	3.1
8PI264C	-5.71E-08	77.9	-2.04E-06	-0.1
8PI264D	-5.88E-07	-7.4	-4.25E-06	2.7
8PI264E	2.33E-06	0.3	-4.35E-06	-0.5
8PI264F	-1.29E-06	-1.7	-2.43E-06	-1.1
8PI264G	-2.84E-06	0.4	2.36E-06	1.2
8PI264H	2.09E-07	1.3	4.26E-06	0.0

Table 5.1 – Mutual Inductance of 8-part Rogowski coils to HF and TVF magnet coils and the percent difference in the modeled value

5.5 Full Rogowski Coil Compensation

Similar to the shunt measured currents, the Rogowski coil signals which measure the plasma and eddy currents also require significant corrections. As described in Secs. 3.1 and 3.2, an ideal Rogowski coil should only respond to the currents that are enclosed within the loop. However, physical Rogowski coils have various sources of pickup from external current sources. Using the method described in Sec. 5.3, the mutual inductance of each full Rogowski coil to each of the external currents was determined. The following corrections were made to the full Rogowski signals:

$$S_{Raw}(t) - \sum_i M_i I_i(t) - \left[S_{offset} + R_{drift} t\right] = S_{Corrected}(t) \tag{5.9}$$

where S_{Raw} is the full uncorrected signal, M_i are the empirically determined mutual inductance values, I_i are the external currents, and $S_{Corrected}$ is the corrected signal. This correction is applied to each full Rogowski diagnostic, although the double wound coils have significantly less pickup than the single wound coils.

The bracketed quantity in Eq. (5.9) is the correction for linear drift. As described in Sec. 3.2, the full and segmented Rogowski coils are each connected to an integrating circuit. Although the circuit design helps reduce saturation, the integrator circuit introduces a drift and offset to the diagnostic signals. In order to remove this drift and offset, a linear fit is applied to the integrated signal 0.4 s prior to when the magnet coils are triggered. This initial data provides the slope (R_{drift}) and intercept (S_{offset}) which are then subtracted from the diagnostic signal over the full time of the run.

5.6 Modification of Segmented Rogowski Coil Signals

The measurement and modeling of the external currents, as well as the method used to optimize the modeled diagnostics are described in the previous sections of this chapter. These methods reduce the differences between the modeled and observed external flux represented in Eq. 5.2 as $\left(\sum_i M_{ij}^O I_i^O - \sum_i M_{ij}^M I_i^M \right)$. However, as shown in Table 5.1, small differences in the mutual inductance still remain. Due to the magnitude of the external magnet currents, these small differences in the modeled mutual inductance can still result in a significant systematic error. To minimize the known sources of systematic error, the observed signals are adjusted prior to being used for equilibrium reconstruction.

The initial correction is to subtract out drift and offsets added to the signal by the integrating circuit. This first correction to the raw signals (S^O_{Raw}) gives the signal produced by the total flux (S^O_{Total}) and is given by:

$$S^O_{Total} = S^O_{Raw} - \left\lfloor S^O_{Offset} + R_{Drift} t \right\rfloor \tag{5.10}$$

where the correction shown in brackets is determined in the same way as described in the previous section. The total flux measured by the segmented Rogowski coils is a combination of flux generated by the external coils and that generated by the plasma. This can be represented as:

$$S^O_{Total} = S^O_{Plasma} + \sum_j M^O_j I_j \tag{5.11}$$

where S^O_{Plasma} is the portion of the signal generated by the plasma current. The M^O_j terms are the empirically determined mutual inductances, and the summation is over each of the external currents (I_j). Solving for the plasma contributed portion of the total signal gives the following:

$$S^O_{Plasma} = S^O_{Total} - \sum_j M^O_j I_j \tag{5.12}$$

Due to small errors in the measured mutual inductance as well as sources of pickup, a residual signal is still present prior to the time when the plasma is generated. To correct for this offset, the average residual signal is subtracted as measured 1 ms prior to when the OH is discharged. If this time is represented as t_α, the adjusted plasma signal in Eq. (5.12) is now:

$$S^O_{Plasma}(t) = S^O_{Total}(t) - \sum_j M^O_j I_j(t) - S^O_{Residual}(t_\alpha) \tag{5.13}$$

where

$$S^O_{Residual}(t_\alpha) = S^O_{Total}(t_\alpha) - \sum_j M^O_j I_j(t_\alpha) \tag{5.14}$$

The assumption being made is that there is no net toroidal plasma current at the time t_α. An example of how the observed plasma signal compares with the total signal from one of the 8-part Rogowski coils is shown in Figure 5.9. In this figure, the plasma is started at about 1.6 s and remains for approximately 100 ms. The remaining non-zero plasma signal (shown in red) at 0.8 s is characteristic of the typical residual signal that remains after correction.

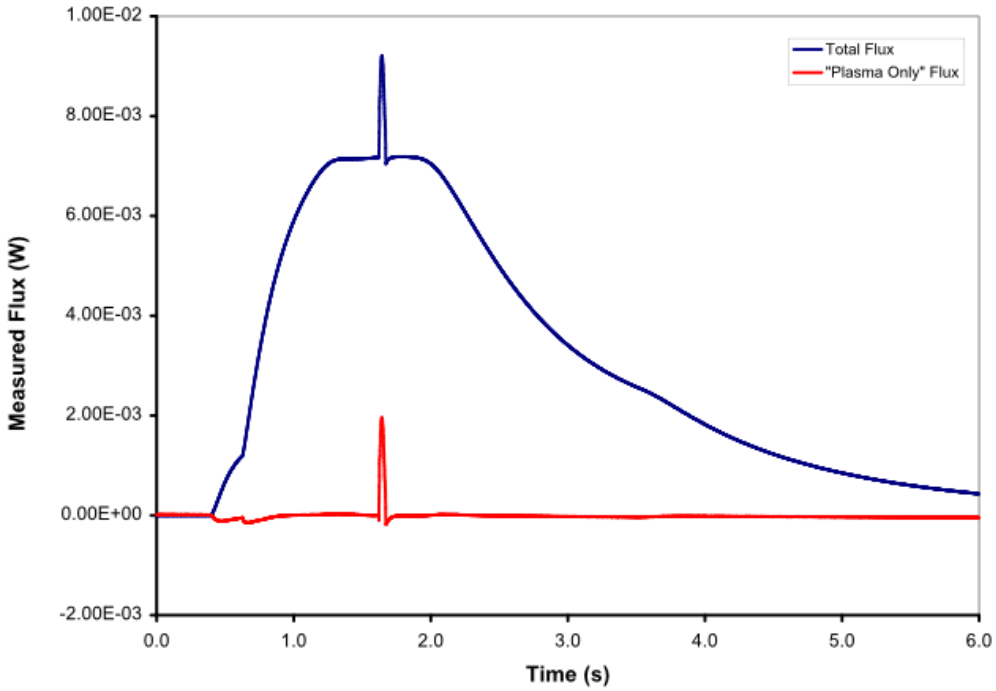

Figure 5.9 – Example showing how the plasma flux contribution (red) can be extracted from the total Rogowski coil flux measured (blue).

Within V3FIT, the modeled diagnostic Rogowski signals include contributions from the plasma and the external currents. Similar to Eq. (5.12), the modeled signals can be represented as:

$$S^M_{Total} = S^M_{Plasma} + \sum_j M^M_j I_j \qquad (5.15)$$

where S^{M}_{Plasma} is the plasma contribution calculated from the modeled VMEC equilibrium, M^{M}_{j} are the mutual inductance values as determined from the V3RFUN code, and I_j are the measured external currents. Ideally, the modeled mutual inductances, M^{M}_{j}, would be identical to the observed mutual inductances, M^{O}_{j}, indicating that the modeled magnet coils and diagnostic coils exactly matched those of the experiment. However, differences inevitably exist, and can significantly influence the reconstruction results. To try and minimize this effect, the summation in Eq. (5.15) was added to Eq. (5.13) to give:

$$S^{O}_{Plasma}(t)+\sum_{j} M^{M}_{j} I_{j}(t)=S^{O}_{Total}(t)-\sum_{j}\left(M^{O}_{j}-M^{M}_{j}\right)I_{j}(t)-S^{O}_{Residual}(t_{\alpha}) \qquad (5.16)$$

or

$$S^{O}(t)\equiv S^{O}_{Total}(t)-\sum_{j}\delta M_{j} I_{j}(t)-S^{O}_{Residual}(t_{\alpha}) \qquad (5.17)$$

In this equation, S^O is the observed diagnostic signal used in V3FIT, and is comprised of the total observed flux with two presumably small corrections.

The majority of magnetic flux contributed by external currents can be removed as demonstrated in Figure 5.9. However, the signal S^{0}_{Plasma} as defined by in Eq. (5.13) assumes the remaining magnetic flux is generated strictly from the plasma. For a shot in which no plasma was generated, the diagnostic signals would be entirely due to flux generated by external currents. If the measured currents and empirically determined mutual inductance values are correct, the value of S^{0}_{Plasma} for this shot should be zero. An example of the measured value of S^{0}_{Plasma} for a shot in which no plasma was generated is shown in Figure 5.10. Although the magnitude of the flux shown in this plot is significantly smaller than the flux measured from the plasma (shown in red in Figure 5.9), it is not zero or simply random noise. The remaining

uncompensated magnetic flux follows the loop voltage trace. This remaining flux is likely due to a small error in the mutual inductance value to the induced eddy currents. The magnitude of the uncompensated flux shown for this diagnostic is typical of what is measured for the other segmented Rogowski coils. Based on these measurements, a constant flux value of $1x10^{-4}$ W was set as the diagnostic signal uncertainty for each of the Rogowski coils used in reconstructions.

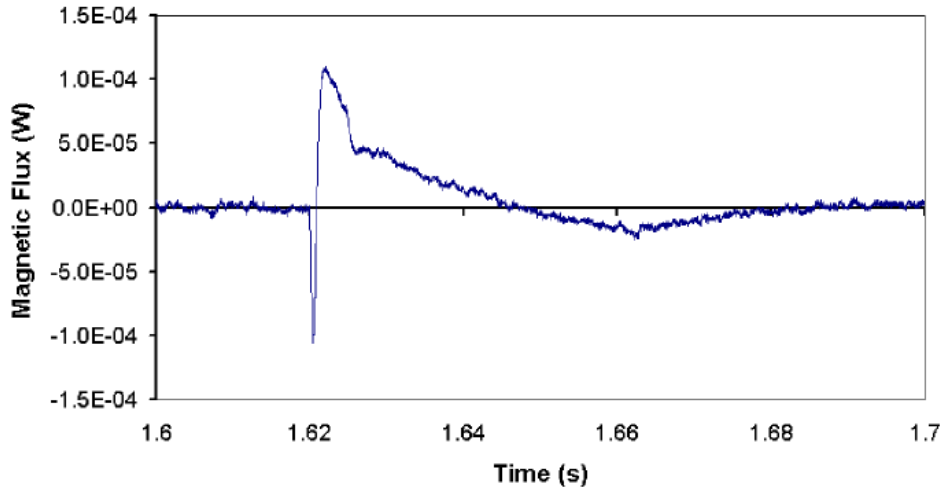

Figure 5.10 – Uncompensated magnetic flux as measured by 8PI264B during a shot in which no plasma was generated

5.7 Hall Sensor Signal Considerations

As described in Sec. 3.3, the Hall sensor array was designed to measure the poloidal component of the magnetic field along the mid-plane of CTH. As with the segmented Rogowski coils, the majority of the magnetic field measured by the Hall sensors is produced by the external magnetic coils. By design, the normal to the sensor surface should be oriented in the upward or $+\hat{z}$ direction. Aligned in this way, the sensors should not detect the toroidal magnetic field. In reality, each of the individual sensors can have small alignment errors as well as manufacturing

defects which can cause them to detect non-poloidal fields. It is important to characterize these effects prior to comparing these measurements with reconstructed equilibria.

To measure the Hall sensor response to the external current sources, the same technique that was used to determine the Rogowski coil mutual inductance values was applied (Sec. 5.3). That is each coil set was isolated by open circuiting all the others. Then a constant current was driven in this isolated coil. The ratio of the magnetic field measured by each Hall sensor to the measured coil current gave the Hall sensor response function. This response function is

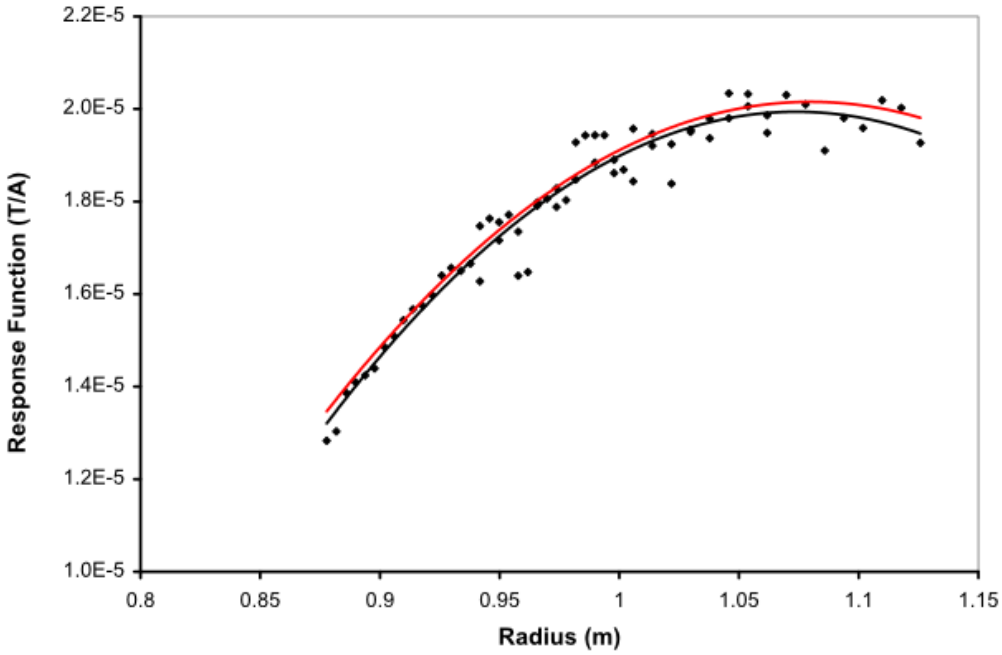

Figure 5.11 – Hall sensor response to HF current versus radial position. Black curve is a fit to data, and red curve is modeled using V3RFUN

analogous to the mutual inductance values (M_{ij} in Eq. (4.21)) determined for the Rogowski coils. However, unlike the Rogowski coils, the positions of the Hall sensors do not remain constant.

The radial dependence of these response functions was determined by performing a series of constant current shots with the Hall probe array at different radial positions. As an example,

Figure 5.11 shows how the response function to the HF coil set depends on the radial position of the probe. The data points in this plot were generated by positioning the array at four different radial positions and determining the response of all 16 sensors. The HF response function data was fit using a quadratic as shown by the black curve. Although the quadratic is generally a good fit, the Hall probe data does exhibit some scatter. Upon further investigation of this scatter, the variations from the fit depended more on the specific probe than on the radial position. Since the HF coil produces a strong toroidal magnetic field in addition to the poloidal field, the scatter is likely due to variations in the toroidal field pickup. The average response of each of the 16 Hall

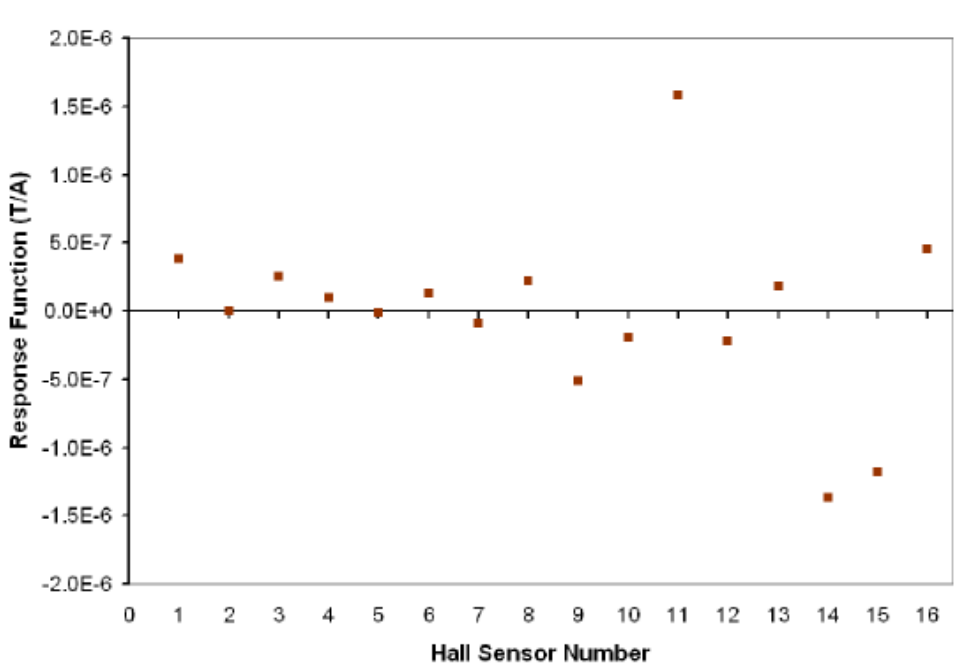

Figure 5.12 – Average Hall sensor response to TF current versus sensor number

sensors to the predominantly toroidal field produced by the TF coil is shown in Figure 5.12. Ideally, the Hall sensors would not respond to a purely toroidal field, and in fact the majority of sensors show only a small response. However, four sensors show a response with a magnitude greater than 5×10^{-7} T/A . These four sensors do indeed correspond to the points in Figure 5.11

which show the largest deviation from the fitted curve. These sensors appear to be slightly misaligned which results in the detection of non-poloidal fields. However, by determining the various response functions of each sensor, the majority of the Hall sensor signal contributed from external current sources can be removed. The result is a measure of the poloidal magnetic field produced predominantly by currents within the plasma.

A similar approach can be applied to the modeled magnetic fields calculated during equilibrium reconstruction. Using the output from VMEC, the modeled poloidal magnetic field at the Hall sensor locations can be determined. The modeled magnetic field is produced predominantly from currents external to the plasma. Errors in the way these external currents are modeled can lead to systematic differences when compared to the Hall probe measurements. For each of the modeled external currents, V3RFUN was used to compute the poloidal magnetic field produced due to a unit current for a series of points along the outer mid-plane. These localized field values were fit using simple polynomials and compared with the Hall probe response function data. As an example, the red curve in Figure 5.11 shows the modeled radial distribution of the poloidal magnetic field along the outer mid-plane due to a unit current in the HF coil. The modeled curve shows generally good agreement to the Hall probe fit (black). By determining the external current contribution to the modeled poloidal field in this region, this portion can be removed from the total poloidal field. The remaining poloidal field is due to the modeled currents within the plasma.

In order to test how well this set of response functions accounts for the externally produced poloidal field, a series of shots were ran in which there was no plasma generated. As an example, during shot 11072022 the Hall probe array was positioned such that the inner-most sensor had a minor radius of 0.8778 m. This position was chosen to maximize the number of

sensors that were within the last closed flux surface. The external magnetic field configuration for this shot utilized the HF, TVF, and TF coils and had a vacuum transform with the range $0.059 \leq \iota(s) \leq 0.063$. Although there was no plasma current, the OH transformer was still discharged to generate similar eddy currents in the vacuum vessel and coil frame. Using the measured external currents along with a model of the edge limiters, V3FIT was used to calculate the vacuum magnetic equilibria. The total poloidal magnetic field as measured by the Hall sensors are compared to those calculated from the reconstructed equilibria in Figure 5.13. There is a small offset seen between the modeled and measured poloidal field strengths. The values with the largest offsets are due to the slight misalignments of the sensors as described at the beginning of this section. By using the modeled and empirically determined set of response functions, the magnetic field contributed from the external coils at each Hall sensor location was subtracted leaving the residual signals shown in Figure 5.14. These residual signals are small which is as expected since there is no plasma current present during this shot. This demonstrates that the externally contributed poloidal field can be effectively removed from the Hall sensor measurements.

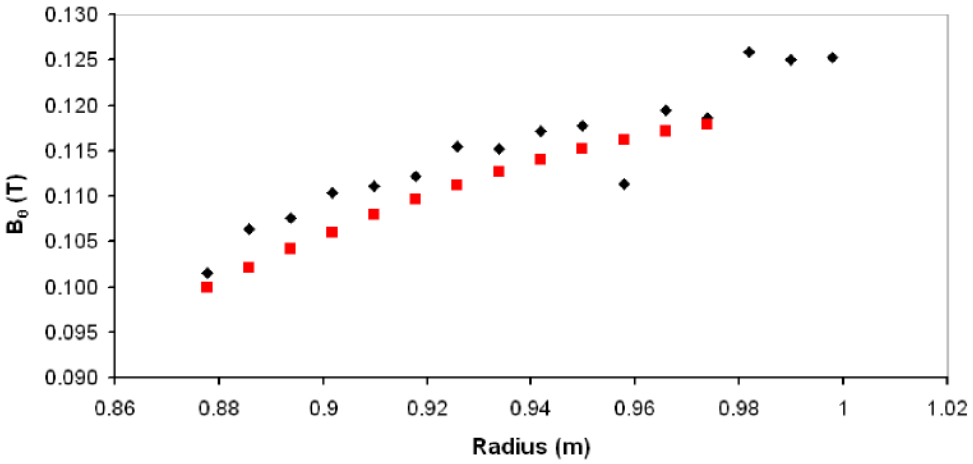

Figure 5.13 – Total poloidal magnetic field measured (black) using Hall probe and calculated (red) from equilibrium reconstruction for shot 11072022 at 1.64s

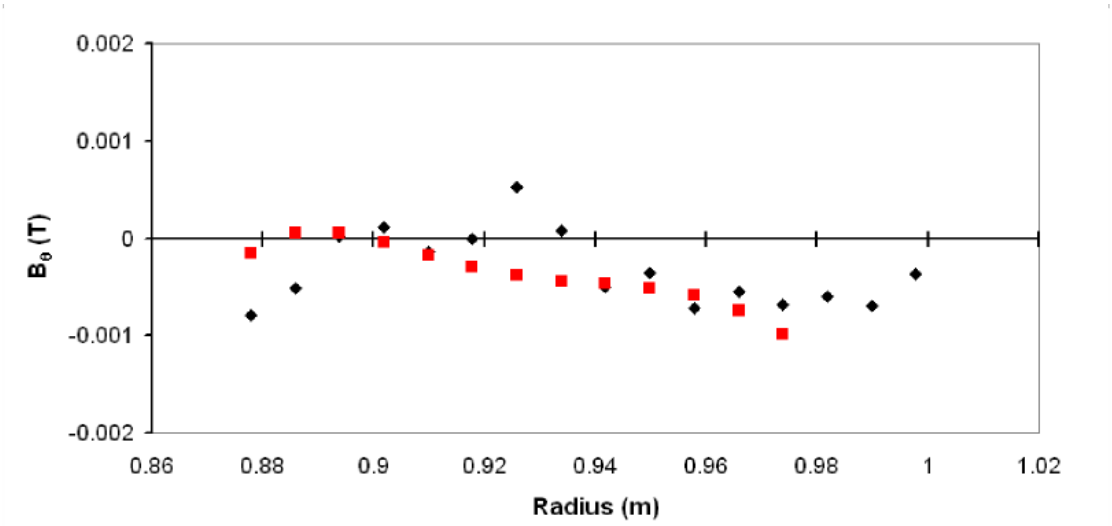

Figure 5.14 – Residual poloidal field from the Hall probe (black) and reconstructed equilibrium (red) after external fields have been removed for shot 11072022 at 1.64s

6 Reconstruction Results and Discussion

In the previous chapter, a series of techniques were described that are used to optimize the modeled diagnostics as well as compensate the magnetic measurements for flux from non-plasma sources. With this framework established, results obtained from equilibrium reconstruction are presented. Three 8-part Rogowski coils and 1 full Rogowski coil are used to measure poloidal field fluxes. This diagnostic data is used in combination with the V3FIT code to perform a series of equilibrium reconstructions. Reconstructions have been performed for different times during a plasma shot, and for different external magnetic field configurations. In Sec. 6.1, reconstruction results that make use of different current density parameterizations and model pressure profiles are shown. The time evolution of the reconstructed parameters are presented. In Sec. 6.2, these reconstructed parameters are compared to those from a similar shot in which a plasma disruption occurs. To investigate the effect of the external magnetic field configuration, the reconstructions of plasma equilibria with a low vacuum rotational transform are shown in Sec. 6.3. In Sec. 6.4, poloidal field measurements of Hall probe data are presented and compared to those predicted by reconstruction using the Rogowski coils. A summary of the remaining systematic error is given in Sec. 6.5 along with suggestions for improvement of the equilibrium reconstruction process.

6.1 Reconstruction of Plasmas with High Rotational Transform

The first example of equilibrium reconstruction considers a case for which the external coil currents were configured to produce a vacuum transform with a range of $0.10 \leq \iota(s) \leq 0.13$. The time evolution of the currents in the external magnet coils is shown in Figure 6.1. A plasma is generated using ECRH at 1.6 seconds once the HF and TVF currents have reached a relatively

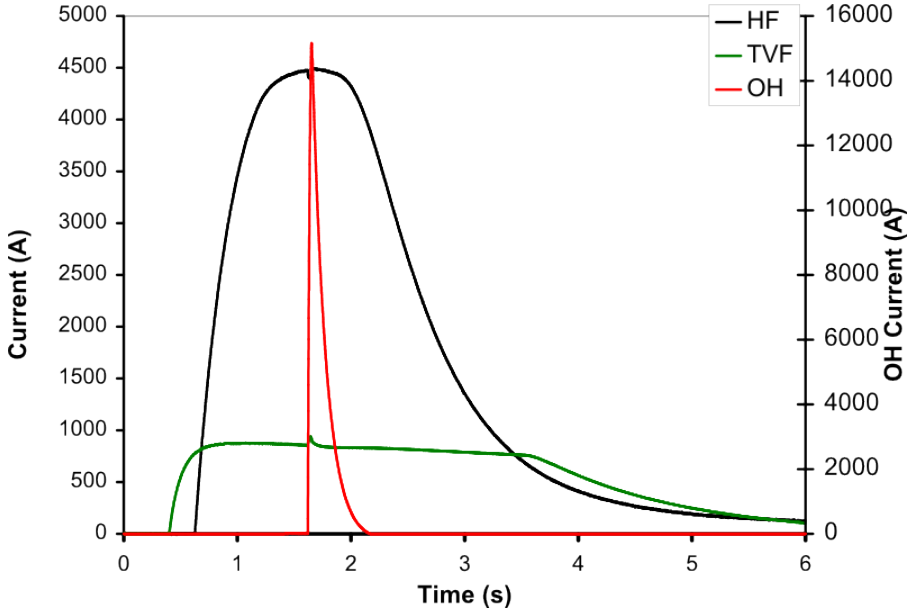

Figure 6.1 – Time evolution of HF (black), TVF (green), and OH (red) external coil currents for shot 11050236

constant value. The line averaged electron density versus time is shown in Figure 6.2 (a). The initial ECRH-generated plasma has an electron density of 2×10^{18} m^{-3}. During the 20 ms period of time prior to the OH discharge, there is no net toroidal current driven in the plasma. The OH capacitor bank is discharged at 1.62 s producing a toroidal loop voltage that drives a toroidal current within the plasma. The measured loop voltage and toroidal plasma current are shown in Figure 6.2(b). The induced current heats the plasma and also enables the average plasma density to rise about the cut-off density as shown in Figure 6.2 (a). The rapidly changing magnetic flux

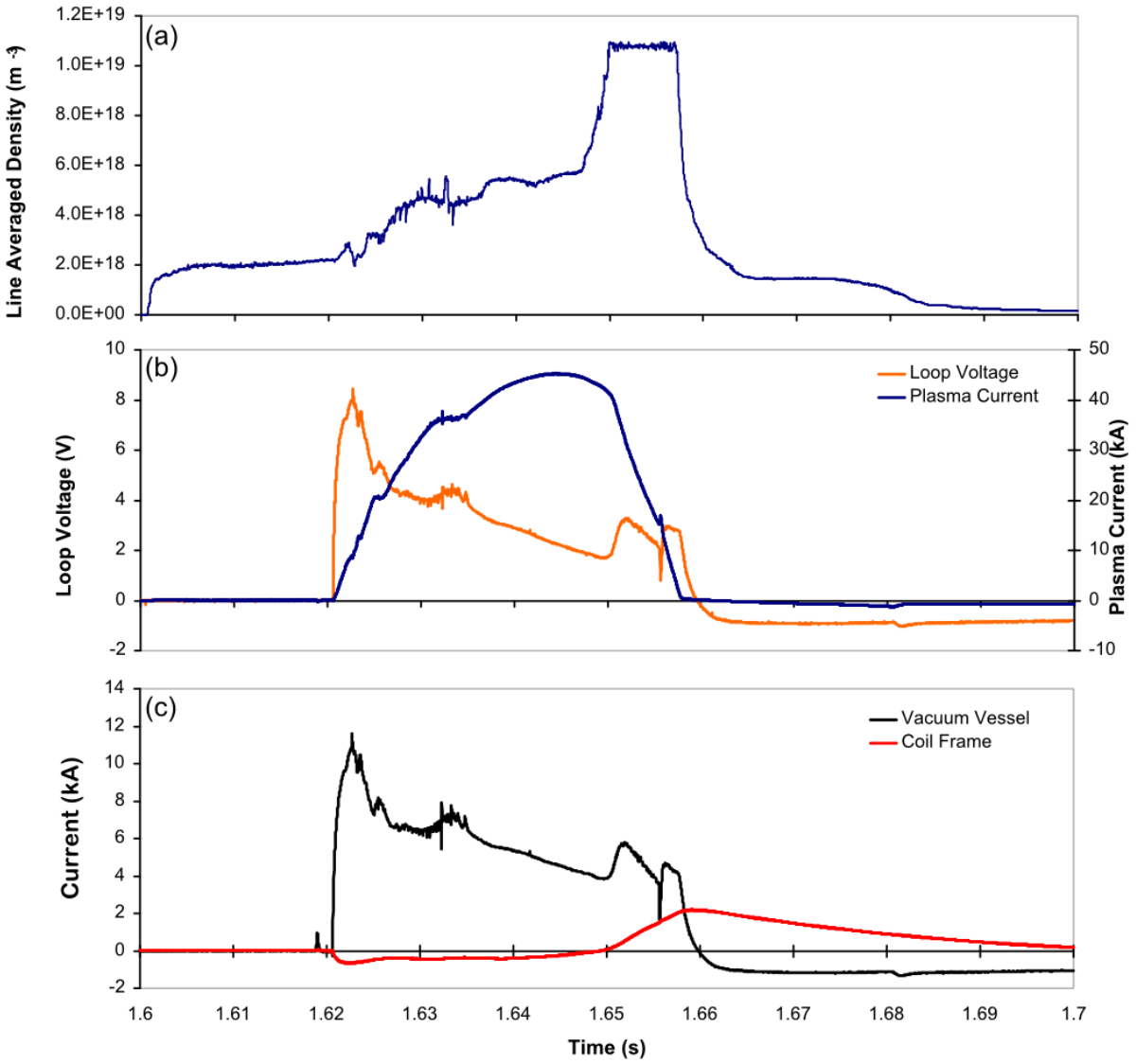

Figure 6.2 – Variation with time of (a) line-averaged electron density, (b) average loop voltage (orange) and toroidal plasma current (blue) and (c) the induced eddy currents in the vacuum vessel and a single coil frame for shot 11050236

produced by the OH coil also drives toroidal vacuum vessel current as well as eddy currents in the coil frame structure. The currents measured during this shot in the vacuum vessel and one of the coil frames are shown in Figure 6.2(c).

The first reconstruction makes use of the signals from 25 Rogowski coils to determine the current density profile at the time t = 1.64 s. The total toroidal plasma current at this time is

measured to be 43.4 kA. The magnetic diagnostic signals used for reconstruction consist of three 8-part Rogowski coils (8PI108, 8PI144, 8PI264) and an internal full Rogowski coil (1PI264). For this reconstruction, the plasma current density profile was modeled as a truncated Gaussian:

$$I'(s) = I'_0 \left[e^{-\left(\frac{s}{a_G}\right)^2} - e^{-\left(\frac{1}{a_G}\right)^2} \right] \tag{6.1}$$

Because the integrated current density must match the total measured current, there is only one free parameter to determine the width of the Gaussian. The pressure was initially assumed to be zero since it was not explicitly measured. Because the pressure profile is an input to the VMEC equilibrium calculation (Sec. 4.1), the pressure was set to 5.0 x 10^{-5} Pa on the magnetic axis which corresponds to a peak density of 1.25x10^{18} m^{-3} and a temperature of 2.5x10^{-5} eV. Clearly this value is certainly well below its expected value of $T_e(0) \sim 200\,\text{eV}$, and reconstructions performed later incorporate a more realistic value of pressure. The positions of two edge limiters were used to constrain the reconstruction process by defining the radial extent of the outer most closed flux surface. The brown shaded regions shown in Figure 6.5 (b) and (d) indicate the positions of these two plasma limiters located at φ=300˚ (5/6 field period) and φ=348˚ (1/6 field period).

The two plasma parameters reconstructed in this example are the total toroidal magnetic flux $\left(\Psi_{t_{tot}}\right)$ enclosed within the last closed flux surface and the width of the Gaussian current profile a_G in Eq. (4.10). The results of the reconstruction are shown in Table 6.1. The initial

	Initial Value	Reconstructed Value
Total Toroidal Flux (Φ_e)	-0.035	-0.0499 ± .0003
Truncated Gaussian a_G	0.7	0.34 ± .05
χ^2	4318.6	161.6

Table 6.1 – Reconstructed equilibrium parameters for truncated Gaussian fit of shot 11050236 at 1.64 s

parameter values were chosen arbitrarily without prior knowledge of the plasma, and not surprisingly the starting value of χ^2 is large. Following reconstruction, the value of χ^2 is reduced to 161.6. The absolute value of the reconstructed total toroidal flux increases from its original value, resulting in a larger last closed flux surface. The total toroidal flux values are negative only because the toroidal magnetic field of CTH points in the $-\hat{\phi}$ direction. The second reconstruction parameter (a_G) is reduced from its initial value, indicating the plasma current has a more peaked current density profile than originally assumed as shown in Figure 6.3. The rotational transform profiles that correspond to the original and reconstructed current density profiles are shown in Figure 6.4. The computed flux surfaces are shown in the surface of section plots of Figure 6.5, demonstrating the effect these two reconstructed parameters have on the shape and position of the equilibrium. The flux surfaces are shown at four different toroidal angles within a field period. The outermost circle in each plot represents the minor radius of the vacuum vessel. The limiters were modeled as full circles with a minor radius corresponding to the minimum minor radius of the physical limiters. These modeled limiters are shown as the inner-most circles in Figure 6.5 (b) and (d). After reconstruction, the last closed flux surface of the computed equilibrium is seen to be tangent to these limiters.

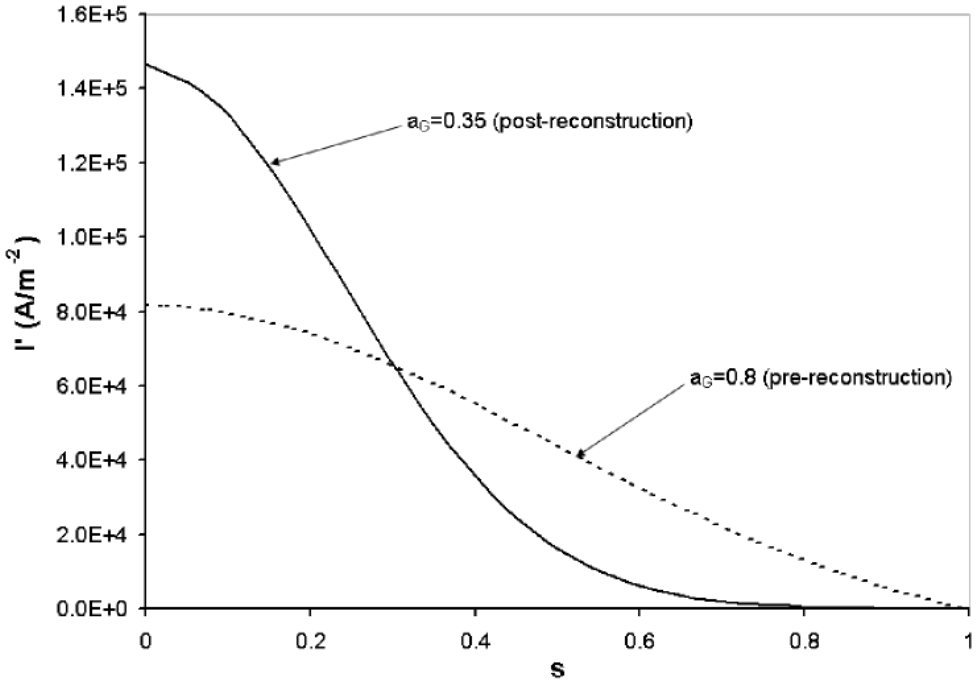

Figure 6.3 – Current density profiles for the initial (dashed) and reconstructed (solid) values of the Gaussian parameter a_G.

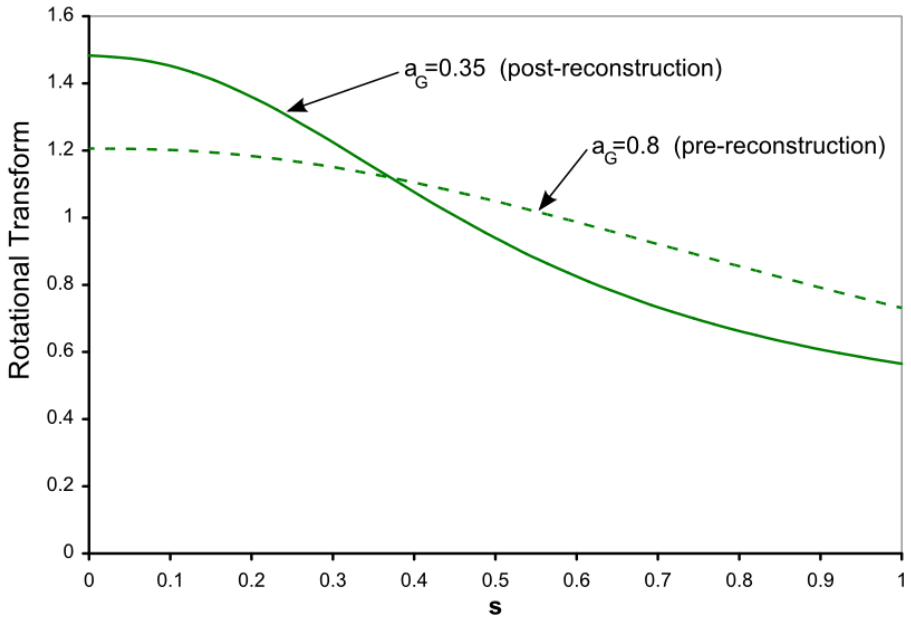

Figure 6.4 – Rotational Transform profiles for the initial (dashed) and reconstructed (solid) values of a_G.

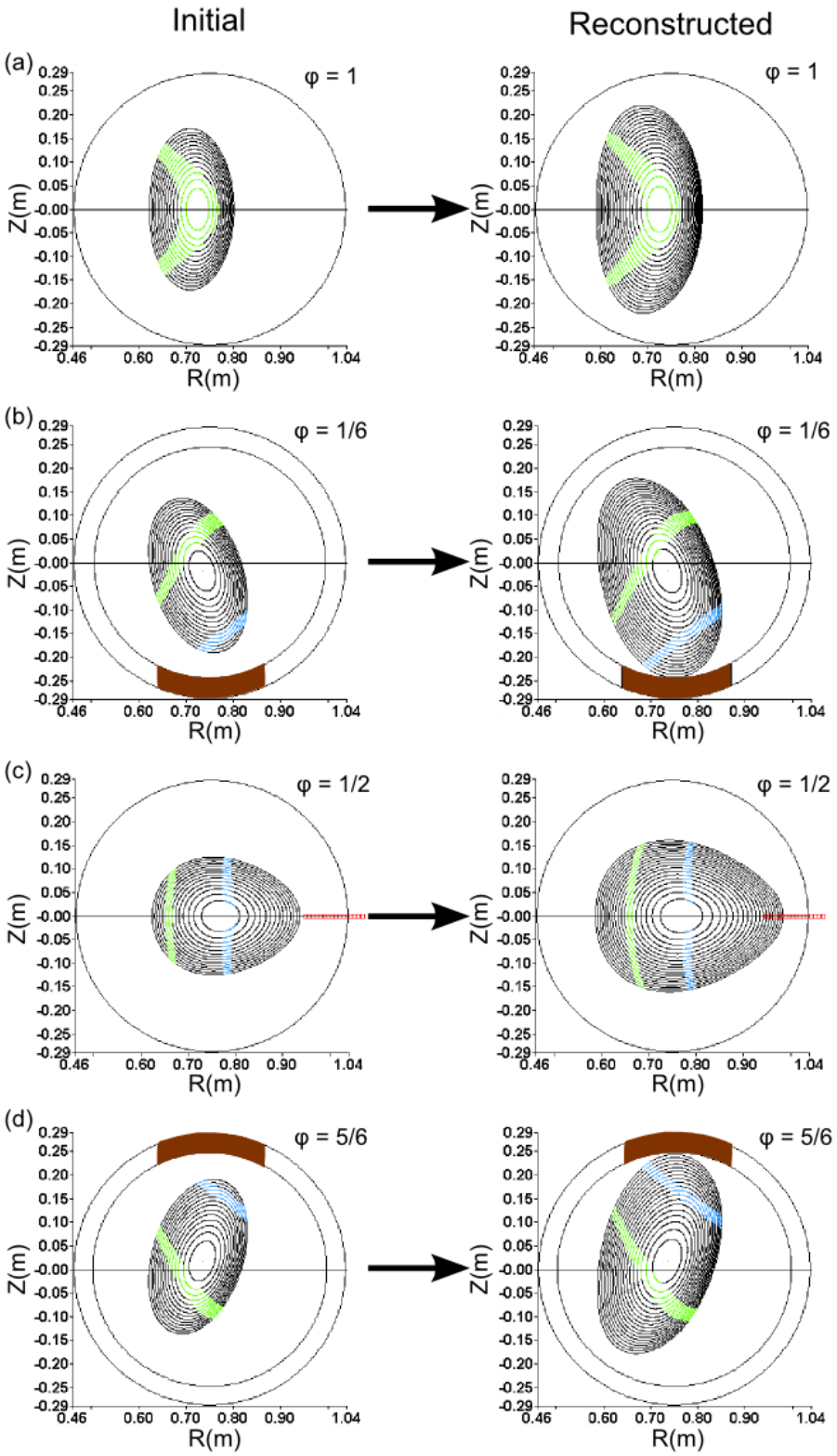

Figure 6.5 – Surface of section plots at four field period locations showing the change which results f rom equilibrium reconstruction of shot 11050236 at 1.64s. Also shown are limiter (brown) and Hall Probe (red) locations.

Based on the number of magnetic diagnostics used in this reconstruction, the ideal χ^2 value is 27, or lower than the final value of 161.6 reached in the reconstruction. Using Eqs. (5.15) and (5.17), the difference of S^M and S^O is:

$$\begin{aligned} S^M - S^O &= S^M_{Plasma} + \sum_j M^M_j I_j - S^O_{Plasma} - \sum_j M^M_j I_j \\ S^M - S^O &= S^M_{Plasma} - S^O_{Plasma} \end{aligned} \tag{6.2}$$

where the terms $\sum_j M^M_j I_j$ cancel. Therefore the value of χ^2, in Eq. (4.13), is directly proportional to the difference of the plasma signals (S^O_{Plasma} and S^M_{Plasma}). The comparison of the modeled and observed plasma signals as a function of poloidal position for the three 8-part Rogowski coils is shown in Figure 6.6. The error bars on the measured plasma signals represent the $1x10^{-4}$ Weber uncertainty assigned to these signals, as discussed in Sec. 5.6. Overall, the reconstructed plasma signals show generally good agreement with the observed signals.

As shown in Figure 6.6, two segments within the Rogowski coil labeled 8PI108 show the largest difference between the measured and modeled signals. The residual difference from these two diagnostics accounts for over 64% of the total minimum χ^2 value. These segments are located at the top ($\theta \sim 90^\circ$) and bottom ($\theta \sim 270^\circ$) of the vacuum vessel (Figure 5.8). To determine the effect of these large residuals on the reconstructed

	Initial Value	Reconstructed Value
Total Toroidal Flux (Φ_e)	-0.035	-0.0500 ± .0003
Truncated Gaussian a_G	0.7	0.34 ± .06
χ^2	4318.6	57.7

Table 6.2 – Reconstructed equilibrium parameters for truncated Gaussian fit of shot 11050236 at 1.64 s without signals from coils 8PI108D and 8PI108H

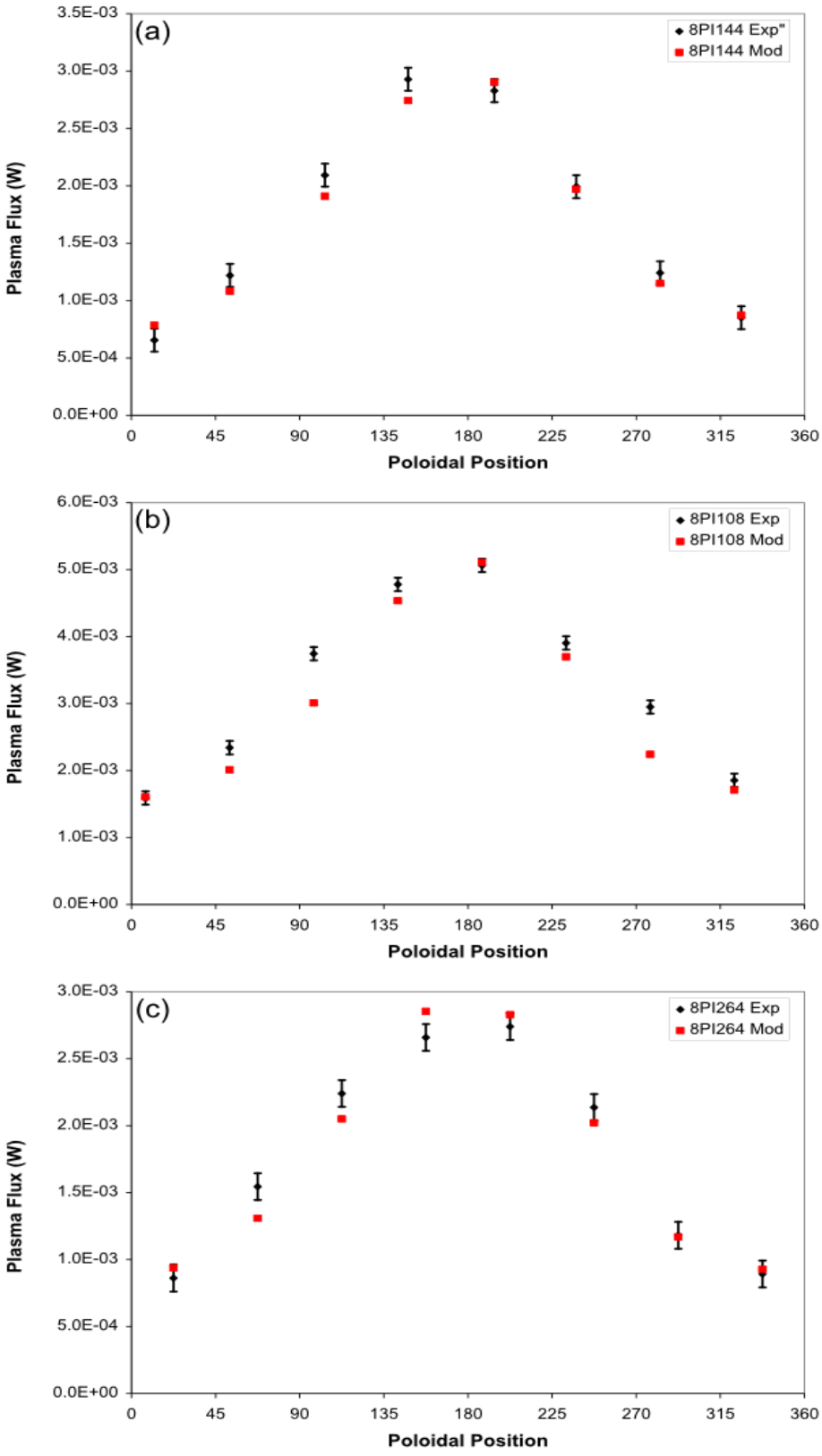

Figure 6.6 – Comparison of observed and modeled plasma contributed flux versus position for the 24 segmented Rogowski coils.

parameters, the reconstruction was repeated without using these two signals as data to be fit. This was achieved by setting the corresponding weighting factors (k_i) of these two diagnostics to zero. The reconstruction results without these two signals are shown in Table 6.2. Although the final χ^2 is over 64% lower than when these signals were included, the reconstructed parameters are no different within their range of uncertainty. Furthermore, the measured and modeled mutual inductance values for these two Rogowski coils in Table 2.1 show close agreement suggesting the differences evident in Figure 6.6 are not due to errors in the diagnostic model. There is thus no evidence that the signals from these particular diagnostic signals have an unusually high error nor that their weight in the reconstruction process should be reduced. That these two diagnostic coils are located 180˚ apart suggests these differences could result from a discrepancy between the model and the actual vertical elongation and/or radial position of the equilibrium. This possibility is discussed at the end of this section. In the work described heron, the weighting factors for these two signals remain the same as the others, i.e. one.

The Gaussian parameterization was not chosen with fore knowledge of the actual profiles. Comparing reconstructed profiles using different current density parameterizations may improve the accuracy of the reconstructions. One example is the current density profile of a second degree polynomial as:

$$I'(s) = \left(\frac{I_{tot}}{\frac{2}{3} + \frac{a_c(1)}{6}} \right) \left[1 + a_c(1)\, s - (1 + a_c(1))\, s^2 \right] \tag{6.3}$$

where I_{tot} is the measured total toroidal current. The parameters $a_c(1)$ and Φ_e are reconstructed using V3FIT. The results of this reconstruction are shown in Table 6.3. The reconstructed value of Φ_e is the same as the previously reconstructed value in Table 6.1. The polynomial parameter

increased during the reconstruction, and the minimum χ^2 value is similar to that found for the truncated Gaussian fit.

	Initial Value	Reconstructed Value
Total Toroidal Flux (Φ_e)	-0.03	-0.0499 ± .0003
2^{nd} order polynomial ($a_c(1)$)	-2.0	-2.42 ± .16
χ^2	7908	161.4

Table 6.3 – Reconstructed equilibrium parameters for polynomial fit of shot 11050236 at 1.64 s

The next current density parameterization uses the so called two-power fit which has the form:

$$I'(s) = I'_0\left[1 - s^{\alpha}\right]^{\beta} \tag{6.4}$$

I'_0 is the peak current density at the magnetic axis. As before, the value of I'_0 is scaled to ensure the integral of $I'(s)$ gives the total toroidal plasma current. Unlike the previous two fits used, this parameterization has two free parameters α and β. However, attempts to reconstruct both the current parameters, α and β, have resulted in uncertainties as large as or larger than the reconstructed parameters themselves. This trend suggests the set of diagnostic signals being used presently are an insufficient constraint to determine more than two parameters. This will be discussed more in Sec. 6.5.

While using the two-power fit, the parameters reconstructed were the total toroidal flux, Φ_e, and the fit parameter α. During this reconstruction, the parameter β was held constant. Different values of β were attempted, and each results in a different reconstructed value of α. However, the reconstructed current density profile changes very little as shown in Figure 6.7. The reconstruction results with β = 5 are shown in Table 6.4.

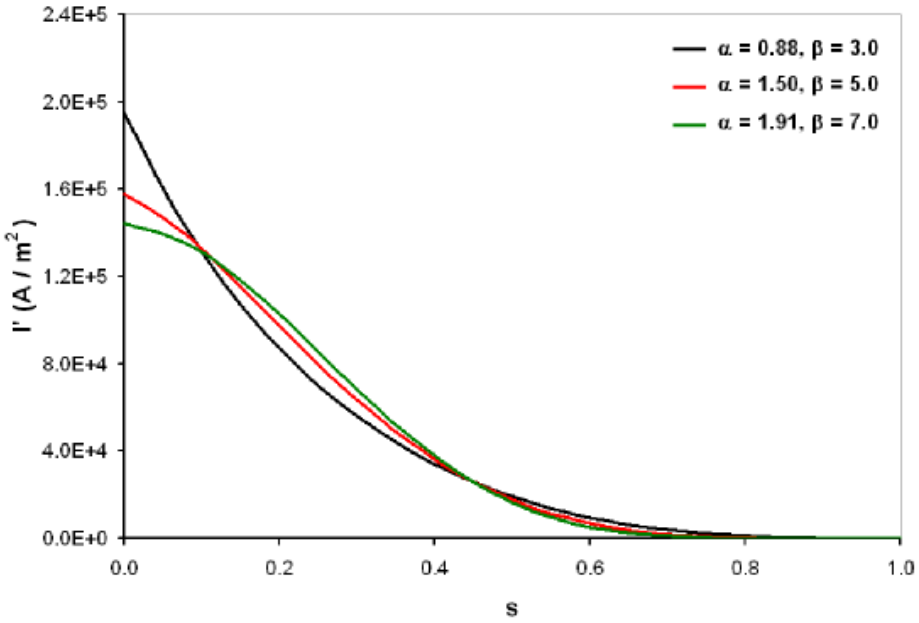

Figure 6.7 – Reconstructed current density profiles using the two-power parameterization with various values of β for shot 11050236 at 1.64s

	Initial Value	Reconstructed Value
Total Toroidal Flux (Φ_e)	-0.035	-0.0499 ± .0003
Two power parameter (α)	3.0	1.50 ± .35
χ^2	4260.1	161.6

Table 6.4 – Reconstructed equilibrium parameters for two-power fit of shot 11050236 at 1.64 s assuming β=5

The minimum χ^2 is similar to that obtained in the two examples shown previously. The reconstructed current density parameter α is reduced to ½ its initial value. These three different reconstructed current density profiles which use different parameterizations are compared in Figure 6.8. The two dashed curves show the initial profiles of the Gaussian and the two-power parameterization. Although the initial conditions and current density parameterizations used were quite different, the final current profiles in all three cases are similar. The shaded region about the two-power profile displays the uncertainty in this profile due to the variance of the reconstructed parameter, α. The polynomial and Gaussian fit predominantly lie within the uncertainty of the two-power fit. For peaked profiles, the quadratic form of the polynomial fit

often results in negative current densities near the edge of the plasma, which is unphysical. The truncated Gaussian fit cannot fit broad profiles effectively because the distribution changes very little once the value of a_G becomes greater than 1. The two-power parameterization however, is able to produce a wide range of current density profiles even when β is held constant. Due to this versatility, the two-power profile is used for the majority of reconstructions being presented.

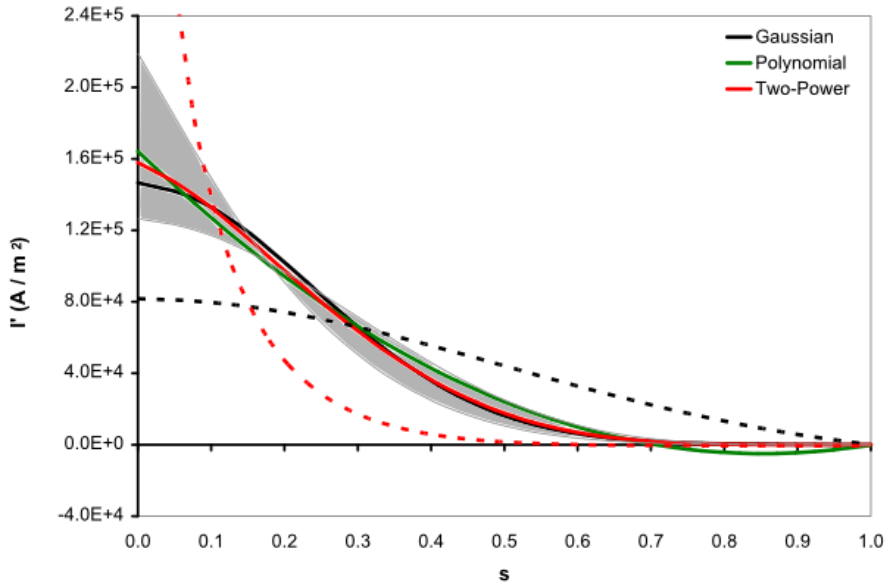

Figure 6.8 – Comparison of reconstructed current density profiles using Gaussian (black), polynomial (green) and the two power (red) fits

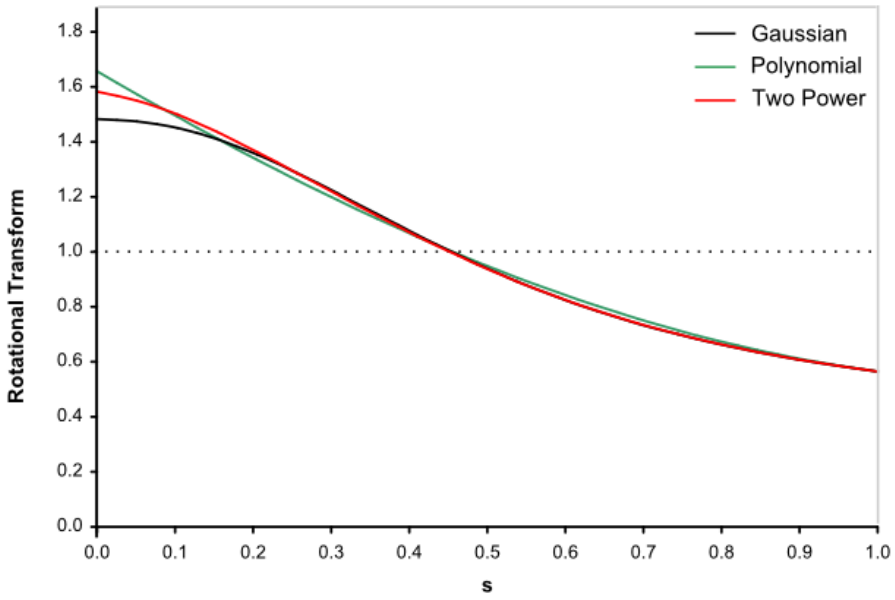

Figure 6.9 – Comparison of rotational transform profiles from reconstructs using Gaussian (black), polynomial (green), and the two power (red) current density profiles for shot 11050236 at 1.64s

The rotational transform profiles determined from these three reconstructions are shown in Figure 6.9. The reconstructed iota profiles are similar to each other, with only a small variation between them evident near the magnetic axis. They each indicate that the rotational transform at the magnetic axis is greater than one. However, this is unphysical if the behavior of these hybrid discharges is similar to tokamaks. Tokamaks are nominally limited to $\iota(0) \leq 1$ by the Kruskal-Shafranov condition[5,43,44]. This limitation of the rotational transform is affected by the sawtooth instability[45]. The sawtooth instability is evidence of the repetitive collapse of the central current density to damp $\iota(0)$ near a value of unity. CTH is similar to a tokamak in that a large fraction of the rotational transform is produced by the toroidal plasma current. Similarly, the central transform of current driven discharges in the earlier W VII-A stellarator have been shown to be limited to $\iota \approx 1$ due to sawtooth oscillations[46]. Therefore it is likely that the sawtooth instability would also limit the rotational transform in CTH plasmas. Evidence of the sawtooth instability is often detected on CTH using the soft X-ray Bremsstrahlung diagnostic array.

However, the magnitudes of soft X-ray signals were too low to detect the sawtooth instability during this shot due to the low density of the discharge. Nonetheless, this instability condition should be considered. To reduce the reconstructed value of $\iota(0)$, the assumed model parameters must be modified.

As mentioned earlier, the central pressure in these examples was taken to be 5×10^{-5} Pa. Recent electron temperature measurements from soft X-ray spectrometry indicate the central electron temperature to $T_{e_0} = 150 - 300$ eV during the ohmic phase of the discharge. Assuming a central density of $n_{e_0} = n_{i_0} = 1.25\times10^{19}$ m^{-3}, an ion temperature of $T_{i_0} = 75$ eV, and an electron temperature of $T_{e_0} = 225$ eV, the peak pressure estimate is $p_0 = 600$ Pa. The pressure profile:

$$p(s) = p_0\left(1 - 2s + s^2\right) \tag{6.5}$$

was assumed. This pressure profile is shown in Figure 6.10. Two of the previous reconstructions were performed again, using the more realistic model of the pressure profile. As shown in Figure 6.11, the reconstructed current density profiles are much broader than when the pressure was

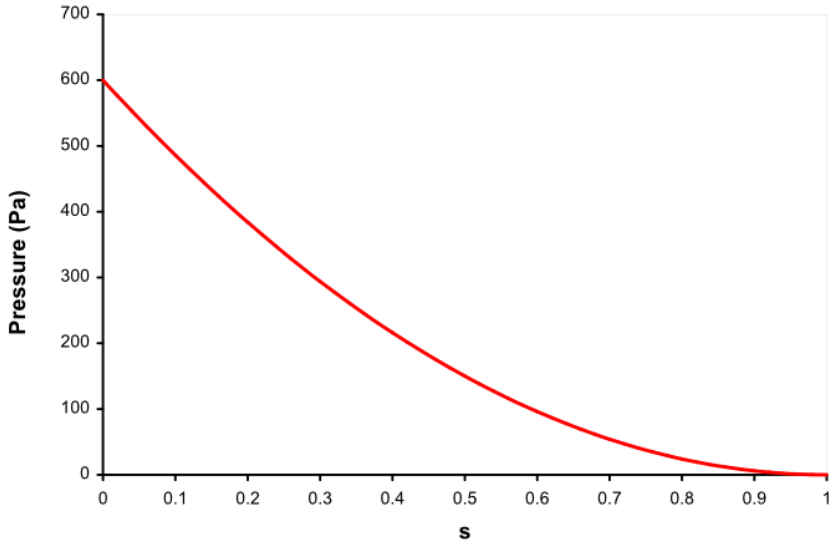

Figure 6.10 – Pressure profile assumed for equilibrium reconstruction of shot 11050236

modeled to be near zero. This trend is expected given the requirement of toroidal force balance in toroidal confinement. If we consider the poloidal field of a large-aspect ratio circular tokamak plasma in equilibrium with current I_{tot}, major radius Ro, and minor radius a, the field is[47]:

$$B_\theta\left[r_a(\theta),\theta\right]=\frac{\mu_0 I_{tot}}{2\pi a}\left[1+\frac{a}{R_0}\left(\beta_\theta+\frac{l_i}{2}-1\right)\cos\theta\right] \tag{6.6}$$

where β_θ is defined as:

$$\beta_\theta=\frac{2\mu_0\langle p\rangle}{B_\theta^2(a)} \tag{6.7}$$

The variable $\langle p\rangle$ represents the average plasma pressure. The internal inductance l_i is defined as:

$$l_i=\frac{2}{a^2 B_\theta^2(a)}\int_0^a B_\theta^2(r)\,r\,dr \tag{6.8}$$

$B_\theta(r)$ is the poloidal magnetic field. In a tokamak, the radial dependence of $B_\theta(r)$ is determined entirely by the current density profile. As seen in Eq. (6.7), a higher pressure corresponds to a higher value of β_θ. For a specific equilibrium value of $B_\theta(a)$, the value of l_i must be reduced if β_θ is raised. A decrease in the internal inductance indicates a broader current density profile, which is the trend shown in Figure 6.11. Moreover, the broader profile results in a reduced rotational transform profile near the magnetic axis, as shown in Figure 6.12. Specifically, the reconstructed values of $\iota(0)$ for each current parameterization are now much closer to one. The reconstructed parameters determined when using the Gaussian fit with a realistic pressure value are shown in Table 6.5. The resulting minimum χ^2 value is only reduced from 161.6 to 158.4 when pressure is included. Similarly, the reconstructed parameters determined using the two-power fit with realistic pressure are shown in Table 6.6. Although the reconstructed current

density parameter α increases significantly, the minimum χ^2 value only changes from 161.6 to 156.5 when pressure is included.

	Initial Value	Reconstructed Value
Total Toroidal Flux (Φ_e)	-0.03	-0.0491 ± .0003
Truncated Gaussian a_G	0.8	0.57 ± .02
χ^2	8062.8	158.4

Table 6.5 – Reconstructed equilibrium parameters for truncated Gaussian fit of shot 11050236 at 1.64 s including a more realistic pressure

	Initial Value	Reconstructed Value
Total Toroidal Flux (Φ_e)	-0.03	-0.0494 ± .0003
Two power parameter (α)	3.0	2.46 ± .78
χ^2	7680.8	156.5

Table 6.6 – Reconstructed equilibrium parameters for two-power fit of shot 11050236 at 1.64 s assuming β=5

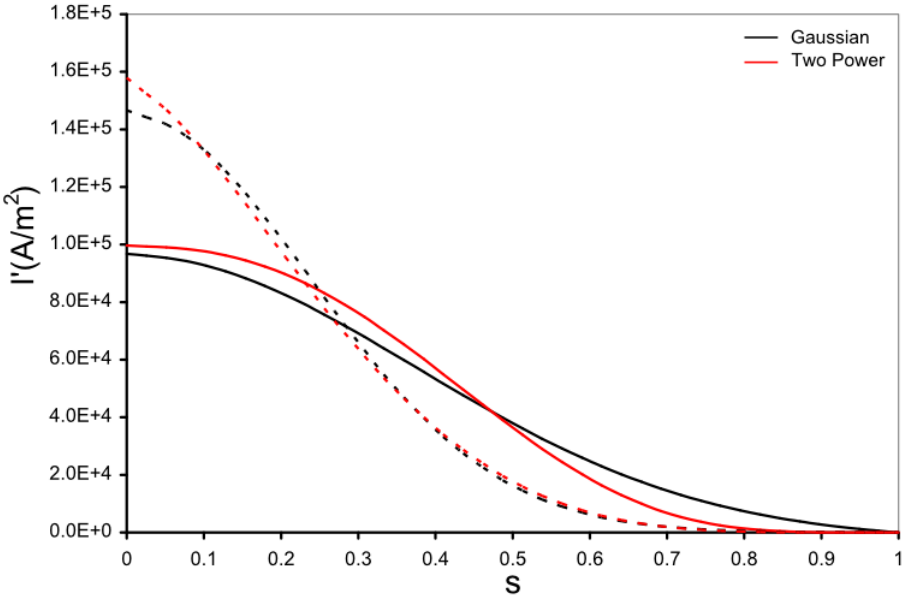

Figure 6.11 – Reconstructed current density profiles for Gaussian (black) and two-power (red) current parameterizations. Solid lines for p_o= 600 Pa and dashed for p_o= $5x10^{-5}$ Pa.

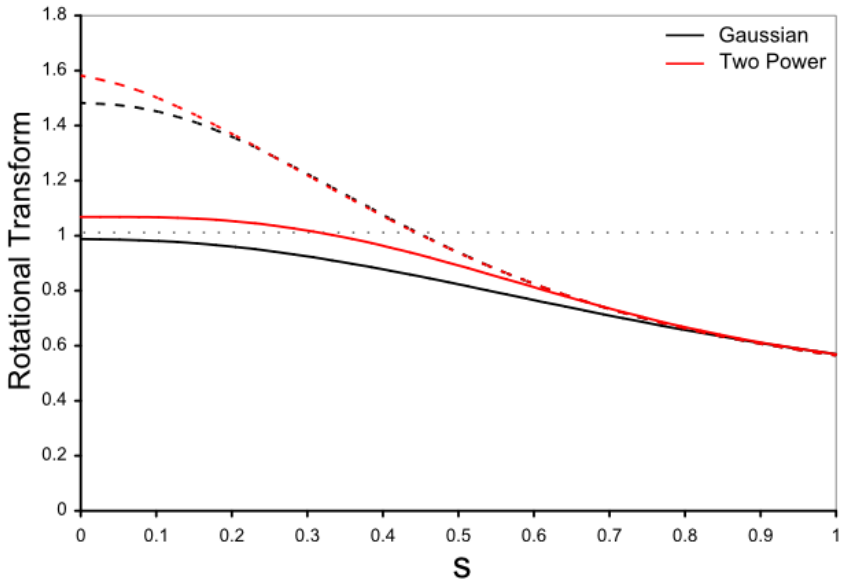

Figure 6.12 – Reconstructed rotational transform profiles for Gaussian (black) and two-power (red) current parameterizations. Solid lines for p_o= 600 Pa and dashed for p_o= $5x10^{-5}$ Pa.

To determine how the plasma equilibrium evolves with time in this particular shot, reconstructions were performed for every 50 μs from 1.623 – 1.656 s. This series of reconstructions uses the two-power function to fit the plasma current density profile. The pressure profile p(r) and central pressure p_0 are taken to be constant during this time. The pressure profile shown in Figure 6.10 is maintained during this series of reconstructions.

The measured plasma current and loop voltage as a function of time are shown again in Figure 6.13 (a). This plot shows a series of hesitations as the plasma current rises which are characteristic of many of the current driven plasma discharges on CTH. There is also an increase in the measured loop voltage during each of these hesitations. The rotational transform at the last closed flux surface ($ι_e$) computed from VMEC is shown in Figure 6.13 (b). From the rotational transform plot, it is clear that each hesitation seen in the rise of the plasma current corresponds to the rotational transform near the edge of the plasma having a rational value, e.g. $ι_e$ = ¼, ⅓, and ½.

Figure 6.13 (c) displays the reconstructed total toroidal flux (Φ_e) as a function of time. The grey error bars shown in Figure 6.13 (c) and (d) represent the square root of the posterior variances for these reconstructed parameters, calculated by V3FIT. The magnitude of Φ_e increases as the plasma current increases until $\iota_e = ½$. During the interval over which $\iota_e = ½$, the magnitude of Φ_e increases while the plasma current remains relatively constant. The time evolution of the current density profile parameter α is shown in Figure 6.13 (d). Larger values of α indicate a broader current density distribution. During the times when the plasma current is ramping up, the width of the current profile changes very little. However, during the hesitations in the current ramp, the current density distribution becomes significantly more peaked. This trend is seen both when the edge rotational transform is ½ and ⅓. Similar trends were reported for the current ramp stage of the T-4 tokamak in which the current distribution underwent a series of collapses corresponding to the presence of rational surfaces on the plasma edge[48].

The increases in the measured loop voltage seen during these periods of constant plasma current could indicate several processes taking place. The toroidal loop voltage at the plasma surface is the sum of a resistive term and an inductive term:

$$V_{loop} = I_{Plasma} R_{Plasma} + \frac{d}{dt}\left(L_{Plasma} I_{Plasma}\right) \tag{6.9}$$

where I_{Plasma} is the plasma current, R_{Plasma} is the plasma resistance, and L_{Plasma} is the plasma inductance. With I_{Plasma} constant, an increase in loop voltage may be due to either an increase in the resistance or internal inductance of the plasma. One possible explanation of these results is that the presence of the rational surface near the edge may result in an enhancement of

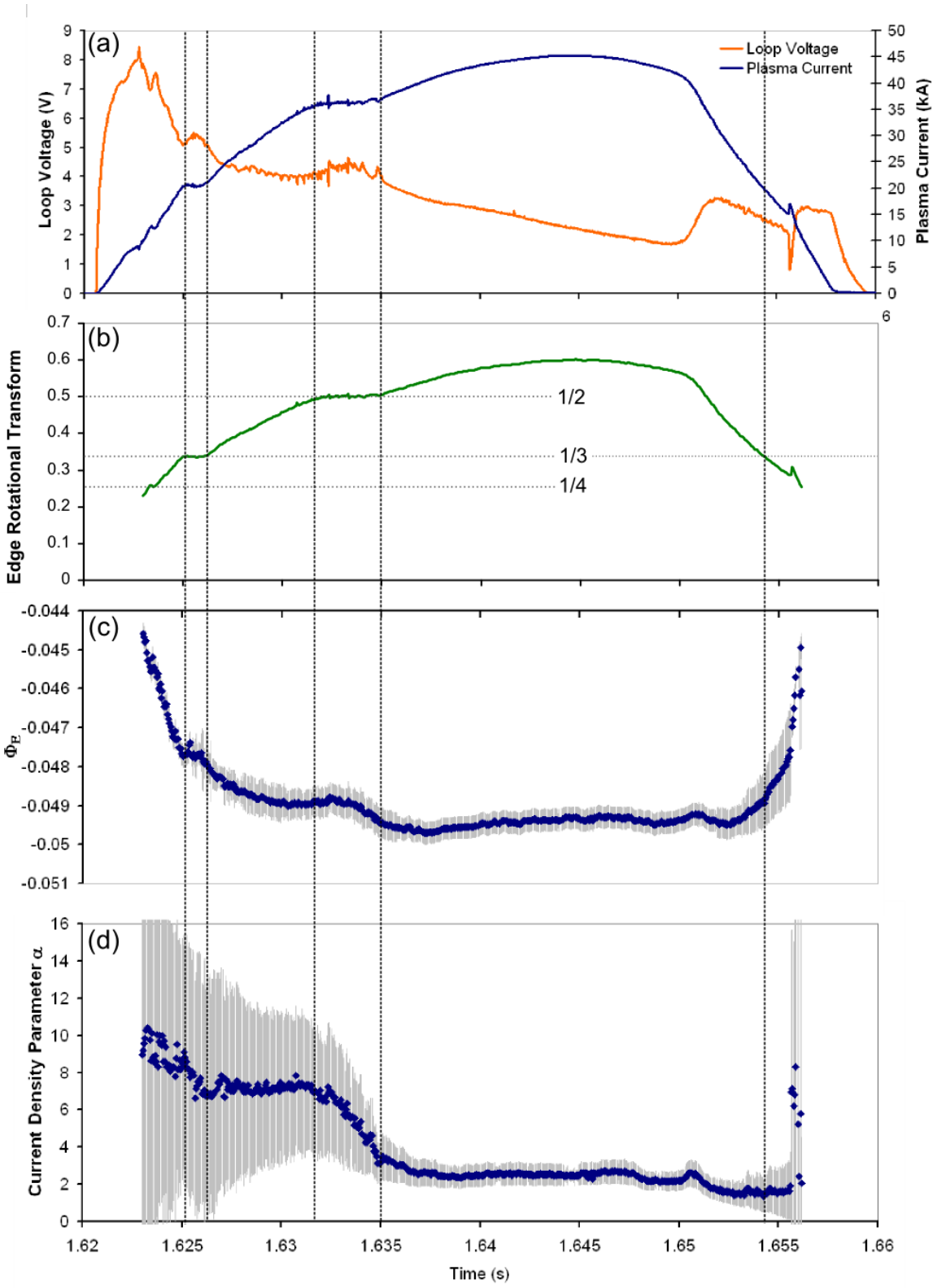

Figure 6.13 – Reconstruction results vs time for shot 11050236, including (a) plasma current and loop voltage, (b) edge rotational transform, (c) total toroidal flux, and (d) current density profile parameter α.

the local plasma transport. When the plasma interacts with the wall, the temperature in this region is likely reduced perhaps due to increased radiation and/or increased parallel transport of energy along open magnetic field lines. Assuming the center of the plasma still has a relatively higher temperature and therefore lower resistance, the current density profile will become more peaked. Based on Eq. (6.8), the higher central current will lead to an increase in the plasma's internal inductance. The reconstructed current density parameter shows the current channel is becoming increasingly more peaked during these times which would result in an increase in the plasma's internal inductance.

The change in the current density profile when the edge rotational transform is ⅓ is shown in Figure 6.14. The times corresponding to these profiles are indicated by vertical lines in Figure 6.13. This shift in the plasma current profile is due to a redistribution of the current given that the total plasma current does not change. A more pronounced shift in the plasma current profile occurs between the times 1.6315 s and 1.635 s when the edge rotational

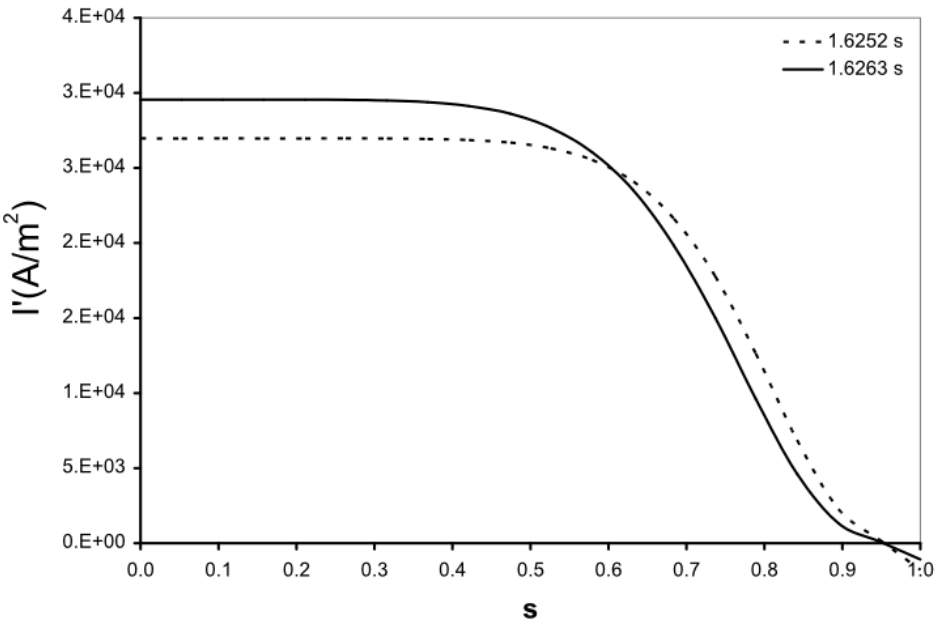

Figure 6.14 – Change in current density profile seen when edge rotation transform is ⅓

transform is $\iota_e = ½$. This trend is shown in Figure 6.15. Once again, this change in the current density profile is a result of a redistribution of the current channel since the total plasma current remains relatively constant.

Although the presence of a rational surface at the edge of the plasma significantly affects the current density profile and magnitude when the plasma current is ramping up, similar effects are not seen during the current ramp down. This is clearly seen in Figure 6.13 (a) and (b) by the absence of a hesitation in the current ramp down when the edge rotational transform is ½ or ⅓. Figure 6.16 shows two reconstructed current density profiles, both of which have an edge

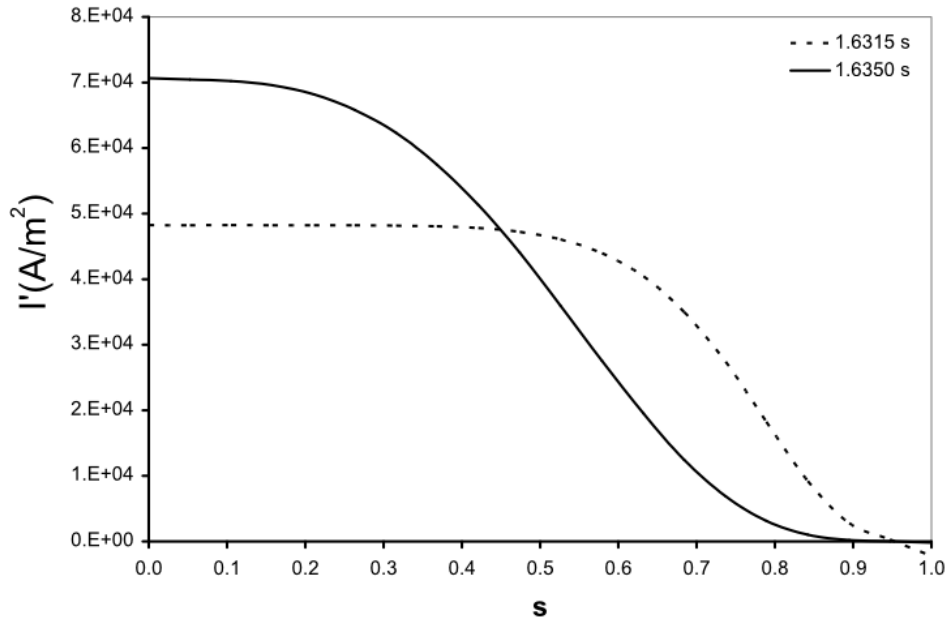

Figure 6.15 – Shift in current density profile observed when edge rotational transform is ½.

rotational transform value of ⅓. The current density profile is much broader during the time when the current ramps up than when the current is decreasing. Previous results on W VII-A have shown that plasmas are more stable to tearing mode instabilities when the current density does not have a strong gradient in the region near a rational surface[46]. As shown in Figure 6.16,

the gradient of the current density at 1.6252 s is much steeper near the plasma boundary where $\iota_e = \frac{1}{3}$ than it is when the current is ramping down. This trend determined using equilibrium reconstruction is consistent with the W VII-A results.

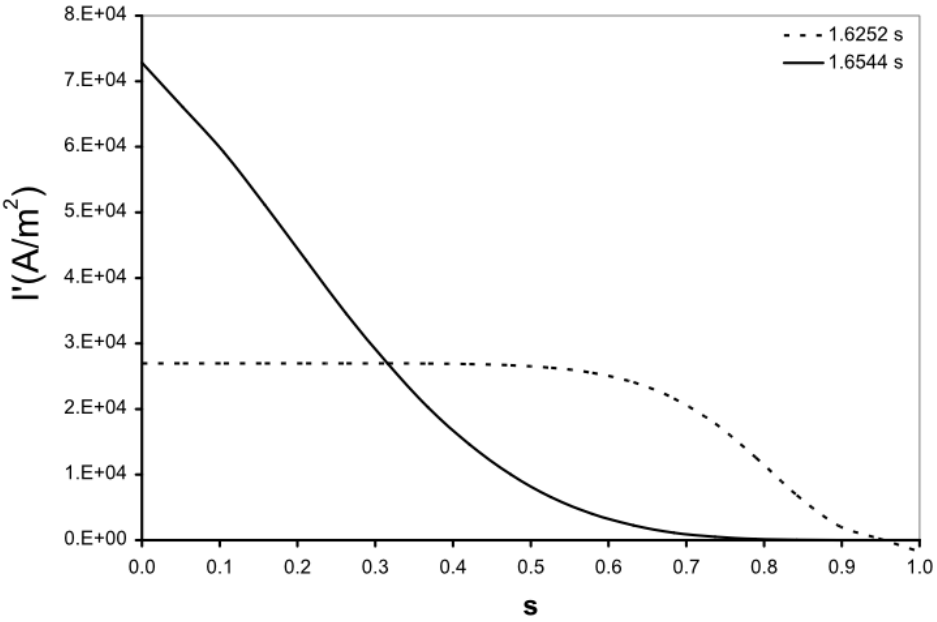

Figure 6.16 – Reconstructed current density profiles each with $\iota_e = \frac{1}{3}$, one during the current rise (dashed), and one during the current decay (solid)

The reconstructed results shown in Figure 6.13 (c) and (d) smoothly change in time and the series of sudden changes in the current density profile during the current ramp are consistent with previously published results[48]. However, the final values of χ^2 are still higher than the optimal value. The minimum χ^2 values achieved during this series of plasma reconstructions are shown in Figure 6.17. In the absence of systematic error, the values in this plot should be randomly distributed. However, the plot shows a trend that resembles the time evolution of the measured plasma current. Again, the value of χ^2 that is reached is largely dependent on the diagnostics 8PI108D and 8PI108H. The difference between the modeled and measured plasma signals for diagnostic 8PI108D and 8PI108H are shown in Figure 6.18 for these sequential reconstructions. The residual from these two diagnostics are responsible

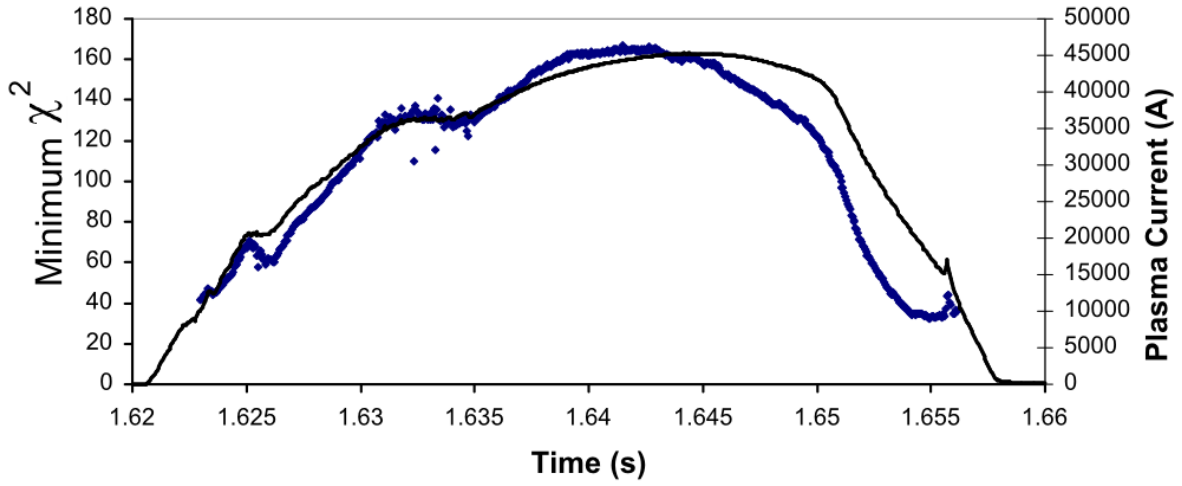

Figure 6.17 – Minimum χ^2 (in blue) achieved during plasma reconstructions and plasma current (black) during shot 11050236

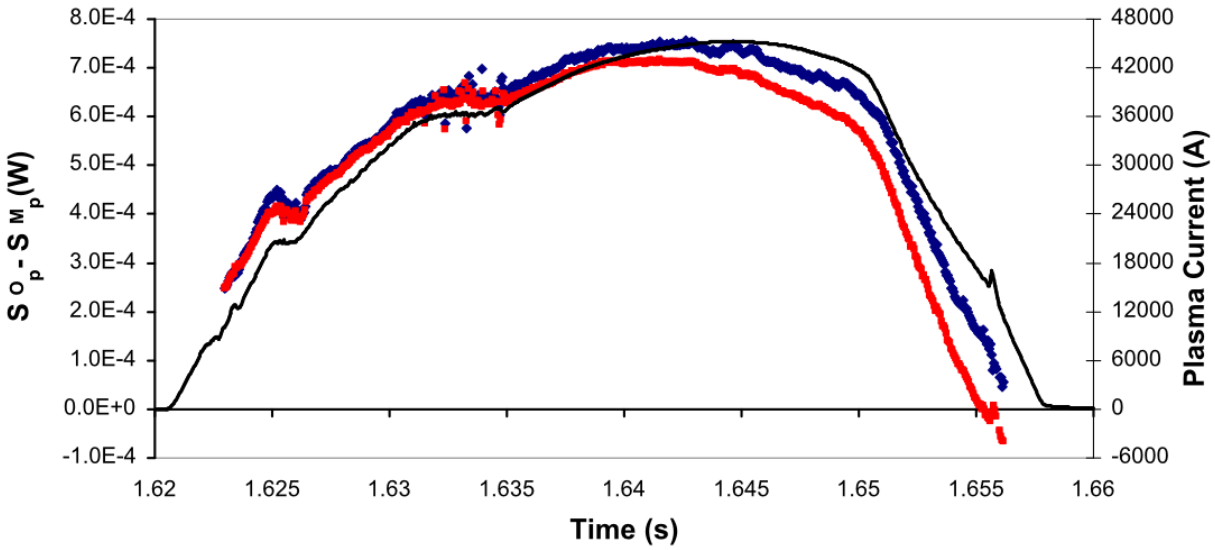

Figure 6.18 – Difference of observed and modeled plasma signals versus time for diagnostics 8PI108D (blue) and 8PI108H (red) overlaid with the plasma current (black) for shot 11050236

for between 40 – 65 % of the final χ^2 values shown in Figure 6.17, where the largest percentages correspond to when the plasma current is the highest.

The trend in the minimum χ^2 with plasma current suggests there is a related systematic measurement error in the reconstruction. This could result from an incorrect gain in the modeled

or experimental diagnostics. However, the agreement in the mutual inductances seen in Table 5.1 suggest that this is not the source of the systematic error. Another possible source of error is the measurement of the plasma current. In order to test this hypothesis, the total plasma current (I_{tot}) was allowed to vary as a reconstruction parameter within V3FIT along with the total toroidal flux (Φ_e) for the time 1.64 s into shot 11050236. During this reconstruction, the previously reconstructed parameter α, was set to the value shown in Table 6.7. The plasma current only increased by 0.3%, as shown in Table 6.7, and the small reduction in χ^2 indicates that the plasma current measurement is not the source of the remaining systematic error. However, if the signal weight (k_i) of the full Rogowski coil is set to zero, the same equilibrium reconstruction results in a 5% higher plasma current and a 26% lower χ^2 as shown in Table 6.8. Although this χ^2 value is substantially closer to the optimal value, it clearly shows that scaling the total current is not a sufficient correction. It also implies the calibration of Rogowski coil 1PI264 should be rechecked.

	Previous Results (Table 6.6)	Reconstructed Value
Total Toroidal Flux (Φ_e)	-0.03	-0.0493 ± .0003
Total Plasma Current (I_{tot})	43407 A	43560 ± 96 A
χ^2	157	153.8

Table 6.7 – Optimization of total plasma current using V3FIT for shot 11050236 at 1.64 s

	Previous Results (Table 6.6)	Reconstructed Value
Total Toroidal Flux (Φ_e)	-0.03	-0.0488 ± .0003
Total Plasma Current (I_{tot})	43407 A	45760 ± 370 A
χ^2	157	115.8

Table 6.8 – Optimization of total plasma current using V3FIT without the full Rogowski coil (1PI264) for shot 11050236 at 1.64 s

As previously mentioned, the diagnostics 8PI108D and 8PI108H are located at the top and bottom of the vacuum vessel as shown in Figure 5.8. The modeled values of the poloidal flux at these locations are consistently smaller than the experimentally measured values. This indicates the reconstructed flux surfaces could extend further in the vertical direction than

assumed. The elongation of the reconstructed plasma equilibrium can be adjusted within the model by adding SVF current. Although several values of SVF current were tried, the example which resulted in

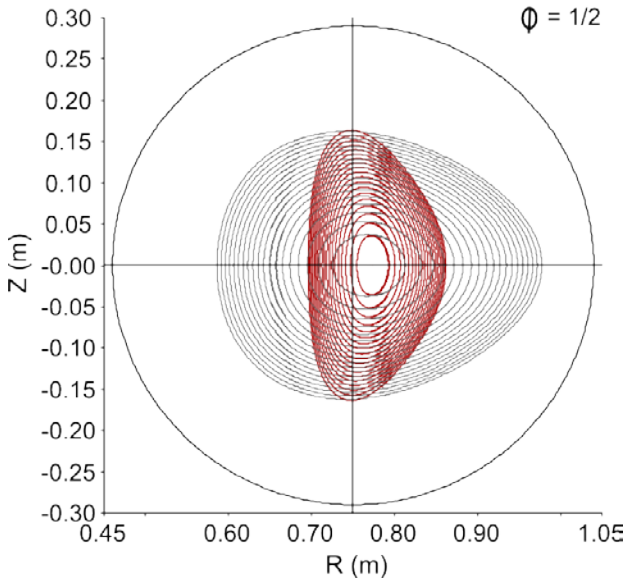

Figure 6.19 – Reconstructed flux surfaces with SVF quadrupole field (red) and without (black)

the largest reduction in χ^2 requires 3000 A. The addition of this quadrupole field also changes the average radial position of the magnetic axis. To correct for this shift, the modeled TVF current was increased by 750 A to maintain the average radial position of the equilibrium. With these additional modeled currents, the parameters Φ_e, and α were again reconstructed using V3FIT. The effect of the quadrupole field on the reconstructed flux surfaces are shown in Figure 6.19. This surface-of-section plot is for the same field-period location as the diagnostics 8PI108D and 8PI108H. The reconstructed parameters are listed in Table 6.9 along with the values previously

	Without SVF	With SVF
Total Toroidal Flux (Φ_e)	-0.0494 ± .0003	-0.0205 ± .0035
Two power parameter (α)	2.46 ± .78	6.52 ± .49
χ^2	156.5	119.7

Table 6.9 – Reconstructed parameters with and without modeled SVF current for shot 11050236 at 1.64 s

reconstructed without SVF current. The elongation of the flux surfaces by the quadrupole field causes the modeled surfaces to encounter the edge limiter at a much smaller value of Φ_e. The result of this smaller Φ_e is that the vertical extent of the last closed flux surface at this field-period location is unchanged. However, the larger value of α indicates a much broader current profile, so although the radial extent of the flux surfaces in these regions has not changed, the current channel is effectively closer. The addition of the SVF does in fact result in a 24% reduction in the minimum χ^2 value. However, it should be noted that these modified values of I_{SVF} and I_{TVF} are unreasonable and are not justified based on experimental measurements.

The next attempt to reduce the systematic error is to combine the effect of elongation with the scaling of the total plasma current. For this test, the SVF and TVF currents were shifted as in the previous example, but this time, the total plasma current parameter (I_{tot}) was reconstructed along with Φ_e, and the current density parameter α was kept constant at 2.46. The reconstruction results are shown in Table 6.10. These two adjustments reduced the minimum χ^2 value by 63%. However, it is quite unlikely that there exists an unknown external current which would produce such a strong quadrupole field. Further testing will be required to determine the cause of the remaining systematic error which is explicable by an effective elongation of the plasma, but not physically reasonable.

	Previous Results (Table 6.6)	Reconstructed Value
Total Toroidal Flux (Φ_e)	-0.03	-0.0215 ± .00003
Total Plasma Current (I_{tot})	43407 A	46030 ± 375 A
χ^2	157	58.1

Table 6.10 – Optimization of the plasma current using V3FIT with modeled SVF current for shot 11050236 at 1.64 s

6.2 Reconstruction Analysis of a Current Disruption

One of the goals of the CTH project is to investigate how plasma disruptions are affected by 3D shaping of the equilibrium flux surfaces. A disruption is the term used to describe a sudden loss of plasma confinement which results in a sudden decrease in the plasma temperature immediately followed by a decrease in the plasma current. Plasma disruptions are of interest because they represent operational limits in the current and density of tokamak plasmas[6]. This section includes the reconstruction results from a shot in which a plasma disruption occurs. The trends in the reconstructed parameters are compared with the previously described shot in which no disruption occurs.

The vacuum rotational transform for this shot is also $0.10 \leq \iota(s) \leq 0.13$. The current in the external magnet coils are the same as shown in Figure 6.1.

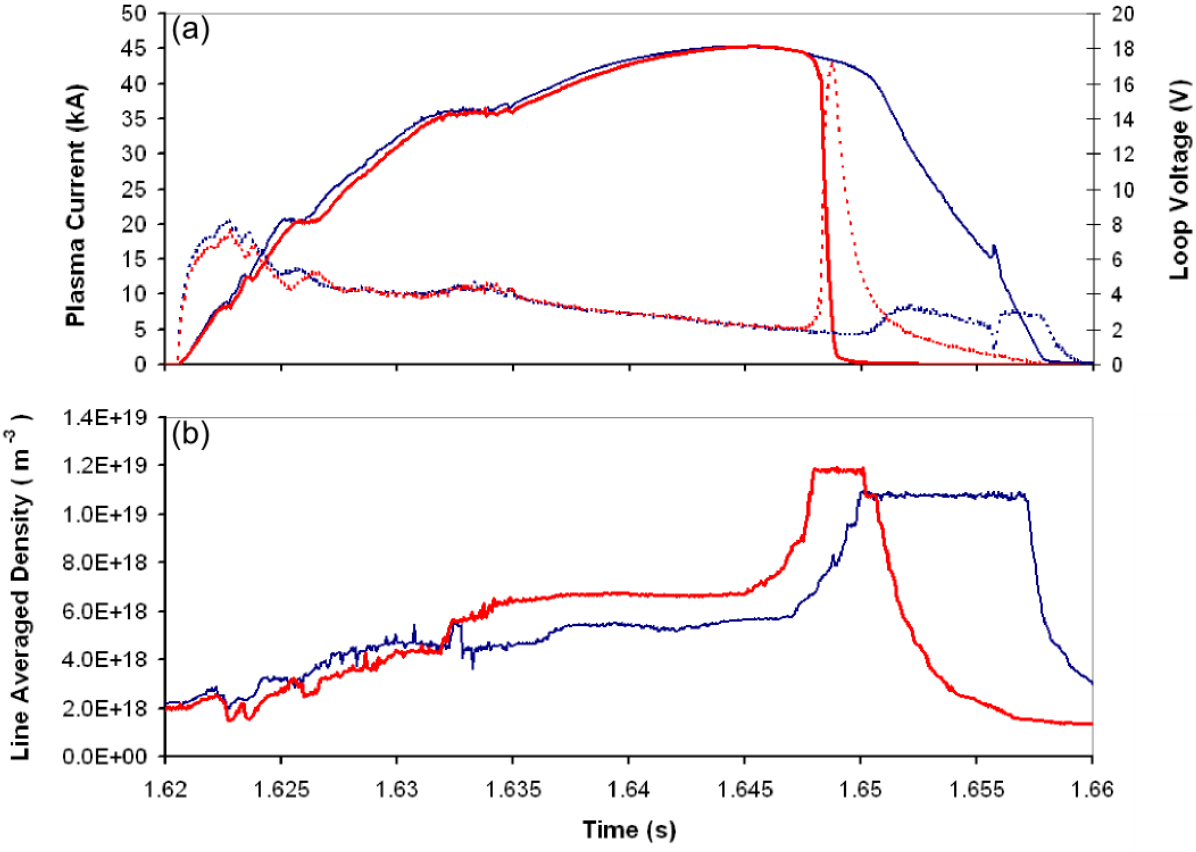

Figure 6.20 – (a) Plasma current (solid) and loop voltage (dashed) measured during shots 11050236 (blue) and 11050240 (red) and the line-averaged electron density for these two shots shown in (b)

The evolution of the plasma current and loop voltage are compared to the previous shot in Figure 6.20 (a). These two shots are nearly identical until the disruption occurs at 1.648 s. The large increase in loop voltage is characteristic of plasma disruptions. This is understood to be caused by a sudden decrease in plasma temperature which increases the resistance[5]. A comparison of the density traces is shown in Figure 6.20(b). Although the general trend is the same, the shot in which the plasma disrupts does show a higher density during the time when the current is highest. The Hall probe array was positioned within the plasma during these shots, and the rise in density appears to be an effect of plasma interactions with the probe. After the disruption, the density decays to a level characteristic of plasmas heated using only ECRH. The magnetic flux surfaces produced by the external coils presumably are present after the disruption. This is distinctly different from major disruptions within a tokamak which typically result in the termination of the plasma discharge. As the plasma current decays to zero in a tokamak, the poloidal field required for toroidal confinement is no longer present.

As before, a series of equilibrium reconstructions are performed for every 50 μs from 1.623 – 1.656 s. For these reconstructions, the two-power function Eq. (6.4) is used to fit the plasma current density profile, and the pressure profile is again held constant with a peak pressure of p_0 = 600 Pa. The reconstructed parameters are the total toroidal flux, Φ_e, and the two-power current density exponent α. The parameters along with the plasma current and edge rotational transform are shown in Figure 6.21. The parameters from the previously reconstructed shot which did not disrupt are also shown for comparison. Over the first half of the shot, the evolution of the reconstructed parameters is similar with the previously reconstructed shot. However, several differences appear just before the disruption occurs. At 1.6464 s the current density

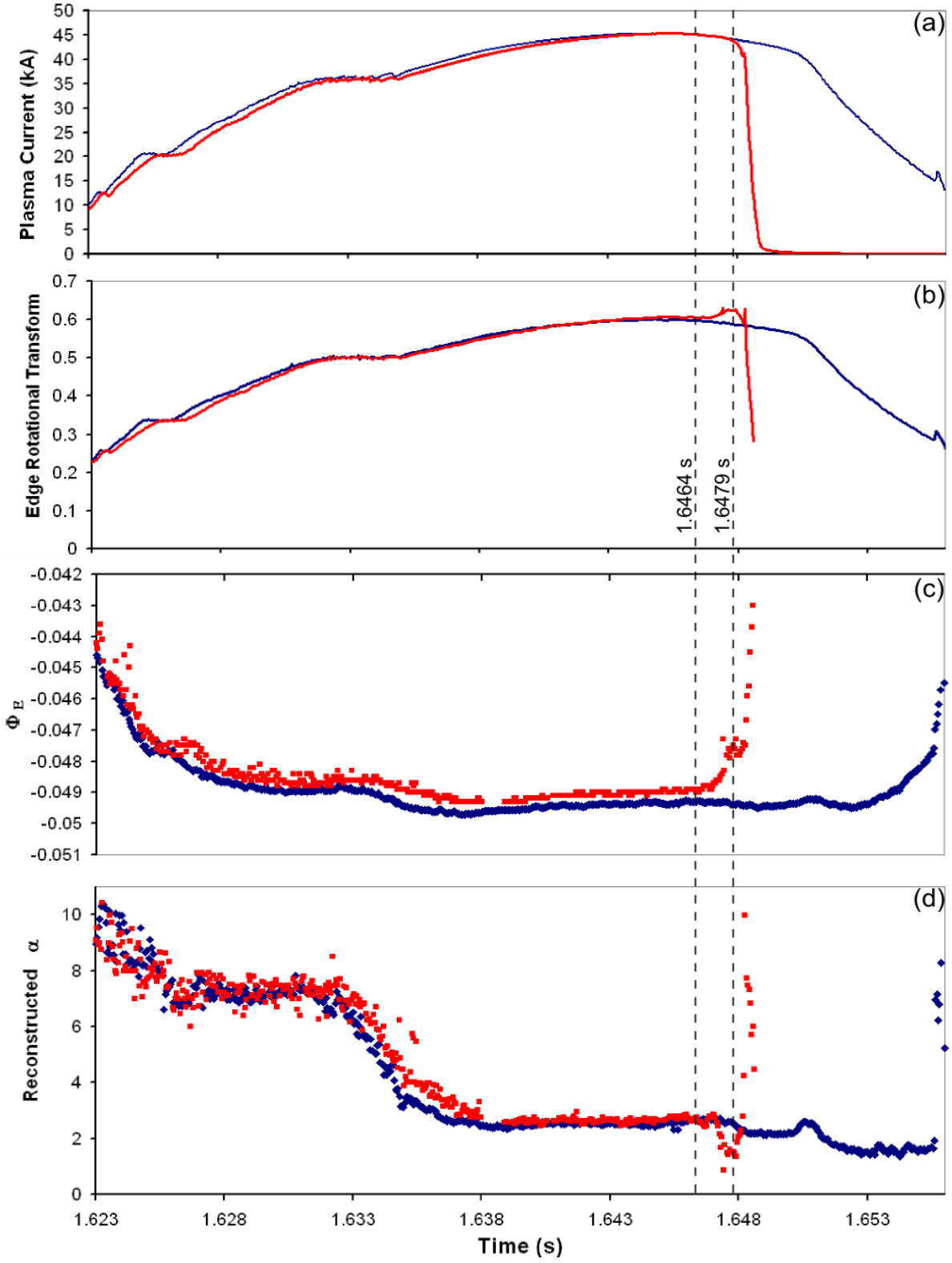

Figure 6.21 – Comparison of reconstructed results from shots 11050236 (blue) and 11050240, including (a) plasma current, (b) edge rotational transform, (c) total toroidal flux, and (d) current density profile parameter α

parameter α decreases slightly to indicate a peaking of the current profile, but then returns to its previous value. At this point, the current density again becomes more peaked (α decreases) and the total toroidal flux begins to decrease in magnitude, which indicates that the minor radius of the plasma is decreasing. As the minor radius decreases, the rotational transform at the edge becomes higher as seen in Figure 6.21(b). At 1.6479 s, the plasma current begins to decrease, and the current density profile again broadens. The plasma current channel begins to fully collapse at 1.6482 s marked by sudden changes in each of the reconstructed parameters.

Disruptions in tokamak discharges are often due to large tearing mode instabilities associated with the spatial location of the $\iota = ½$ rational surface. A set of rotational transform profiles along with the associated current density profiles are shown in Figure 6.22 which

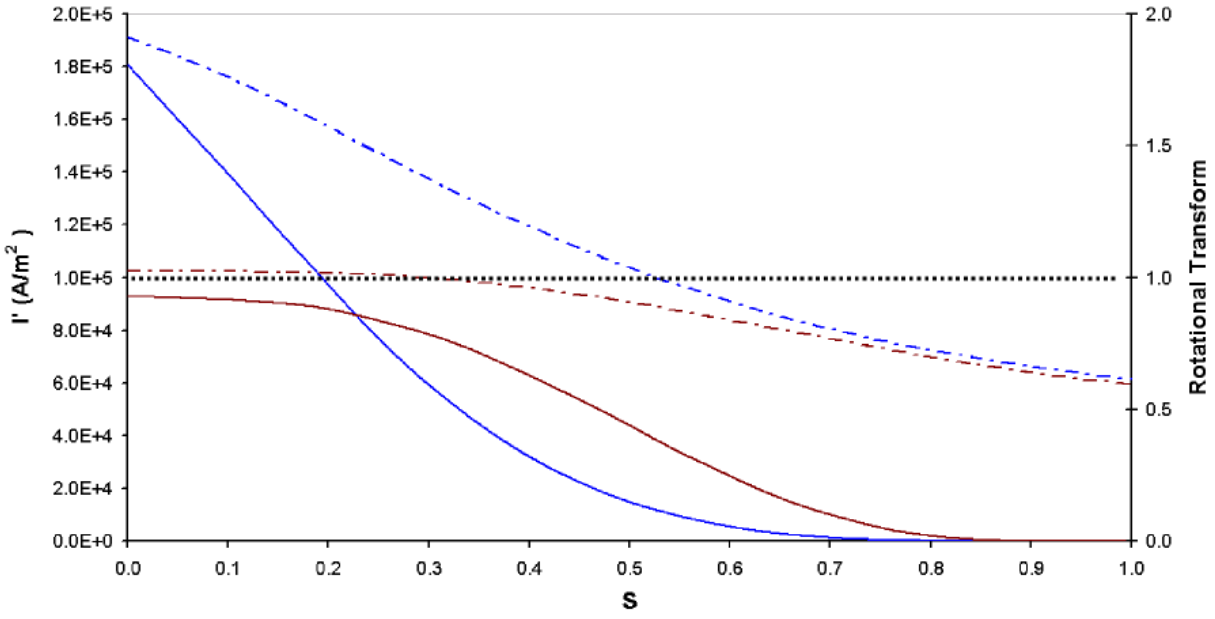

Figure 6.22 – Current density profiles (solid) and rotational transform profiles (dashed) for 1.6464 s (blue) and 1.6479 s (brown) into shot 11050240

correspond to the two times indicated by dashed lines in Figure 6.21. The reconstruction results indicate the rational surface $\iota = ½$ is outside the last closed flux surface. However, when the current density becomes more peaked at 1.6479 s, the $\iota = 1$ surface is substantially closer to the

edge of the plasma. One of the causes of disruptions in tokamaks is a local increase in the concentration of impurities near the edge of the plasma. The impurities increase the radiative cooling along the edge which causes the current profile to contract. As it contracts, the edge rotational transform can reach unstable rational surfaces which can cause disruptions.[6] A similar behavior is likely the cause of this disruption. That is impurities introduced to the edge of the plasma by the Hall probe, are likely the cause of the current profile contraction. As the profile contracts, the effective edge of the plasma approaches the $\iota = 1$ rational surface and becomes unstable which results in a disruption.

6.3 Reconstructions with low vacuum transform

A key area of fusion energy research is the ability to control current-driven instabilities in tokamak devices which often result in current disruptions. Moderate 3D shaping of the magnetic flux surfaces have been shown to effectively control instabilities such as resistive wall modes and edge localized modes in tokamak geometries. Research efforts on CTH are aimed at studying the effect of more substantial 3D shaping on current-driven instabilities. In order to investigate this effect, it is necessary to first recreate the tokamak-like magnetic field configuration which produces the disruptive instabilities. On CTH, this is achieved by minimizing the vacuum rotational transform, such that a larger fraction of the required poloidal field is produced by the plasma current. The next example of equilibrium reconstruction was performed on shot 11051954 which was configured to have a lower vacuum rotational transform of $0.059 \leq \iota(s) \leq 0.063$ compared to the previously reconstructed shots which were from $0.10 \leq \iota(s) \leq 0.13$. The external coil currents used to create this vacuum transform are shown in Figure 6.23. In addition to the HF, TVF, and OH coils used in the previously reconstructed shot, current

was also passed through the TF coil to produce the low vacuum transform. The timing of the ECRH plasma generation and Ohmic current drive is the same as in the previously presented shots. The measured loop voltage and resulting toroidal plasma current are shown in Figure 6.24 (a). The maximum plasma current is 5 kA higher than in the previous shots. The line-averaged electron density is shown in Figure 6.24(b). More gas was puffed in during this shot than in the previous examples, and results in approximately twice the peak density.

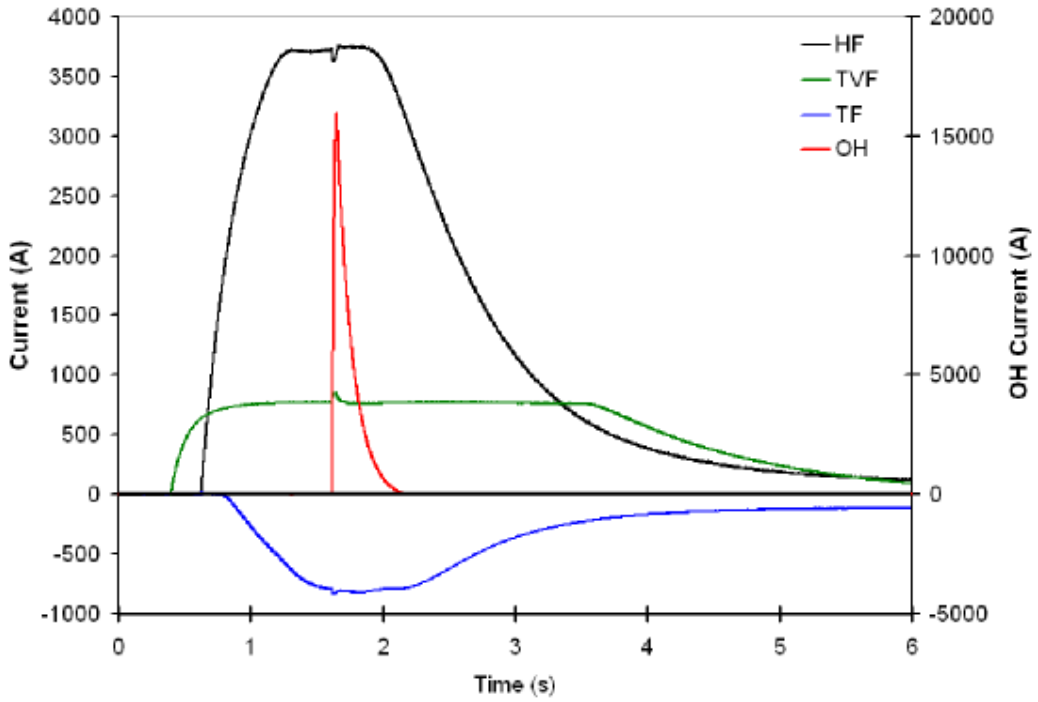

Figure 6.23 – Time evolution of HF (black), TVF (green), TF (blue), and OH (red) external coil currents for shot 11051954

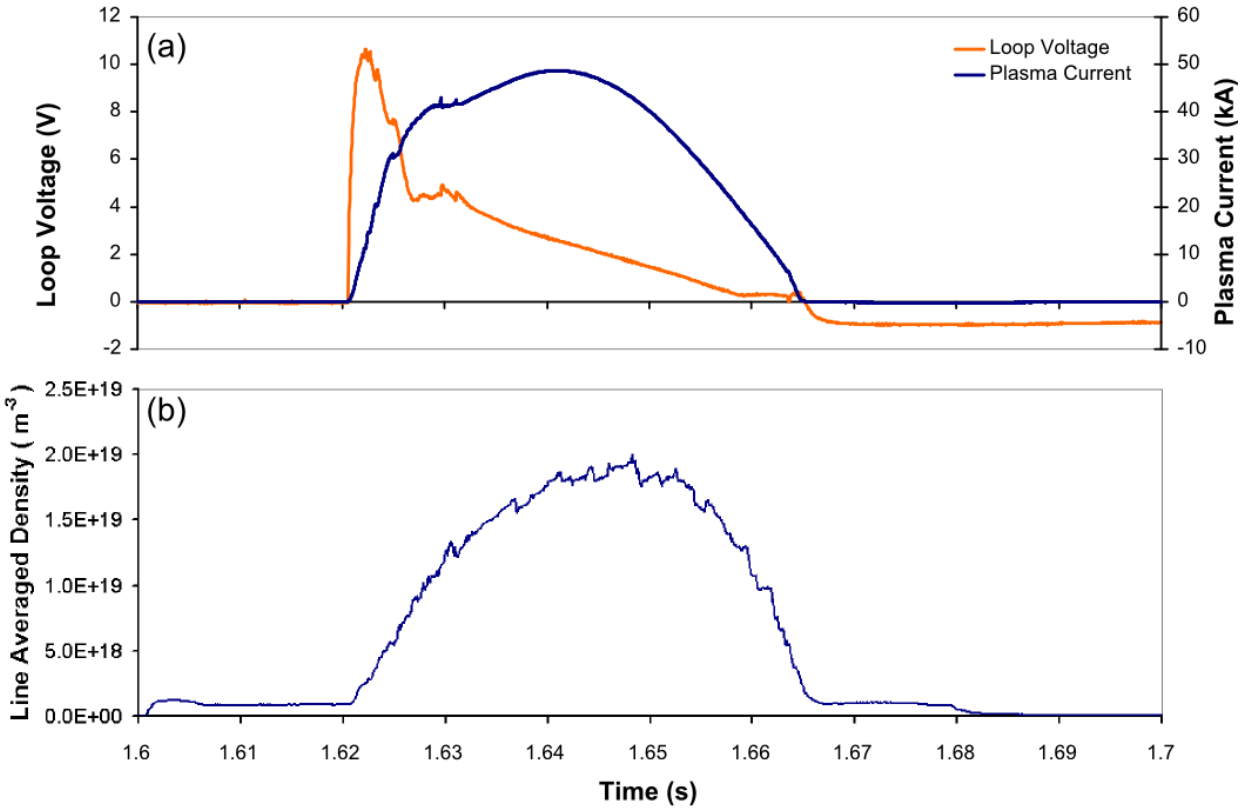

Figure 6.24 – (a) Measured loop voltage and toroidal plasma current as well as (b) line-averaged electron density for shot 11051954

As before, a series of equilibrium reconstructions were performed at every 50 μs through the shot. Once again, the two-power current density parameterization was assumed with the parameter β=5. The assumed pressure profile shown in Figure 6.10 was again held constant for each of the reconstructions. The time evolution of the two reconstructed parameters, $\Psi_{t_{tot}}$ and α, are shown in Figure 6.25 (c) and (d). As seen during the high vacuum transform shot (11050236), there are a series of temporal hesitations present during the rising plasma current. There is a rise in the loop voltage during each of these hesitations indicating increased plasma resistivity. Figure 6.25 (b) displays the edge rotational transform which results from the equilibrium reconstructions. The first brief hesitation in the current ramp begins at 1.6234 s and corresponds to when the edge rotational transform is ¼. There does not appear to be a change in

the evolution of the reconstructed current density parameter α during this time, but the parameter is already slowly decreasing through this time. The second hesitation begins at 1.6248 s and corresponds to the time when the edge rotational transform is ⅓. The parameter α decreases at a greater rate during this time, but then increases slightly once the ⅓ surface has moved beyond the last closed flux surface. The changes in the reconstructed parameters during these first two hesitations in the current rise are very similar to the trends shown in Figure 6.13. However, the next hesitation in the plasma current does not occur when the edge rotation transform is equal to ½, but rather ι_e= 0.42. As before, during this period of relatively constant plasma current, the reconstructed parameter α begins a steep descent. Although the ½ resonant surface is not directly on the last closed flux surface during this time, the reconstructed iota profile (Figure 6.26) shows this surface is near the edge of the plasma during this time. A similar result on the Alcator A tokamak found that MHD instabilities during the current ramp phase of the discharge led to a sudden redistribution of the plasma current.[49] In this case, these instabilities were linked to the presence of rational surfaces within the interior of the plasma and were not localized to the edge. The reconstructed current density profile is shown in Figure 6.26, and shows that there is a steep current density gradient in the shaded region where ι = ½. Experiments on W VII-A have shown that MHD modes become unstable when the rational magnetic surfaces exist in regions with a steep current density gradient.[46] A magnetic island may exist on the ι = ½ surface, and based on the small shear present in the reconstructed iota profile it may be large enough to interact with the edge of the plasma. The trends in the current density profile are again consistent with the idea that there is an enhancement in the edge transport as discussed in Sec 6.1.

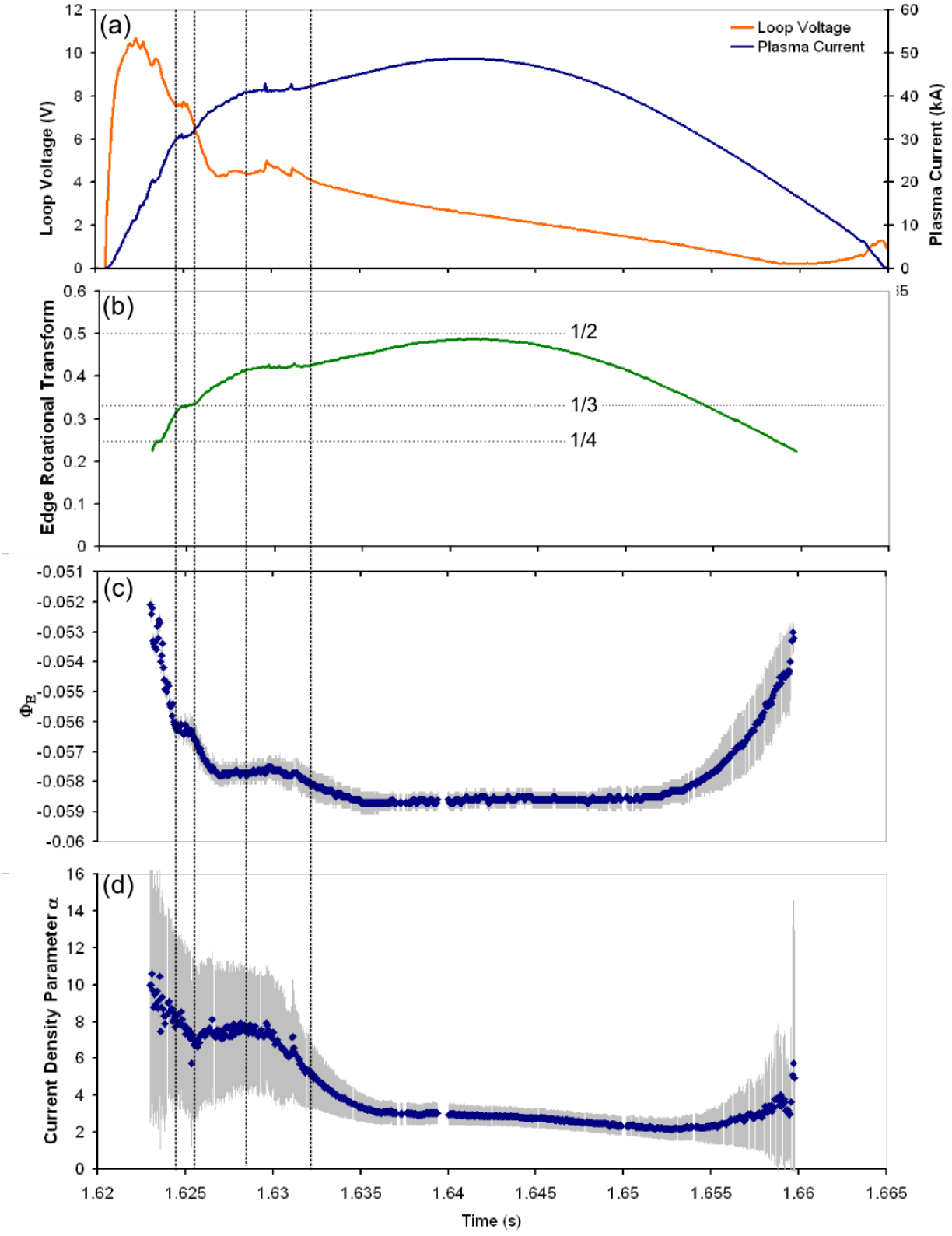

Figure 6.25 – Reconstruction results versus time for shot 11051954, including (a) plasma current and loop voltage, (b) edge rotational transform, (c) total toroidal flux, and (d) current density profile parameter α.

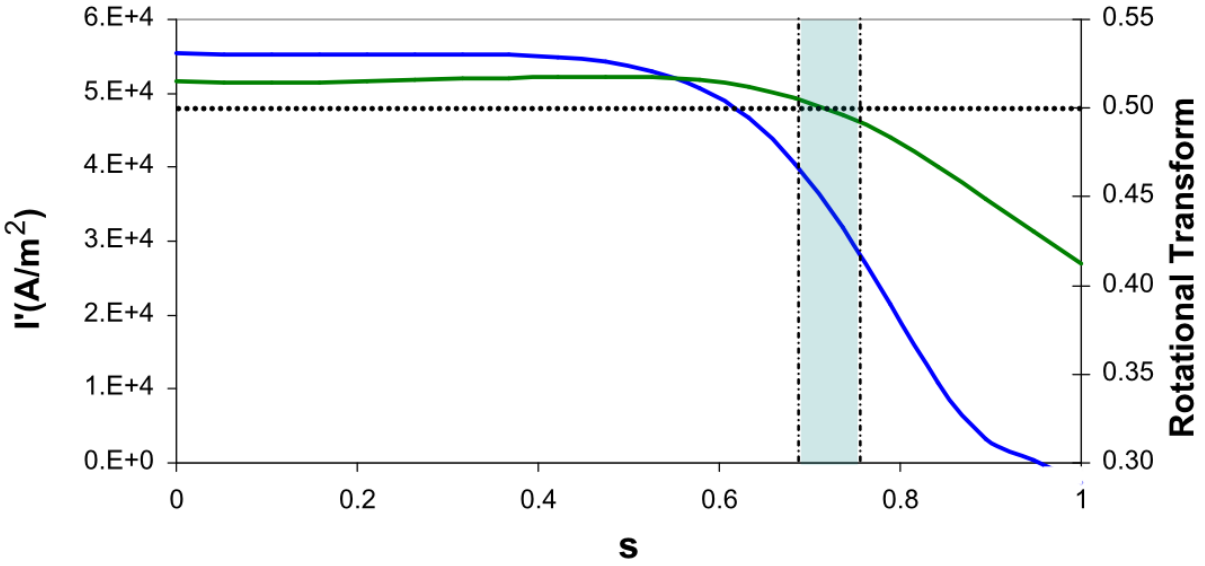

Figure 6.26 – Reconstructed current density profile (blue) with the associated rotational transform profile (green) for shot 11051954 at 1.63s

Closer examination of the time period when the edge rotational transform is close to ½ reveals a series of sudden changes in the plasma current. These changes can be seen in Figure 6.27 (a) along with the corresponding changes in the measured loop voltage. Signals from an array of Mirnov coils that measure fluctuations in the poloidal magnetic field are shown in Figure 6.27(b). The 16 Mirnov coils span the full poloidal circumference of the plasma. The data from separate channels have been offset in the figure to show the oscillations. The measured magnetic field perturbations are defined as:

$$\tilde{B}_\theta = B_\theta(r)e^{i(m\theta - n\phi)} \tag{6.10}$$

The oscillations starting at 1.63 s show a poloidal periodicity of m=2. This indicates the presence of a rotating ½ magnetic island. The amplitude of the oscillation also grows indicating the island is becoming larger. The presence of a magnetic island could result in an increased transport of higher temperature plasma from the interior to the edge. This may result in the formation of a

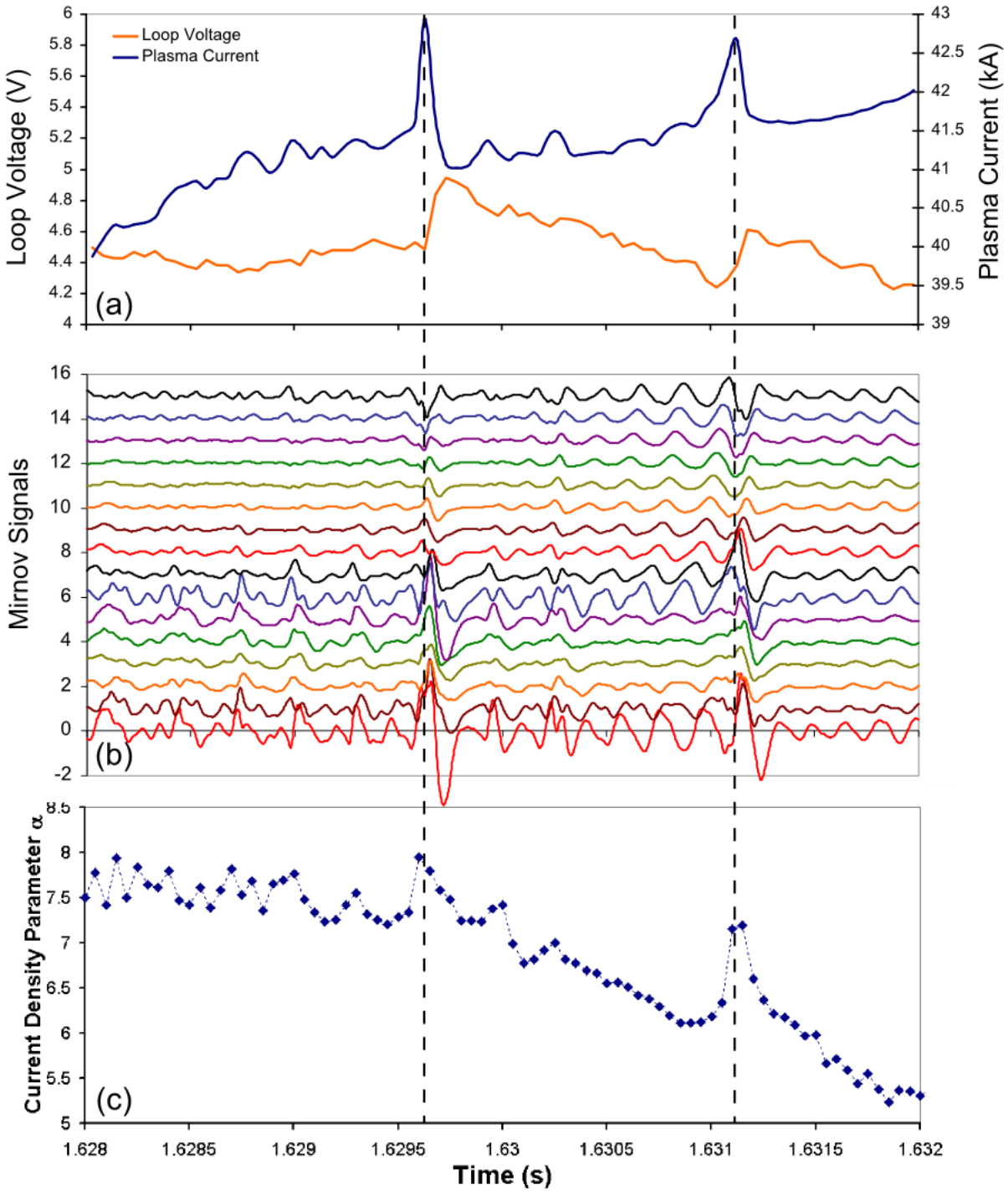

Figure 6.27 – Effects of MHD activity due to the ι=½ rational surface seen in the (a) measured plasma current and loop voltage, (b) poloidal Mirnov coil array, as well as (c) the reconstructed current density parameter α.

skin current which would explain the sharp increases in the plasma current. The current density parameter α is shown in Figure 6.27 (c), and suggests the current density profile is becoming broader. This trend is also consistent with the formation of a skin current. As the skin current increases, the local rotational transform would change. The result is an unstable iota profile which can lead to rapid diffusion of the current as described for Alcator A discharges[49].

6.4 Reconstructed Equilibria compared with Hall Probe results

The previous three sections have shown that the parameters reconstructed using Rogowski coil signals and the V3FIT code not only vary smoothly in time during each shot, but also show similar trends from shot to shot. To provide a check of the reconstructed current density profile, a comparison should be made with direct measurements of the current density profile. The Hall sensor array described in Sec. 3.3 can be inserted into the plasma. This array provides point measurements of the poloidal magnetic field within the last closed flux surface, to provide a direct measurement of the current density profile over part of the plasma radius.

During the shot presented in Sec. 6.1 (11050236), the inward-most Hall sensor was positioned at a major radius of 0.9484 m. The positions of each element of the Hall sensor array along with the reconstructed flux surfaces are shown in Figure 6.5 (c) at a time of t = 1.64 s. The radial position of the plasma moves outward as the plasma current increases. Due to this motion of the plasma, the number of Hall sensors within the plasma varies with time. Based on the position of the reconstructed flux surfaces, the plasma first envelops the tip of the probe in shot 11050236 at t = 1.632 s. The measured plasma density exhibits a sudden increase a short time later at t=1.645 s as shown in Figure 6.2 (a). Most shots with the Hall probe present in the plasma show a degradation of the plasma current, both in magnitude and duration. These results

have been recorded in previous experiments when boron nitride probes are inserted into current carrying plasma discharges, and are likely the result of an increase in plasma impurity due to ablation from the BN probe sheath[36]. Although the presence of the probe affects the plasma, these diagnostic measurements can still be compared to the reconstruction results obtained using external magnetic diagnostics alone.

The poloidal magnetic field strengths are calculated from the reconstructed equilibrium for each Hall sensor position that was within the last closed flux surface. These calculated field strengths are compared to those measured by the Hall sensor array in Figure 6.28. The radial trend of B_θ with r is similar for both curves, but there is a consistent 0.0065 T offset between the measured and modeled poloidal field strengths. Although the fields calculated from the model are purely poloidal, a few of the Hall sensor measurements include a small component from the toroidal field due to minor misalignments, as discussed in Sec. 5.7. By using the fitting procedure described in Sec. 5.7, the magnetic field contributed from the external coils at each Hall sensor location was subtracted to compare the poloidal field produced by the plasma current. This comparison is shown in Figure 6.29. The offset of ~ 0.0065 T seen in Figure 6.28, is now slightly diminished to ~ 0.0055 T in Figure 6.29. This offset is much larger than the similar comparison shown in Figure 5.14 which is from a shot in which there was no plasma current. This confirms that the offset is not due to a sensor calibration error, or an error in the calculation of the external poloidal field contribution. The slope of the measured and modeled poloidal field strengths are in good agreement, but the amplitude difference suggests the error is in the modeled equilibrium.

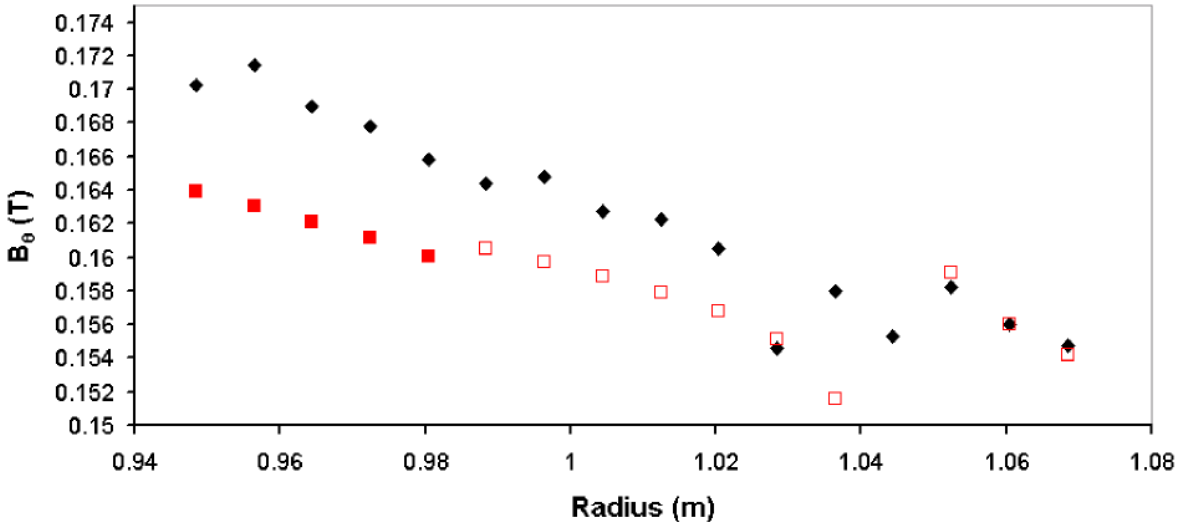

Figure 6.28 – Total poloidal magnetic field versus major radius as measured by Hall sensors (black) and those calculated from the reconstructed equilibria (red) for shot 11050236 at 1.64s. Open boxes are outside calculated last closed flux surface.

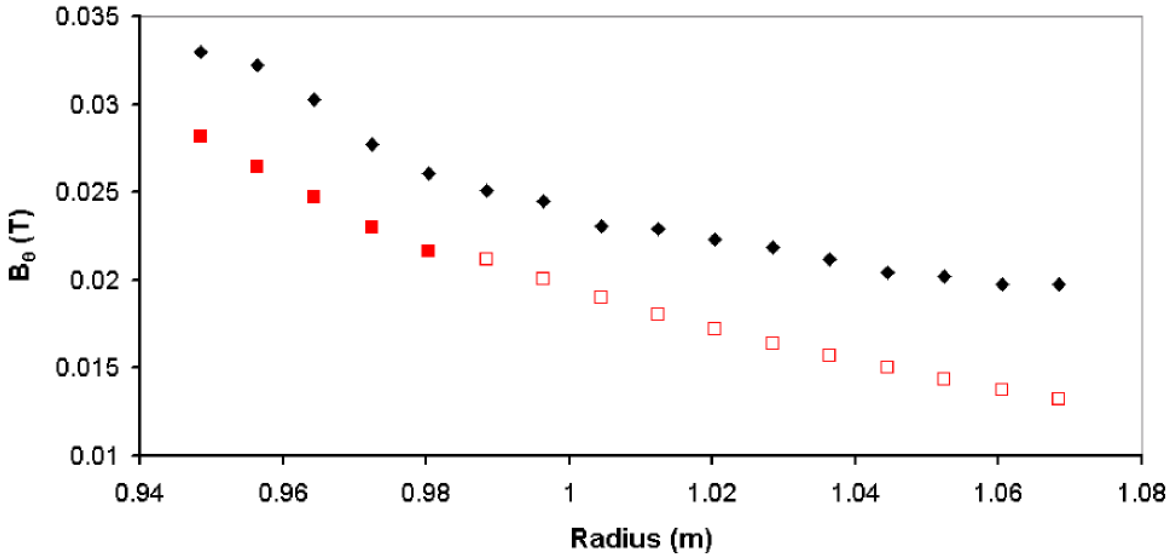

Figure 6.29 – Poloidal magnetic field contributed by plasma current versus major radius as measured by Hall sensors (black) and as calculated from the reconstructed equilibria (red) for shot 11050236 at 1.64s. Open boxes are outside calculated last closed flux surface.

To further investigate the offset a similar comparison is made for the low transform shot presented in Sec. 6.3 (11051954). During this shot, the inner-most Hall sensor was positioned with a minor radius of 0.9584 m. There was no noticeable increase in the plasma density or

decrease in the plasma current due to the presence of the probe. However, only two of the 16 Hall sensors were within the last closed flux surface of the reconstructed plasma. A comparison of the poloidal magnetic field contributed from the plasma current as measured by the Hall sensors to that calculated from the reconstructed equilibria are shown in Figure 6.30. Once again, there is an offset of approximately 0.0055 T between the modeled and measured poloidal magnetic field strength. The gradient of the measured and modeled poloidal field strengths are also nonetheless similar.

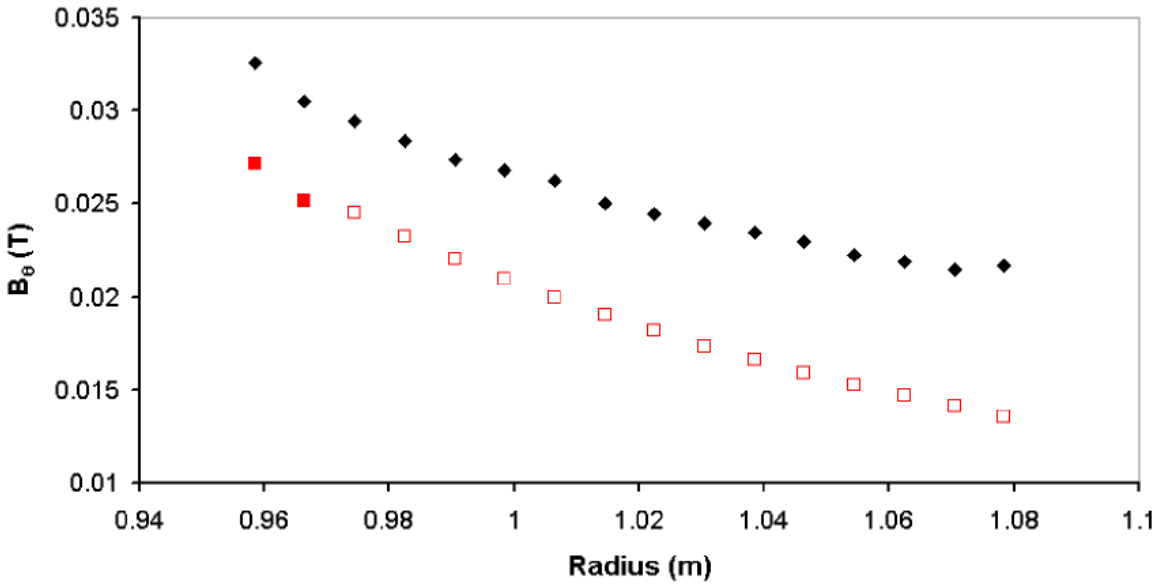

Figure 6.30 – Poloidal magnetic field contributed by plasma current versus major radius as measured by Hall sensors (black) and as calculated from the reconstructed equilibria (red) for shot 11051954 at 1.64s. Open boxes are outside calculated last closed flux surface.

Similar to the systematic error described for the Rogowski coils, the offsets in the Hall probe results appear to be due to the distribution of the reconstructed current density. In Sec. 6.1, a significant reduction in χ^2 is achieved when the full Rogowski diagnostic signal is removed as a reconstruction constraint and the plasma current is added as a

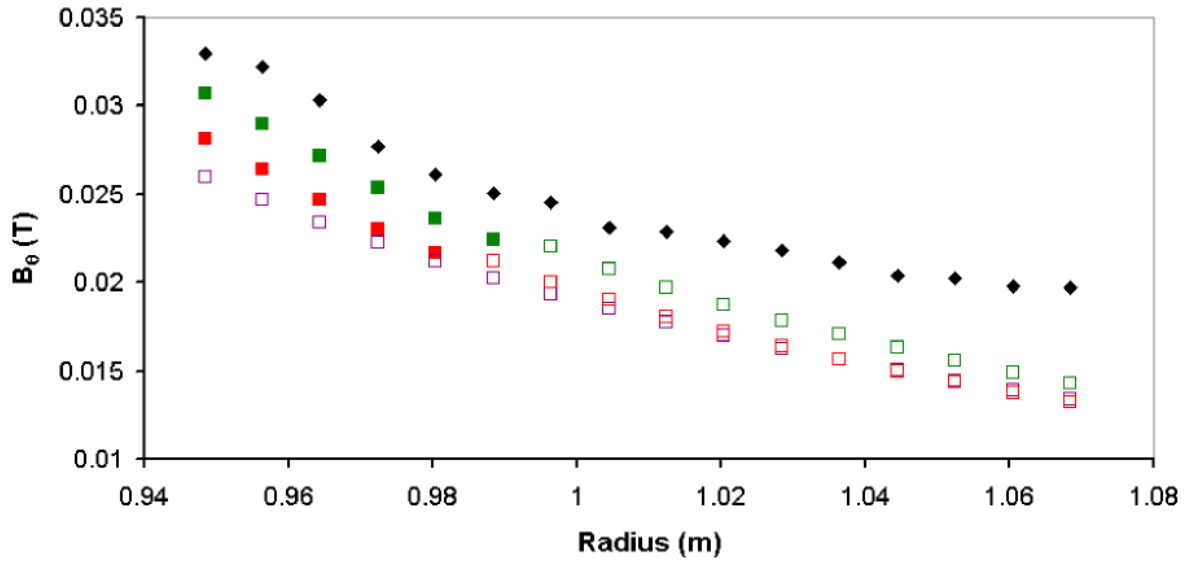

Figure 6.31 – Poloidal magnetic field contributed by plasma current vs. radius measured by Hall sensors (black) and from reconstructed equilibria (boxes) for shot 11050236 at 1.64s with the initial equilibrium (red), 6% higher current (green), and elongated in addition to higher current (purple). Open boxes are outside last closed flux surface.

reconstruction parameter. The resulting 6% increase in the plasma current not only reduced χ^2 but as shown in green in Figure 6.31, also results in a smaller offset between the reconstructed poloidal magnetic field and the Hall probe measurements. This improved agreement with the Hall probe measurements provides additional support for the calibration of the full Rogowski coil being incorrect. The modified equilibrium in Sec. 6.1 that results in the best fit to the diagnostic data includes not only an increase in plasma current, but is also elongated using the SVF coil. The values of the poloidal field calculated from this modified equilibrium are shown as purple boxes in Figure 6.31. Even though the χ^2 value shown in Table 6.10 is much lower, the offset from the Hall probe measurements is greater.

Despite the remaining systematic error, the Hall sensor measurements can also be used to verify the time evolution of the current density profiles. Unfortunately, for shots 11050236 and 11051954, the Hall sensor array was outside the last closed flux surface during the times when

the reconstructed equilibria showed the greatest change in the current density profile. To validate the trends seen in the current density profile, further experiments were performed in which the Hall probe was extended much further into the vacuum vessel. The presence of the probe for these runs in fact led to large changes in the density and a reduction of the total plasma current. However, neither of these changes prevented reconstructions of the plasma equilibria. More importantly, the initial portion of the shot demonstrated similar characteristics of those previously presented in Figure 6.13 and Figure 6.25.

During shot 11080512, the inner most Hall sensor had a major radius of 0.9084 m. The external coil currents for this shot were configured the same as in shot 11050236 (Figure 6.1). Similar to the reconstruction results shown in section 6.1, there are a series of hesitations in the plasma current ramp which correspond to times when there is a rational surface near the edge of

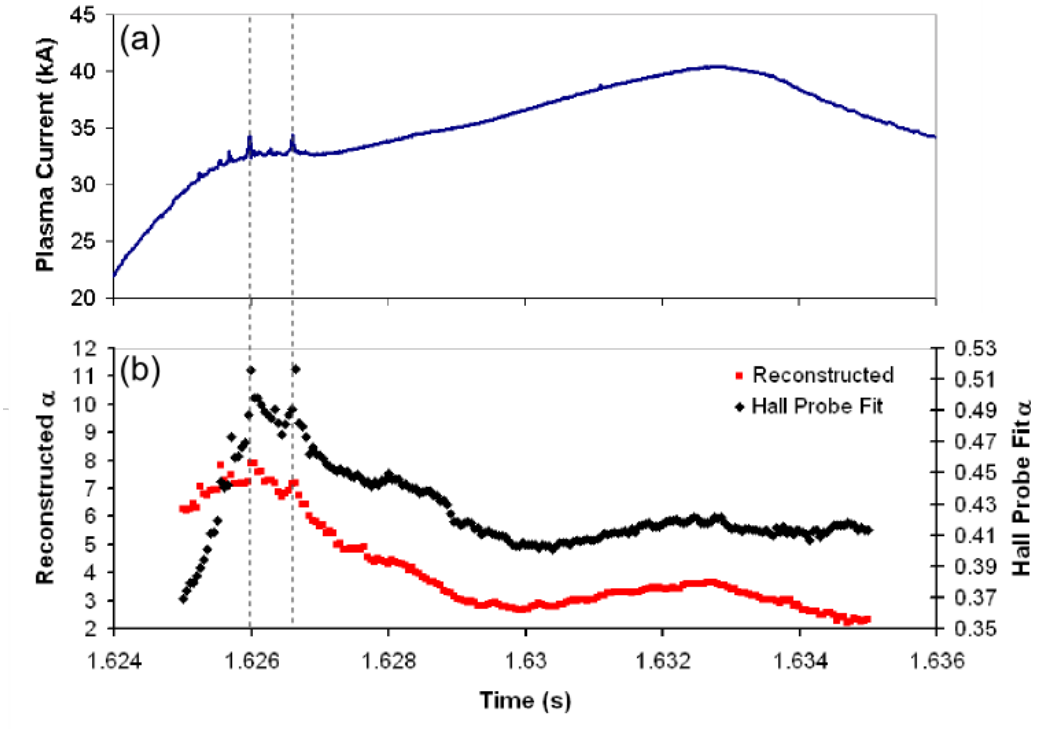

Figure 6.32 – (a) Measured plasma current (b) Current density parameter α as determined from equilibrium reconstruction (red) and that determined from fitting the Hall probe magnetic field measurements.

the plasma. The measured plasma current for a portion of the overall shot is shown in Figure 6.32 (a). The time evolution of the reconstructed α parameter is shown in Figure 6.32 (b). Similar to the previously discussed shots, the current density profile becomes more peaked during and following the hesitation in the plasma current ramp corresponding to $\iota_e = ½$.

In order to compare the trend in the reconstructed parameter α with the Hall probe results, the poloidal magnetic field measured by the Hall probe was expressed in terms of the parameter α, using Ampere's law (see Appendix A.2). To approximate a current density distribution from the Hall probe measurements, the plasma was assumed to be cylindrically symmetric. With the poloidal magnetic field expressed in terms of r and α, a Levenberg - Marquardt solver was used to determine the parameter α which best fit the poloidal field measured by the Hall sensors. The resulting α values are plotted in Figure 6.32. While the values of α are smaller than those determined through reconstruction, the trend is very similar. The dashed lines indicate times when apparent MHD activity results in sharp changes in the measured plasma current. Corresponding changes in the current density profile are shown in the reconstructed results as well as those determined from the Hall probe measurements.

6.5 Recommended Next Steps

The results presented in this dissertation demonstrate that the process of equilibrium reconstruction can effectively model plasma phenomenon on the CTH torsatron. Two reconstructed parameters have been used to track the evolution of the plasma equilibrium during the time of the discharge. However, allowing only one free parameter to define the current density profile is a rather stringent limitation. This single parameter generally indicates how peaked the current profile is, without allowing for a more complex distribution. For example, the

current density parameterizations being used do not allow for the possibility of a hollow profile. As reported on tokamaks[48,49], skin currents can develop during the current ramp phase of the discharge which can result in a hollow current density profile. Current density parameterizations which can model these more complex profiles require a larger number of free parameters. With the diagnostics currently being used, reconstructing more than two parameters leads to a higher level of uncertainty in the reconstructed parameters. Although there are 25 diagnostic signals, the 24 segmented Rogowski coils provide similar measurements in that each measure the poloidal magnetic flux at the edge of the plasma. Jones and Finn have shown that an increased number of diagnostics of the same type do little to decrease the posterior variance of reconstructed equilibrium parameters[39]. Adding different types of diagnostic signals to the set currently being used should allow a greater number of parameters to be reconstructed while maintaining lower posterior variance values.

As mentioned in Sec. 2.2, CTH is equipped with several types of plasma diagnostics. One diagnostic which has recently been incorporated into V3FIT is the soft X-ray diagnostic. This diagnostic consists of 100 chordal measurements of the plasma emissivity. Initial reconstructions using this diagnostic have reconstructed electron density profiles[50]. The reconstructions presented in this dissertation use an assumed pressure profile which remains constant through the shot. Data from the soft X-ray diagnostic in combination with a measurement of the average plasma temperature using the new X-ray spectrometer should provide a better estimation of the evolution of the plasma pressure. Also, using both the soft X-ray diagnostics along with the Rogowski coils as input signals to V3FIT should make it possible to reconstruct a greater number of parameters and improve the overall fit. The soft X-ray diagnostic can also be used to investigate the apparent elongation of the flux surfaces described in Sec. 6.1. A similar use of

soft X-ray tomography has been used on the JET tokamak to validate the equilibria reconstructed using magnetic diagnostics[51].

Besides the soft X-ray diagnostic, there are a series of additional magnetic diagnostics that will soon be used in the reconstruction process. The analysis of the remaining systematic error discussed in Sec. 6.1 indicates that the measurement of the plasma current made by the Rogowski coil 1PI264 may have a small error in the calibration. The calibration of this coil should be rechecked, and perhaps another full internal Rogowski coil should be added. In addition to the Rogowski coils, a set of saddle coils have been installed on CTH. These coils measure the radial magnetic flux rather than the poloidal flux which is measured by the Rogowski coils and when combined with the Rogowski coils, should further improve the reconstruction.

Another set of magnetic diagnostic signals which should be included in the reconstruction process are the Hall sensor measurements. As shown in Figure 6.32 (b), data from the Hall sensors have already been used to show a similar trend in the evolution of the current density profile to that determined through equilibrium reconstruction. As discussed in Sec. 4.2, magnetic diagnostic signals calculated using V3FIT which extend beyond the last closed flux surface are currently unreliable. Further code development will be required for V3FIT to properly simulate this type of diagnostic. Once this functionality has been added, the internal poloidal field measurements should greatly enhance the determination of the current density profile.

Finally, the reconstructions performed in this dissertation each assume stellarator symmetric equilibria. A close examination of Figure 6.6 reveals that the observed Rogowski signals and typically greater than those modeled for poloidal angles of between 45˚ - 135˚. Figure 6.6 (a) and (b) present data taken at symmetry planes when the plasma is assumed to be

up-down symmetric. The measured poloidal fluxes are consistently higher at the top of each symmetry plane than at the bottom. This implies the plasma equilibrium is vertically shifted upward from the mid-plane. Reconstructions should eventually be performed without the assumption of stellarator symmetry. Further development is required to incorporate the non-stellarator symmetric functionality of VMEC into the V3FIT code.

References

[1] J. D. Hanson, S. P. Hirshman, S. F. Knowlton, L. L. Lao, E. A. Lazarus, and J. M. Shields, Nuclear Fusion **49**, 075031 (2009).

[2] J. P. Freidberg, *Plasma Physics and Fusion Energy* (Cambridge University Press, 2007), p. 671.

[3] M. Balat, Energy Sources, Part B: Economics, Planning, and Policy **2**, 31-47 (2007).

[4] B. M. Fronk, R. Neal, and S. Garimella, Journal of Energy Resources Technology **132**, 021009 (2010).

[5] K. Miyamoto, *Plasma Physics for Nuclear Fusion* (MIT Press, 1980), p. 610.

[6] John Wesson and D. J. Campbell, *Tokamaks* (Clarendon Press, 2004), p. 749.

[7] 50 years of Lawson criteria | EFDA JET, Retrieved October 7, 2011, from Www.jet.efda.org /jet/news/2005/12/50-years-of-lawson-criteria/ (2005).

[8] J.D. Lawson, Proceedings of the Physical Society **B70**, (1957).

[9] M. Wakatani, *Stellarator and Heliotron Devices (International Series of Monographs on Physics)* (Oxford University Press, USA, 1998), p. 464.

[10] Fusion Research Today | Fusenet, Retrieved October 7, 2011, From www.fusenet.eu/node/42 (2011).

[11] J. P. Freidberg, Review of Modern Physics **54**, 801 (1982).

[12] L.L Lao, J.R Ferron, R.L Miller, T.H Osborne, V.S Chan, R.J Groebner, G.L Jackson, R.J. La Haye, E.J Strait, T.S Taylor, A.D Turnbull, E.J Doyle, E.a Lazarus, M Murakami, G.R McKee, B.W Rice, C Zhang, and L Chen, Nuclear Fusion **39**, 1785-1792 (1999).

[13] O. Katsuro-Hopkins, S.a. Sabbagh, J.M. Bialek, H.K. Park, J.G. Bak, J. Chung, S.H. Hahn, J.Y. Kim, M. Kwon, S.G. Lee, S.W. Yoon, K.-I. You, a.H. Glasser, and L.L. Lao, Nuclear Fusion **50**, 025019 (2010).

[14] W. Howl, a. D. Turnbull, T. S. Taylor, L. L. Lao, F. J. Helton, J. R. Ferron, and E. J. Strait, Physics of Fluids B: Plasma Physics **4**, 1724 (1992).

[15] E. J. Strait, Physics of Plasmas **1**, 1415 (1994).

[16] S Sakakibara, K Watanabe, S Ohdachi, Y Narushima, K Toi, K Tanaka, K Narihara, K IDA, T Tokuzawa, K Kawahata, H Yamada, and A Komori, Fusion Science and Technology **58**, 176 (2010).

[17] A. Scarabosio, A. Pochelon, and Y. Martin, Plasma Physics and Controlled Fusion **49**, 1041-1060 (2007).

[18] E A Lazarus, Nuclear Fusion Supplement **1**, 609-626 (1994).

[19] S Hirshman, Computer Physics Communications **43**, 143-155 (1986).

[20] J.L. Luxon and B.B. Brown, Nuclear Fusion **22**, 813-821 (1982).

[21] L L Lao, Nuclear Fusion **25**, 1611-1622 (1985).

[22] L.L. Lao, H.E. St. John, Q. Peng, J.R. Ferron, E.J. Strait, T.S. Taylor, W.H. Meyer, C. Zhang, and K.I. You, Fusion Science and Technology **48**, 968-977 (2005).

[23] D.P O'Brien, L.L Lao, E.R Solano, M Garribba, T.S Taylor, J.G Cordey, and J.J Ellis, Nuclear Fusion **32**, 1351-1360 (1992).

[24] H.J. Gardner, Nuclear Fusion **30**, 1417-1424 (1990).

[25] R.N. Morris, J.C. Glowienka, G.H. Neilson, S.P. Hirshman, and P. Merkel, Nuclear Fusion **29**, 2115-2123 (1989).

[26] S. Tsaun and Hogun Jhang, Fusion Engineering and Design **82**, 163-174 (2007).

[27] R. Yoshino, Proceedings of the 36th IEEE Conference on Decision and Control 3709-3714 (1997).

[28] I. H. Hutchinson, *Principles of Plasma Diagnostics* (Cambridge University Press, 2002), p. 440.

[29] S. Cauffman and R. Majeski, Review of Scientific Instruments **66**, 817 (1995).

[30] B. J. Braams, Plasma Physics and Controlled Fusion **33**, 715-748 (1991).

[31] E. J. Strait, Fusion Science and Technology **53**, 304-334 (2008).

[32] M W Bongard, R J Fonck, B T Lewicki, and a J Redd, The Review of Scientific Instruments **81**, 10E105 (2010).

[33] Y. Liu, D. Maurer, G. Navratil, and N. Rivera, Review of Scientific Instruments **76**, 093501 (2005).

[34] I. Ďuran, J. Stöckel, G. Mank, K. H. Finken, G. Fuchs, and G. Van Oost, Review of Scientific Instruments **73**, 3482 (2002).

[35] GH-701.PDF, Retrieved October 7, 2011, From fwbell.com/ckfinder/userfiles/files/GH-701.PDF (2008).

[36] P. D. Coleman, B. D. Blackwell, M. Kristiansen, and M. O. Hagler, IEEE Transactions on Plasma Science **9**, 123-125 (1981).

[37] W. H. Press, S. A. Teukolsky, W. T. Vetterling, and B. P. Flannery, *Numerical Recipes 3rd Edition: The Art of Scientific Computing* (Cambridge University Press, 2007), p. 1256.

[38] D. Sivia and J. Skilling, *Data Analysis: A Bayesian Tutorial* (Oxford University Press, USA, 2006), p. 264.

[39] C. S. Jones and J. M. Finn, Nuclear Fusion **46**, 335-349 (2006).

[40] S. P. Hirshman, E. A. Lazarus, J. D. Hanson, S. F. Knowlton, and L. L. Lao, Physics of Plasmas **11**, 595 (2004).

[41] J. Peterson, J. Hanson, G. Hartwell, and S. Knowlton, Physics of Plasmas **17**, 032505 (2010).

[42] J. Bialek, A. H. Boozer, M. E. Mauel, and G. A. Navratil, Physics of Plasmas **8**, 2170 (2001).

[43] M. D. Kruskal, J. L. Johnson, M. B. Gottlieb, and L. M. Goldman, Physics of Fluids **1**, 421 (1958).

[44] V. D. Shafranov, Soviet Physics JETP **6**, 545 (1958).

[45] J. D. Callen and G. L. Jahns, Physical Review Letters **38**, 491-495 (1977).

[46] W VII-A Team, Nuclear Fusion **20**, 1093-1100 (1980).

[47] J. P. Freidberg, *Ideal Magnetohydrodynamics* (Plenum Press, 1987), p. 489.

[48] S. V. Mirnov and I. B. Semenov, Sov. J. Plasma Phys.(Engl. Transl.);(United **4**, 27 (1978).

[49] R.S. Granetz, I.H. Hutchinson, and D.O. Overskei, Nuclear Fusion **19**, 1587 (1979).

[50] G.J. Hartwell, J. Hanson, S.F. Knowlton, and B.A. Stevenson, in *Bulletin of the American Physical Society 52nd Annual Meeting of the APS Division of Plasma Physics* (Chicago, IL, 2010).

[51] J.P. Christiansen, J.D. Callen, J.J. Ellis, and R.S. Granetz, Nuclear Fusion **29**, 703-711 (1989).

[52] R Valencia, G Olayo, and G Cruz, Journal of Nuclear Materials **228**, 254-256 (1996).

[53] G. Verdoolaege, R. Fischer, and G. Van Oost, Plasma Science, IEEE Transactions On **38**, 3168–3196 (2010).

[54] A. Razmara, P. Khorshid, and M. Ghoranneviss, Research Journal of Applied Sciences **6**, 209-212 (2011).

Appendix

A.1 Estimation of Plasma Temperature from Spitzer resistivity

An estimation of the plasma temperature can be made from the measurements of the loop voltage and the plasma current. For this estimation, the plasma is assumed to be toroidally symmetric with a major radius of R_0. Beginning with Ohm's law and that the toroidal electric field (E) is constant:

$$J = \frac{E}{\eta_s} \qquad E = \frac{V_{loop}}{2\,\pi\,R_0} \tag{A.1}$$

where the current density J is defined in terms of the Spitzer resistivity. Wesson defines the Spitzer resistivity as[6]:

$$\eta_s = \frac{Z_{eff}\left(1.65\times10^{-9}\right)\ln\Lambda}{T_e^{3/2}}\ \Omega\cdot m \tag{A.2}$$

where T_e is the electron temperature, $\ln\Lambda$ is the Coulomb logarithm, and Z_{eff} is the effective charge state. A value for the Coulomb logarithm of $\ln\Lambda \approx 15$ is commonly assumed for hot plasmas[28]. The effective charge state depends on the amount of impurities in the plasma and has not been measured for CTH plasmas. A reasonable estimate based on previously published[52-54] values is $2 \le Z_{eff} \le 3$. Substituting in the Spitzer resistivity into Eq. x.x and solving for the electron temperature gives:

$$T_e = \left[\frac{J\ 2\pi\ R_0\ Z_{eff}\left(1.65\times10^{-9}\right)\ln\Lambda}{V_{loop}}\right]^{2/3}\ \text{keV} \tag{A.3}$$

If we consider the measurements shown in Figure x.x at t = 1.64 s, then the peak current density is $J_0 = 9.36\times10^5\ A\,m^{-2}$ calculated using VMEC. Also, the measured loop voltage at this time is

$V_{loop} = 2.66\,\mathrm{V}$. Assuming the plasma is centered in the vacuum vessel, $R_0 = 0.75\,\mathrm{m}$ and $Z_{eff} = 2.5$, the electron temperature is estimated as:

$$T_e = \left[\frac{\left(9.36\times10^{5}\ \mathrm{A\,m^{-2}}\right) 2\pi \left(0.75\,\mathrm{m}\right) 2.5 \left(1.65\times10^{-9}\right) 15}{\left(2.66\,\mathrm{V}\right)} \right]^{2/3} \mathrm{keV} \qquad \text{(A.4)}$$

$$T_e = 0.219\,\mathrm{keV}$$

A.2 Poloidal Magnetic Field in terms of the fit parameter α

When cylindrical geometry is assumed, the definition of $I'(s)$ as defined by Eq. 4.x can be expressed in the following way:

$$I'(s) = I'\left(\frac{r^2}{a^2}\right) = \int_0^{2\pi} J_{z'}\, r\, d\theta \tag{A.5}$$

Here s in cylindrical geometry is expressed in terms of the radial position r and an assumed plasma radius a. Also, the poloidal-like flux coordinate u now directly corresponds to the poloidal coordinate θ, and $J_{z'}$ is the toroidal component of the current density. With the assumed symmetry, r and $J_{z'}$ are constant, and Eq. x.x becomes:

$$J_{z'} = \frac{I'\left(\frac{r^2}{a^2}\right)}{2\pi r} = \frac{I_0'}{2\pi r}\left[1-\left(\frac{r^2}{a^2}\right)^{\alpha}\right]^5 \tag{A.6}$$

where the expression on the far right results from substituting the two-power fit (eqn. 6.4) in for I' and setting β=5. Now, this expression can be substituted into Ampere's law which gives the poloidal magnetic field in terms of r and α.

$$\left[\nabla \times \mathbf{B}\right]_z = \mu_0 \mathbf{J}_z$$

$$\frac{1}{r}\left[\frac{\partial}{\partial r}\left(rB_\theta\right) - \frac{\partial B_r}{\partial \theta}\right] = \frac{\mu_0 I_0'}{2\pi r}\left[1-\left(\frac{r^2}{a^2}\right)^{\alpha}\right]^5 \tag{A.7}$$

Assuming $B_r = 0$,

$$\int \partial\left(rB_\theta(r)\right) = \frac{\mu_0 I_0'}{2\pi}\int\left[1-\left(\frac{r^2}{a^2}\right)^\alpha\right]^5 dr$$

$$B_\theta(r) = \frac{\mu_0 I_0'}{2\pi}\left[1-\left(\frac{r^2}{a^2}\right)^\alpha\left[\frac{5}{1+2\alpha}-\frac{10\left(\frac{r^2}{a^2}\right)^\alpha}{1+4\alpha}+\frac{10\left(\frac{r^2}{a^2}\right)^{2\alpha}}{1+6\alpha}-\frac{5\left(\frac{r^2}{a^2}\right)^{3\alpha}}{1+8\alpha}+\frac{\left(\frac{r^2}{a^2}\right)^{4\alpha}}{1+10\alpha}\right]\right] \quad \text{(A.8)}$$

Now with this definition, a Levenberg – Marquardt solver was used to determine the α which best fits the series of $B_\theta(r)$ measurements made by the Hall probe.